

OXIDE MATERIALS FOR SPINTRONIC DEVICE  
APPLICATIONS

by

Megan Campbell Prestgard

A dissertation submitted to the faculty of  
The University of Utah  
in partial fulfillment of the requirements for the degree of

Doctor of Philosophy

Department of Materials Science and Engineering

The University of Utah

December 2015

Copyright © Megan Campbell Prestgard 2015

All Rights Reserved

# The University of Utah Graduate School

## STATEMENT OF DISSERTATION APPROVAL

The dissertation of Megan Campbell Prestgard  
has been approved by the following supervisory committee members:

<u>Ashutosh Tiwari</u>	, Chair	<u>10/19/2015</u> Date Approved
<u>Gerald Stringfellow</u>	, Member	<u>10/21/2015</u> Date Approved
<u>Anil Virkar</u>	, Member	<u>10/21/2015</u> Date Approved
<u>Richard Cohen</u>	, Member	<u>10/26/2015</u> Date Approved
<u>Shelley Minter</u>	, Member	<u>10/19/2015</u> Date Approved

and by Feng Liu, Chair of  
the Department of Materials Science and Engineering

and by David B. Kieda, Dean of The Graduate School.

## ABSTRACT

Spintronic devices are currently being researched as next-generation alternatives to traditional electronics. Electronics, which utilize the charge-carrying capabilities of electrons to store information, are fundamentally limited not only by size constraints, but also by limits on current flow and degradation, due to electro-migration. Spintronics devices are able to overcome these limitations, as their information storage is in the spin of electrons, rather than their charge. By using spin rather than charge, these current-limiting shortcomings can be easily overcome. However, for spintronic devices to be fully implemented into the current technology industry, their capabilities must be improved. Spintronic device operation relies on the movement and manipulation of spin-polarized electrons, in which there are three main processes that must be optimized in order to maximize device efficiencies. These spin-related processes are: the injection of spin-polarized electrons, the transport and manipulation of these carriers, and the detection of spin-polarized currents.

In order to enhance the rate of spin-polarized injection, research has been focused on the use of alternative methods to enhance injection beyond that of a simple ferromagnetic metal/semiconductor injector interface. These alternatives include the use of oxide-based tunnel barriers and the modification of semiconductors and insulators for their use as ferromagnetic injector materials. The transport of spin-polarized carriers is heavily reliant on the optimization of materials' properties in order to enhance the carrier

mobility and to quench spin-orbit coupling (SOC). However, a certain degree of SOC is necessary in order to allow for the electric-field, gate-controlled manipulation of spin currents. Spin detection can be performed via both optical and electrical techniques. Using electrical methods relies on the conversion between spin and charge currents via SOC and is often the preferred method for device-based applications.

This dissertation presents experimental results on the use of oxides for fulfilling the three spintronic device requirements. In the case of spin injection, the study of dilute magnetic dielectrics (DMDs) shows the importance of doping on the magnetic properties of the resulting tunnel barriers. The study of spin transport in ZnO has shown that, even at room temperature, the spin diffusion length is relatively long, on the order of 100 nm. These studies have also probed the spin relaxation mechanics in ZnO and have shown that Dyakonov-Perel spin relaxation, operating according to Fermi-Dirac statistics, is the dominant spin relaxation mechanism in zinc oxide. Finally, spin detection in ZnO has shown that, similar to other semiconductors, by modifying the resistivity of the ZnO thin films, the spin Hall angle (SHA) can be enhanced to nearly that of metals. This is possible by enhancing extrinsic SOC due to skew-scattering from impurities as well as phonons. In addition, thermal spin injection has also been detected using ZnO, which results support the independently measured inverse spin-Hall effect studies. The work represented herein illustrates that oxide materials have the potential to enhance spintronic device potential in all processes pertinent to spintronic applications.

## TABLE OF CONTENTS

ABSTRACT.....	iii
LIST OF FIGURES .....	vii
LIST OF TABLES .....	x
LIST OF ABBREVIATIONS.....	xi
ACKNOWLEDGEMENTS .....	xiii
Chapters	
1. INTRODUCTION .....	1
1.1 The Datta-Das Spin-Field Effect Transistor .....	2
1.2 Spin Injection .....	4
1.3 Spin Transport and Manipulation .....	13
1.4 Spin Detection.....	17
1.5 References .....	22
2. EXPERIMENTAL METHODS.....	41
2.1 Pulsed Laser Deposition and Sol-Gel Method.....	42
2.2 Thin Film Characterization Techniques.....	45
2.3 The Spin Seebeck Effect .....	48
2.4 The Hanle Effect .....	49
2.5 The Inverse Spin Hall Effect.....	53
2.6 References .....	55
3. DILUTE MAGNETIC DIELECTRIC MATERIALS FOR SPIN INJECTION .....	65
3.1 Introduction.....	66
3.2 Experimental Procedures .....	67
3.3 Results and Discussion .....	69
3.4 Conclusions.....	71
3.5 References .....	73

4. SPIN TRANSPORT IN ZINC OXIDE THIN FILMS AS OBSERVED USING NONLOCAL HANLE MEASUREMENTS .....	79
4.1 Introduction.....	80
4.2 Experimental Procedures .....	81
4.3 Results and Discussion .....	82
4.4 Conclusions.....	91
4.5 References.....	92
5. OBSERVATION OF THE INVERSE SPIN HALL EFFECT IN ZINC OXIDE THIN FILMS.....	99
5.1 Introduction.....	100
5.2 Experimental Procedures .....	102
5.3 Results and Discussion .....	103
5.4 Conclusions.....	106
5.5 References.....	108
6. SPIN-ORBIT COUPLING IN ZINC OXIDE: INTRINSIC OR EXTRINSIC? .....	115
6.1 Introduction.....	116
6.2 Experimental Procedures .....	118
6.3 Results and Discussion .....	120
6.4 Conclusions.....	130
6.5 References.....	132
7. FUTURE WORK AND CONCLUSION .....	148
7.1 Future Work.....	148
7.2 Conclusion .....	151
7.3 References.....	153
8. LIST OF PUBLICATIONS .....	156
Appendices	
A: EXPERIMENTAL DESIGN AND TESTING OF THE 4T HANLE DEVICE .....	158
B: DEVICE DESIGN FOR ALL-ELECTRICAL INVERSE SPIN HALL EFFECT EXPERIMENTS .....	165
C: DEVICES FOR ELECTRICAL AND THERMAL SPIN INJECTION IN ZNO .....	169

## LIST OF FIGURES

### Figures

1.1	The Datta-Das spin-field effect transistor.....	29
1.2	Spin valve device schematic and operation principles .....	30
1.3	Spin-dependent processes in a spin-FET .....	31
1.4	Methods of electrical spin injection.....	32
1.5	Common spin injector materials: A density of states comparison.....	33
1.6	Tunnel barriers for spin injection.....	34
1.7	Thermal spin injection: The magnon-mediated spin Seebeck effect .....	35
1.8	Optical spin pumping .....	36
1.9	Microwave spin pumping .....	37
1.10	Spin relaxation mechanisms .....	38
1.11	Mechanism of spin-orbit interaction.....	39
1.12	Optical detection of spin-polarization .....	39
1.13	Mechanisms of the extrinsic spin Hall effect.....	40
2.1	Pulsed laser deposition schematic.....	57
2.2	Sol-gel process for nanopowder fabrication .....	57
2.3	X-ray diffraction, X-ray photoelectron spectroscopy, and X-ray absorption spectroscopy .....	58
2.4	X-ray absorption spectrum.....	59



2.5	The Hall effect .....	60
2.6	The spin Seebeck effect .....	61
2.7	The 3-terminal Hanle effect .....	61
2.8	The 4-terminal Hanle effect .....	62
2.9	The Hanle curve: Two cases .....	63
2.10	The inverse spin Hall effect .....	64
3.1	X-ray diffraction pattern for Co: CeO <sub>2</sub> thin films and the STO substrate .....	75
3.2	CeO <sub>2</sub> :Co X-ray absorption spectra.....	76
3.3	X-ray photoelectron spectroscopy data for the CeO <sub>2</sub> :Co thin films .....	77
3.4	M versus H data for the phase-separated CeO <sub>2</sub> :Co thin films .....	78
4.1	Device structure used for nonlocal Hanle measurements .....	94
4.2	ZnO thin film characterizations .....	95
4.3	ZnO Hanle curves and corresponding fittings .....	96
4.4	Calculated spin lifetime and spin diffusion length in ZnO .....	97
4.5	Spin relaxation rate fit to linear and cubic Dyakonov-Perel terms .....	98
5.1	X-ray diffraction pattern of the ZnO thin films .....	110
5.2	Optical and electrical ZnO thin film characterizations .....	111
5.3	ZnO inverse spin Hall effect device structure.....	112
5.4	ISHE Device signal: Deconvolution of magnetoresistance, bias, and ISHE contributions .....	113
5.5	Inverse spin Hall effect signal.....	114
6.1	Device arrangements to test for the ISHE, the SSE, the Nernst effect, and the anomalous Nernst effect in ZnO .....	138
6.2	Voltage signal generated due to electrical and thermal spin injection in ZnO .....	139

6.3	The composition and temperature dependence of the spin Hall angle in ZnO .....	140
6.4	3D Contour plot showing spin Hall angle versus temperature and composition....	141
6.5	The relative spin Seebeck voltage, electrical resistivity, and magnon-injected spin current .....	142
6.6	Nernst effect and anomalous Nernst effect signals .....	143
6.7	The relative spin Hall angle measured via electrical and thermal spin injection....	144
6.8	Spin Hall conductivity versus temperature for all compositions .....	145
6.9	Spin Hall resistivity versus electrical resistivity squared for all compositions .....	146
6.10	Spin Hall resistivity versus electrical resistivity: A fit of the 0.1 mTorr data .....	147
7.1	3T Hanle device with a CeO <sub>2</sub> :Co DMD tunnel barrier and Al injector .....	154
7.2	R-axis ZnO ISHE results .....	155
A.1	Procedure for fabricating the 4T Hanle devices .....	163
A.2	Hanle device testing arrangement .....	164
B.1	Procedure for fabricating the ISHE testing devices .....	167
B.2	ISHE device schematic .....	168
C.1	Raw V <sub>SSE</sub> versus T data .....	174

## LIST OF TABLES

### Tables

6.1	Temperature dependence of the inverse spin Hall effect in ZnO thin films deposited under 0.1 mTorr .....	135
6.2	Temperature dependence of the inverse spin Hall effect in ZnO thin films deposited under 1 mTorr .....	136
6.3	Temperature dependence of the inverse spin Hall effect in ZnO thin films deposited under 10 mTorr .....	137
6.4	Composition dependence of the intrinsic and extrinsic contributions to the spin-orbit coupling in ZnO.....	138

## LIST OF ABBREVIATIONS

FET	Field effect transistor
Spin-FET	Spin-field effect transistor
FM	Ferromagnet
DMS	Dilute magnetic semiconductor
DMD	Dilute magnetic dielectric
SSE	Spin Seebeck effect
SHE	Spin Hall effect
YIG	Yttrium iron garnet, $\text{Y}_3\text{Fe}_5\text{O}_{12}$
SOI	Spin-orbit interaction
SOC	Spin-orbit coupling
BAP	Bir-Aronov-Pikus spin relaxation
EY	Elliott-Yafet spin relaxation
DP	Dyakonov-Perel spin relaxation
DM	Dzyaloshinskii-Moriya spin relaxation
SIA	Structural inversion asymmetry
BIA	Bulk inversion asymmetry
ISHE	Inverse spin Hall effect
PLD	Pulsed laser deposition
XRD	X-ray diffraction

XPS	X-ray photoelectron spectroscopy
XAS	X-ray absorption spectroscopy
XANES	X-ray absorption near-edge fine structure
EXAFS	Extended X-ray absorption fine structure
AFM	Atomic force microscopy
UV/Vis	Ultraviolet/Visible spectroscopy
MR	Magnetoresistance
ZFC	Zero-field cooled
FC	Field cooled
LCF	Linear combination fit

## ACKNOWLEDGEMENTS

I would like to thank Dr. Ashutosh Tiwari for giving me the opportunity to be a part of the Nanostructured Materials Research Laboratory and for his continual guidance and support. I would also like to thank my graduate committee members for their support, advice, and useful discussions throughout my time here at the University of Utah. I would like to thank the National Science Foundation for funding through Grant #DMR-0746486 (CAREER) and Grant #1121252 (MRSRC) and the University of Utah Graduate School for providing partial funding as a 2014-2015 Graduate Research Fellow. I am also grateful to the Utah ARCS Foundation for awarding me the 2012 Dr. Stacy K. Firth Scholar Award. Finally, a very big thanks to my husband Brad for his never-ending love and patience.

## CHAPTER 1

### INTRODUCTION

In 1990, Datta and Das proposed the first active spintronic device.<sup>1</sup> It was this device, a spin-based field effect transistor (spin-FET), that launched the field of active spintronics worldwide.<sup>2-4</sup> Prior to this revolution in the field, spintronic research was focused on passive devices – devices where there is no external control and manipulation of the spin-polarized electrons.<sup>5</sup> In order to make spintronic technologies useful for more wide-scale applications, the field of active spintronics was proposed. Active spintronics involve the study, use, and manipulation of an electron's spin in order to mimic the operation of traditional electronics, which use an electron's charge as opposed to its spin.<sup>6</sup> The applications of these active devices include their potential for next-generation computing, in order to continue the development of the technology sector beyond the failure of Moore's Law.<sup>6</sup> To make this possible, an understanding of spin-based processes and behaviors in semiconductors is necessary. Herein, these processes and behaviors will first be discussed in the framework of a spin-FET and then research into novel, oxide-based materials for fulfilling such applications will be introduced. This work will culminate with a discussion on the future of active spintronics, comment on future research directions, and a discussion of the potential for the implementation of such devices in the technology sector.

### 1.1 The Datta-Das Spin-Field Effect Transistor

The development of active spintronic devices all started with the Datta-Das spin-FET transistor, shown in Figure 1.1.<sup>1,2</sup> In this device, electrons are first spin-polarized in a metal contact and are then injected into the transistor channel. The spin-polarized electrons (spins) then transport from the injector towards the detector. While the spins are moving through the channel, they can be manipulated by applying a gate voltage, to generate an electric field, across the channel. Based on the channel material used, this electric field can have a large impact on the spin transport, as it controls the strength of the Rashba spin-orbit coupling (SOC) in the channel. This SOC results in a loss of spin coherence and thus, the modulation of this Rashba term controls the “on”/“off” ratio of the spin current in a spin-FET.<sup>7</sup> Spin current simply refers to any current comprised of a majority number of either spin-up or spin-down polarized electrons.<sup>8</sup> Once the spin current reaches the spin detector, it must be measured. However, if the current is a pure spin current, electrical detection is not possible via traditional means. A pure spin current is pure spin motion – that is, spin-up and spin-down electrons move in opposite directions, giving a net charge current of zero. In this case, the pure spin current needs to be measured in one of the following ways: (1) detected optically as polarized light, or (2) transformed to electrical current to allow for the use of traditional measurements. Both have been used extensively in research and will be explained in detail at a later point.

As was mentioned, the Datta-Das spin-FET was the first active spintronic device to be proposed. However, it was not the first spintronic device – this came years earlier with the invention of passive spintronic devices. Passive spintronic devices rely only on the spin of electrons and not their motion. These are currently used in magnetic read



heads and magnetic-RAM applications.<sup>9</sup> An example of a passive spintronic device, a spin-valve, is shown in Figure 1.2. These devices operate on the principle of spin-dependent scattering. When a current that contains spin-up and spin-down polarized electrons is passed through a spin valve, the scattering of the two types of spin (the spin-up and spin-down polarizations) will depend on their orientation relative to the polarization of the magnetic layers in the spin valve. Specifically, spin-polarized carriers that are oriented in the same direction as the polarization of the magnetic layers will be able to pass through the device with relatively low scattering – that is, a relatively low resistance.<sup>10</sup> Conversely, if the spin orientation is opposite to the magnetic layers' spin-polarization, the scattering rate will be high and the resistance will be high. These devices can be used as magnetic read-heads, which requires one of the magnetic layers to be a soft magnet. In this case, the magnet will be able to “read” the magnetization of a hard magnetic layer – i.e., of the magnetic storage medium. The magnetization of the soft layer can be determined by “reading” if the spin valve is in the high- or low-resistance state.<sup>10</sup>

Passive spintronics are particularly useful for certain types of storage media. However, they cannot be used as transistors, which is why active spintronic devices are necessary. Active devices use both the spin of electrons as well as their motion to make more complex devices, such as the spin-FET. However, because of the complexity of these devices, there has not yet been a fully functional spin-FET that is ready for implementation in current electronics.<sup>11</sup> This is because the capabilities of spin injection, spin transport and the manipulation of spin, and spin detection are inadequate. These three main processes are the current limiting factors in the fabrication of active spintronic

devices; without optimizing each of these processes independently, active spintronic devices will not be possible. Because of this, research over the last 25 years has focused primarily on improving capabilities and understanding in these three areas: the injection of spin in semiconductors, the transport of spin and how these carriers can be manipulated using a gate-type structure, and how the “on” and “off” spin current states will be detected (Figure 1.3).<sup>12</sup> In the following sections, each of these three areas will be introduced, with a focus on discussing how each of these processes are performed, highlighting present and past research over the last 25 years, and laying a framework for future studies.

## 1.2 Spin Injection

The first process in the operation of a spintronic device is the insertion of spin-polarized electrons into the semiconductor channel, which can be done four ways: electrically, thermally, optically, or via microwave spin pumping. Electrical injection has been the more traditionally used method and typically involves two steps: first, the polarization of electrons in a contact and second, the injection of those polarized carriers into the semiconductor channel.<sup>13</sup> Thermal spin injection is a relatively new technique, in which a temperature gradient is used to excite and inject spin current.<sup>14</sup> Optical spin injection relies on the selection rules for optical transitions to convert circularly polarized light to spin current.<sup>15</sup> Microwave spin pumping is the injection of spin current via spin resonance in an adjoining layer.<sup>16</sup> These four spin injection techniques will be detailed in the following sections.

### 1.2.1 Electrical Spin Injection<sup>1</sup>

Traditionally, there are four main methods of electrical spin injection. In the simplest case, a ferromagnetic metal is used to inject spins directly into the semiconductor channel (Figure 1.4a).<sup>1,17</sup> The second method of injection uses a tunneling barrier to reduce impedance mismatches between the ferromagnet and the semiconductor, giving a final, ferromagnetic metal-tunnel barrier-semiconductor structure (Figure 1.4b).<sup>18</sup> The third method addresses materialistic mismatches again by having the ferromagnetic injector itself be semiconducting through use of a dilute-magnetic semiconductor (DMS) (Figure 1.4c).<sup>19-23</sup> The fourth method suggests use of a ferromagnetic tunnel barrier, a dilute magnetic dielectric (DMD), with a nonmagnetic metal injector to promote enhanced polarization and efficiency (Figure 1.4d).<sup>24-27</sup> In the following subsections, each of these methods of electrical spin injection will be described in detail.

#### 1.2.1.1 Ferromagnetic Metal/Semiconductor Injection Interface

The first spin injectors were relatively simple, consisting of only a ferromagnetic (FM) metal contact in which spins were polarized and the semiconducting channel material into which the spins were injected (Figure 1.4a).<sup>1,17</sup> Despite their straightforward design, the efficiency of these spin injectors is often low, usually less than 5% even at temperatures below 10 K.<sup>28</sup> The limiting factors in efficiency include low levels of spin-

---

<sup>1</sup> Section 1.2 and related subsections on electrical spin injection are based on the following paper: Advanced Materials Letters. (2014) **5**, 242-247. Oxides for Spintronics: A Review of Engineered Materials for Spin Injection, M. C. Prestgard, G. Siegel, and A. Tiwari, VBRI Press. Reprinted with permission.

polarization and a conductivity mismatch between the metal and semiconductor layers.<sup>28</sup> The failure of these devices can be accurately described by theoretical predictions made by Schmidt et al.<sup>29</sup> In these estimations, Schmidt was able to describe the spin-polarization within the semiconductor ( $\alpha_2$ ) as a function of the spin-polarization in the ferromagnetic metal ( $\beta$ ), the conductivity of the metal and semiconducting materials ( $\sigma_{FM}$  and  $\sigma_{SC}$  respectively), and the spin diffusion length within those layers ( $\lambda_{FM}$  and  $\lambda_{SC}$ ). In this equation, eq. 1.1, it is shown that, even for relatively large spin-polarization in the ferromagnet (60% for example), spin-polarization in the semiconductor is greatly limited and degrades quickly as a function of the penetration depth (the depth of spin injection over which spin coherence is maintained),  $\chi_0$ ,

$$\alpha_2 = \beta \cdot \frac{\lambda_{FM}}{\sigma_{FM}} \cdot \frac{\sigma_{SC}}{\lambda_{SC}} \cdot \frac{2}{\left(2 \frac{\lambda_{FM}}{\chi_0} \cdot \frac{\sigma_{SC}}{\sigma_{FM}} + 1\right) - \beta} \quad (1.1)$$

In fact, for spin-polarizations less than 90%, spin injection depth is limited to less than 100 nm.<sup>29</sup> Because this degree of spin-polarization is typically impossible in traditional ferromagnetic metals, half-metals were proposed as a potential solution. Half-metals contain only one type of spin at the Fermi energy (Figure 1.5), therefore 100% spin-polarization, and injection, should be feasible.<sup>30, 31</sup> However, typical half-metals, such as Heusler alloys, are less than desirable due to their tendency to become oxidized, which causes them to lose their half-metallic nature. As such, a half-metal oxide is highly desired, one of which is  $\text{La}_{0.7}\text{Sr}_{0.3}\text{MnO}_3$  (LSMO). Unfortunately, the use of an

LMSO/semiconductor spin injector still did not prove exceptionally efficient, as the conductivity mismatch between the ferromagnet and semiconductor still significantly hindered spin injection. In order to overcome the mismatch between injector and channel conductivities, the use of an intermediate tunnel barrier was proposed.<sup>18</sup>

#### 1.2.1.2 Ferromagnetic Metal/Tunnel Barrier Junctions for Injection

The main goal of using tunnel barriers is to reduce the impedance mismatch between the FM injector and the semiconductor channel by tunneling spin-polarized electrons. Tunnel barriers function as a conduit between the layers and are often a material such as MgO or another insulating oxide (e.g.,  $\text{Al}_2\text{O}_3$ ) (Figure 1.4b). Although using these barriers has allowed for a higher spin-polarization after injection to be achieved, the maximum polarization is still completely limited by the polarization of the FM metal. Another downside to using tunnel barriers is the limitation in the injected spin current. Because spin-polarized electrons are required to tunnel in order to be injected, the number of spins that reach the semiconductor is greatly reduced, which in turn reduces the overall current. In order to avoid this limitation in injected current, it was suggested that a doped semiconductor could be used to remove the impedance mismatch between the injector and channel layers. Because the use of dopants in the semiconductor channel has a large impact on scattering and spin relaxation rates, dopants are generally used to fabricate ferromagnetic semiconductors to be used as spin injectors rather than to modify the properties of the spin transport channel.

### 1.2.1.3 Dilute Magnetic Semiconductor/Semiconductor Injection Interface

In order to satisfy the need for a ferromagnetic semiconductor for spin injection where none exist naturally at room temperature, extrinsic magnetic doping of semiconductors using transition metals has been used for decades. These materials are referred to as dilute magnetic semiconductors (DMS). They can be formed by uniformly doping a semiconductor with a small concentration of transition metal throughout the lattice in order to attain an intrinsically ferromagnetic semiconductor, ideally with room-temperature functionality – intrinsically in this case referring to the magnetic behavior occurring due to uniformly doping throughout the lattice rather than the presence of magnetic clusters; that is, the magnetic behavior is intrinsic to the modified material structure. Novel materials such as GaAs doped with Mn<sup>23</sup>, ZnO doped with Ni<sup>32</sup> and Mn<sup>33</sup>, GaN doped with Mn<sup>34</sup>, and Mn doped InP<sup>35</sup> have been fabricated. However, in order for these materials to be of use in spintronic devices, room-temperature ferromagnetism is a necessity. Theoretical predictions made by Dietl et al. have indicated that both GaN as well as ZnO have the potential to be ferromagnetic at room temperature when doped with manganese concentrations of as little as 5%.<sup>36</sup>

As shown in Figure 1.4c, these materials are advantageous in that they allow a simplified device consisting of only the spin injector and the active semiconducting layer. Because the injector and active layer are both semiconductors, the impedance mismatch between the two is greatly diminished. This allows a possibility for a nearly-unhindered spin-polarized current to be injected into the semiconducting channel. However, the low coercivity of DMS means that an external magnetic field is required in order to attain spin-polarization.<sup>37, 38</sup> Because of this, tunnel barriers are still the most promising method

for spin injection in spintronic devices. However, to enhance spin-polarization in these devices, an alternative, dilute magnetic dielectric, tunnel barrier has been proposed to replace the traditional, oxide tunnel barriers commonly used.

#### 1.2.1.4 Nonmagnetic Metal/Dilute Magnetic Dielectric Tunnel

##### Junctions for Injection

The fourth approach proposed for injecting spin into an active spintronic device eliminates the need for a metallic FM contact. By using a FM tunnel barrier, the spin-polarization will occur on tunneling from the metal to the semiconductor, rather than in the metal itself.<sup>39</sup> For these tunnel barriers, illustrated in Figure 1.4d, a dielectric material doped with ~1-6% transition metal is used. This unique class of material, known as dilute magnetic dielectrics (DMDs), is used to create a barrier which is both electrically insulating as well as intrinsically ferromagnetic.

The goal of a DMD is not to act as a spin injector, but rather to function as a spin filter for polarized injection. This works because the energy requirements for tunneling through DMDs vary directly with spin orientation, as is illustrated schematically in Figure 1.6.<sup>39</sup> As both spin-up and spin-down electrons reach the DMD from the metal, only those with the lower energy requirement for tunneling are capable of passing through into the semiconductor. Because of this, spin-polarization and efficiency may increase drastically compared to other devices, as the total polarization is no longer limited by the polarization of the FM metal.

Much of the current interest surrounding DMDs is regarding the mechanism behind their ferromagnetism. The desired, substitutional doping should result in intrinsic

ferromagnetism. This kind of magnetism is characteristic of a phase-pure material, where the magnetic material has substituted uniformly throughout the lattice. However, extrinsic magnetic behavior can also occur. This magnetism indicates that the ferromagnetic dopant has not substituted into the lattice, but has instead formed magnetic clusters. Both types of doping have been shown, each of which results in its own, unique magnetic response – ferromagnetic for substitutional doping<sup>24</sup> and super-paramagnetic for the clustering of dopants.<sup>40</sup> By being able to distinguish between the two cases, it is possible to ensure intrinsic magnetism as these structures are researched further for their potential as spin filters.

Each of these systems illustrates a different means of spin injection which has been, or is currently being used for the injection of spin-polarized carriers in semiconductor spintronics. Although each has their merits, there are also shortcomings involved with each method which must be addressed before any of these techniques can become the standard injection technique for commercialized spintronic devices.

### 1.2.2 Thermal Spin Injection

In addition to being injected electrically, spin-polarized carriers can also be injected thermally. This is done via the spin-Seebeck effect (SSE), which was first discovered in 2008 by Uchida et al.<sup>14</sup> Typical thermal spin injection is performed using  $\text{Y}_3\text{Fe}_5\text{O}_{12}$  (YIG). Yttrium iron garnet (YIG) is a ferrimagnetic insulator. When a YIG film is placed in a temperature gradient (Figure 1.7), magnon excitation occurs. These magnons, quantized waves of spin precession, propagate through the material along this temperature gradient, in a process generally thought to be mediated by phonon drag



effects.<sup>41,42</sup> For injecting spin, the semiconducting channel is placed on top of the YIG layer. As the magnon propagation occurs, spin current is injected at the YIG/semiconductor interface via spin torque transfer, as the layers are coupled by spin-mixing conductance.<sup>43</sup> Spin torque transfer is the transfer of spin angular momentum from the magnon current to the electrons in the semiconducting layer. This transfer generates a spin current in the semiconductor. This effect can also be observed in a metal; although the mechanism of the SSE is less well understood in metals, it is believed to be a direct spin analogue to the Seebeck effect – a temperature gradient generates a spin voltage which in turn generates spin current in the adjoining material.<sup>44</sup> This spin voltage is understood as the chemical potential difference for spin-up and spin-down electrons. However, because the mechanism of the SSE is better understood in magnetic insulating systems, the YIG-generated SSE is most commonly used.

Since its discovery in 2008, the SSE has been used extensively to inject spin current, especially in metals such as Pt. In addition, the technique can also be used to investigate the spin detection potential of a material; this application will be discussed later in the spin detection section. Although thermal spin injection has already proved to be incredibly useful for spin injection, its recent discovery means that the mechanisms behind this effect have yet to be perfectly understood. As such, in addition to electrical methods for spin injection, two additional techniques are often used: optical and microwave spin pumping.

### 1.2.3 Optical Spin Pumping

In optical spin pumping, circularly polarized light is used to generate spin current.<sup>15</sup> As the circularly polarized light is injected into a semiconductor, the angular momentum of the light is transferred and electrons become spin-polarized due to optical transition selection rules.<sup>45,46</sup> The degree of spin-polarization attained is based on the band-structure of the semiconductor used, according to eq. 1.2:<sup>15</sup>

$$P_s = \frac{P_s^0 + (1 - \nu) \cdot \frac{\tau_R}{2\tau_s}}{1 + (1 + \nu) \cdot \frac{\tau_R}{2\tau_s}}, \quad (1.2)$$

where  $P_s^0$  is the initial spin-polarization upon injection,  $\tau_R$  is the recombination time,  $\tau_s$  is the spin lifetime, and  $\nu$  is the ratio of the upper and lower spin split populations given by the Fermi-Dirac distribution.<sup>15</sup> An example of this is shown in Figure 1.8 for GaAs.

Because of the selection rules for optical transitions, the HH (heavy hole) transitions are 3 times more likely to occur than the LH (light hole) transitions. As such, for spin-polarized light injected with energy lower than the  $\Delta_{SO}$ , the spin-orbit splitting, 50% spin-polarized current will result. If the energy is greater than  $\Delta_{SO}$ , the spin-polarization will be 0%, because the SO transitions are twice as likely as the LH transitions, there will be a net 3 spin-up and 3 spin-down transitions, giving no net polarization. The maximum spin-polarization for GaAs is 50% because, for a bulk sample, the band-structure has 4-fold degeneracy in the valence-band, such that optical transitions from the valence-band to the conduction band occur as outlined in Figure 1.8.

To increase the spin-polarization further, a quantum well-type structure can be used. In this case, the band-structure has 2-fold degeneracy in the valence-band, as strain lifts the LH and HH degeneracy. Because of this, overall spin-polarization can be up to 100% in GaAs quantum well spin injectors.

#### 1.2.4 Microwave Spin Pumping

Microwave spin pumping is similar to thermal spin pumping in magnetic insulators. Microwave radiation is used to induce the precession of spins, which in turn will transfer spin torque into an adjoining, usually semiconducting, layer.<sup>16,47</sup> A schematic of this process is shown in Figure 1.9. This is analogous to the SSE in which magnon precession pumps spin current into a material, except microwave radiation is used in this case to initiate precession.<sup>48</sup>

Although all four of these techniques for spin injection are used extensively, for viability with a spin-FET type device, electrical spin injection remains the focus. Thus, the research included herein will be centered on electrical spin injection, with a brief comparison to the relatively new technique of thermal spin injection.

### 1.3 Spin Transport and Manipulation

Following the injection of spin-polarized carriers into a spintronic device, these carriers must be able to: (1) efficiently transport across the length of the channel and (2) be manipulated, thereby giving spintronic devices the traditional gate-type functionality. To fulfill the first requirement, the spin lifetime in materials must be significantly large to maintain spin coherence while traversing the length of the channel. Spin lifetime is

defined as the time over which spin-polarized carriers can remain polarized, in this case following their injection into the semiconductor channel.<sup>49</sup> For the second requirement of spin manipulation, spin-orbit interaction (SOI; also called spin-orbit coupling, SOC) must be understood, as this describes how a system is influenced by external factors such as magnetic and electric fields.

Increasing the spin lifetime relies on our understanding of spin relaxation mechanisms, and enhancing spin manipulation capabilities relies on our understanding of spin-orbit coupling (SOC).<sup>50-51</sup> In general, there are four spin relaxation mechanisms – mechanisms which describe the relaxation of spin-polarized carriers to an unpolarized state – that affect common semiconductor systems. The first is the Bir-Aronov-Pikus (BAP) mechanism, the second is the Elliott-Yafet (EY) mechanism, the third is the Dyakonov-Perel (DP) mechanism, and the fourth mechanism is the Dzyaloshinskii-Moriya (DM) mechanism.

The BAP mechanism describes the relaxation of spin-polarized electrons via interactions between electrons and holes in the material.<sup>52-54</sup> The electron spins and hole spins interact through exchange interaction and, when hole spins flip due to momentum scattering events (EY mechanism explained below), the interaction between electron spin and hole spin causes the electron spin to likewise flip. A schematic illustration of this mechanism is shown in Figure 1.10a. This mechanism is typically dominant at low temperatures in p-type materials, where electron and hole concentrations are on the same order of magnitude.<sup>54</sup> In n-type materials with low hole concentrations, the BAP relaxation term is generally negligible.

The EY mechanism is used to describe spin relaxation that occurs because of

momentum scattering.<sup>55</sup> This mechanism only occurs in materials with inversion symmetry, as this symmetry causes spin-degeneracy in the system – that is, there is no energy splitting for spin-up and spin-down electrons, as both are possible at any given point. Thus, for every momentum scattering event a spin-polarized electron undergoes, there is a probability of a spin-flip event occurring (Figure 1.10b).<sup>56-57</sup> The probability of a spin-flip event scales with the momentum of electrons in the system, although this probability is generally much weaker than other spin relaxation mechanisms.

The third spin relaxation mechanism is Dyakonov-Perel (DP). The DP mechanism, contrary to the EY mechanism, only occurs in systems with inversion asymmetry.<sup>58,59</sup> This system describes scattering in a material with spin-orbit interaction (SOI). Spin-orbit interaction is the interaction between an electron's spin angular momentum and its orbital angular momentum and is a relativistic effect (Figure 1.11). There is SOI because, from the electron's frame of reference, there is an effective, internal magnetic field due to the orbital motion of the nucleus around the electron, and this effective field will interact with the spin orientation of the electron.<sup>60</sup> In the DP mechanism, similar to EY relaxation, momentum scattering will affect the spin relaxation. However, the DP mechanism is inversely proportional to the momentum scattering. When an electron is scattered by an impurity or defect, its velocity is changed, and this results in a change in the effective internal magnetic field, and thus the spin precession, of the system (Figure 1.10c). In the case where momentum scattering is low, the spins will precess with a finite velocity until they reorient. By having multiple scattering events, the reorientation of the spin-polarized carriers will be minimized, resulting in a much longer spin lifetime.<sup>61</sup>

The final spin relaxation mechanism is the DM mechanism (Dzyaloshinskii-Moriya). DM spin relaxation occurs because of the asymmetric exchange interaction between spin-polarized electrons.<sup>62,63</sup> More specifically, localized spin-up and spin-down electrons behave like electrons, and holes in the BAP spin relaxation mechanism and super-exchange between the two groups causes spin-flip events (Figure 1.10d).<sup>64</sup>

Spin transport is dependent on the spin relaxation mechanisms affecting the system. Although understanding of this is critical to the optimization of spin lifetime, it does not provide information regarding how to manipulate spin-polarized carriers within the semiconductor channel via an electric field. In the above section, SOI was introduced and defined. This interaction can be divided further into Rashba and Dresselhaus spin-orbit interactions. Both of these interactions are due to inversion asymmetry in the crystal structure – Rashba SOI occurs due to structural inversion asymmetry (SIA), whereas Dresselhaus SOI arises due to bulk inversion asymmetry (BIA).<sup>65-67</sup> Rashba SOI can be induced in two ways: (1) internally through growth parameter modulation, or (2) externally through the application of strain or an applied electric field.<sup>68,69</sup> The Dresselhaus SOI is a characteristic of inversion asymmetric crystal lattices, such as the wurtzite crystal structure.<sup>70</sup> Because Rashba SOI can be controlled externally, this is the type of SOI that is desired in spin-FETs or related structures as the strength of the Rashba SOI scales directly with the potential on/off ratio. The focus herein will be on the study of spin relaxation mechanics in oxide semiconductors and on determining the magnitude of the SOC in these systems.

### 1.4 Spin Detection

Spin detection is the final step in the operation of the spin-FET. It is in this step that the spin-polarized carriers are measured. However, the detection of a spin current is a difficult challenge. Traditionally, spin currents can be defined in two ways: as spin-polarized charge current or as a pure spin current. In a spin-polarized charge current, there is a net motion of both electrons as well as spins.<sup>71</sup> In a pure spin current, there is spin motion, but no associated net charge movement, because a pure spin current is defined as the separation of spin-up and spin-down electrons – meaning there is an equal motion of electrons in opposite directions.<sup>71</sup> In the case of pure spin currents, there is no net movement of charge, and thus traditional electronic detection techniques cannot be used. Because of this, spin detection has typically been done using optical techniques. However, in the last decade, the discovery of the intrinsic spin Hall effect<sup>72</sup> and subsequent study of the inverse spin Hall effect (ISHE) has provided a means for converting between spin and charge currents – thereby giving a means for electrical spin detection – in a wide variety of metals and semiconductors.<sup>73-75</sup>

#### 1.4.1 Optical Spin Detection

Traditionally, optical detection methods have been used for measuring spin current. Similar to optical spin injection, in which circularly polarized light is converted into spin via momentum transfer, optical spin detection involves the emission of circularly polarized light in response to a spin current.<sup>76</sup> More specifically, for a perfectly spin-polarized injected current, the spin-polarized electrons will undergo radiative recombination and will return to fill holes in the valence-band.<sup>77</sup> Because of optical

selection rules, this recombination will result in a 50% circularly polarized light (see Figure 1.12).<sup>78</sup> In order to detect the degree of circular polarization, several techniques can be used, such as luminescence to measure the degree of circular polarization or alternative methods, such as Kerr or Faraday rotation.<sup>79-81</sup>

Injection of a spin-polarized current results in right- and left-handed circularly polarized light experiencing different indices of refraction.<sup>79</sup> Both Faraday and Kerr rotation use this to detect spin-polarization. In Kerr rotation, linearly polarized light is reflected off of the material surface. Each of the two circularly polarized components undergo a phase shift, thereby giving a rotation in the circularly polarized light that is reflected that is proportional to the net spin-polarization.<sup>79,82-84</sup> In Faraday rotation, the technique and mechanism are the same as in Kerr rotation, except light is transmitted rather than reflected.<sup>80,85,86</sup> The optical Hanle effect can also be used to measure spin-polarization, by using an external magnetic field to cause spin-randomization and thus change the polarization of the luminescence.<sup>79,87</sup> This measurement of spin-polarization is indirect, as it measures the spin lifetime – therefore indicating the spin-polarization at the time of recombination.<sup>79,88,89</sup> This technique is also commonly used in the discussion of spin transport and manipulation techniques – as such, the electric analogue to this effect will be described in depth in the next chapter. Despite the fact that optical methods constitute a promising means of spin detection, the fabrication of a spin-FET that can function in traditional electronics relies on the development of an all-electrical system, in which spin-polarized carriers are both injected and detected using traditional electrical techniques.



### 1.4.2 Electrical Spin Detection

Although optical spin detection has long been the standard method used, electrical spin detection has recently gained interest. Ever since the discovery of the spin Hall effect, it has been postulated that there could be a device for converting between spin and charge currents in a material, thereby making electrical detection of spin possible.<sup>90</sup> The spin Hall effect describes the conversion of electrical current to spin current due to SOI/SOC. The mechanism of this conversion is twofold: intrinsic due to either Rashba or Dresselhaus spin-orbit coupling in the material itself, or extrinsic due to the presence of high SOC defect states.<sup>91-93</sup>

The intrinsic spin Hall effect was only recently proposed by Murakami et al.<sup>92</sup> and Sinova et al.<sup>72</sup> This effect explains the internal conversion between spin and charge currents due to intrinsic SOC in the material – that is, because spin and orbital angular momenta are coupled, the change in an electron's velocity will result in a change in its effective spin motion.<sup>94</sup> In the case of free electrons, the spin-orbit coupling is due to the spin interacting with the orbital motion of valence electrons in the system. The extrinsic spin Hall effect is also a result of spin-orbit coupling in a material. However, this effect is not caused by the internal SOC of the system, but rather by the SOC of defects or impurities present in the material.<sup>95</sup> Extrinsic SHE, which refers to the interaction between electrons and both phonons and impurities in the system, generally has two mechanisms, attributed to side-jump and skew-scattering events (Figure 1.13).<sup>96-98</sup> In a side-jump event, spin current channels are separated upon scattering about a defect or impurity. In skew-scattering, the scattering process results in the deflection of spin-up and spin-down electrons to opposite ends of the device – that is, generation of a pure spin

current.<sup>98,99</sup> In recent years, the inverse of the SHE has been discovered – that is, the generation of a charge current from a spin current via the same mechanism – and is aptly named the inverse spin Hall effect (ISHE).<sup>100</sup> Because this allows us to convert from spin to charge current, it permits for the electrical measurement of spin current. The efficiency of this conversion is described by the term spin Hall angle ( $\theta_{SH}$ , SHA) and can range from <0.01% to >30%.<sup>101</sup> More about this term will be discussed in later chapters.

As has been outlined herein, there are multiple electrical methods that can be used to efficiently inject, transport, and detect spin currents. However, each of these is not without its shortcomings. In the following sections, the areas of spin injection, spin transport and manipulation, and spin detection will all be investigated in various oxide systems. This dissertation is arranged as follows. In Chapter 2, the growth, characterization, and techniques used for probing the spin-related properties of these materials will be discussed. In Chapter 3, the Co: CeO<sub>2</sub> DMD system will be investigated. In this section, questions regarding the magnetic behavior of this system will be addressed and a framework for determining the nature of magnetic dopants in the dielectric system will be outlined. Chapter 4 will discuss spin transport, lifetime, and spin diffusion length in ZnO thin films. This chapter focuses on the nature of transport in ZnO and comments on the dominant relaxation mechanisms in this system. Spin detection is covered in Chapter 5 and is split into two subsections, the first being on electrical spin detection capabilities in ZnO and the second being on the enhancement of those capabilities through modulation of the temperature and deposition parameters. In this second section, thermal spin injection in ZnO has also been investigated. Chapter 6 will

conclude with a discussion on these works in the framework of a spin-FET and will comment on the future of spintronic research and development.

### 1.5 References

1. Datta, S.; Das, B. *Appl. Phys. Lett.* **1990**, *56*, 665-667.
2. Jansen, R. *Nature Mater.* **2012**, *11*, 400-408.
3. Awschalom, D; Samarth, N. *Physics* **2009**, *2*, 50.
4. Grundler, D. *Phys. World* **2002**, *15*, 39-43.
5. Fert, A. *Thin Solid Films* **2008**, *517*, 2-5.
6. Das Sarma, S.; Fabian, J.; Hu, X.; Zutic, I. *Solid State Commun.* **2001**, *119*, 207-215.
7. Žutić, I.; Fabian, J.; Das Sarma, S. *Rev. Mod. Phys* **2004**, *76*, 323-410.
8. Maekawa, S.; Adachi, H.; Uchida, K.; Ieda, J.; Saitoh, E. *J. Phys. Soc. Jpn.* **2013**, *82*, 102002(1)-(23).
9. Johnson, M. *J. Phys. Chem. B* **2005**, *109*, 14278-14291.
10. Bader, S. D.; Parkin, S. S. P. *Annual Review of Condensed Matter Physics* **2010**, *1*, 71-88.
11. Gardelis, S.; Smith, C. G.; Barnes, C. H. W.; Linfield, E. H.; Ritchie, D. A. *Phys. Rev. B* **1999**, *60*, 7764-7767.
12. Jedema, F. J.; Filip, A. T.; van Wees, B. J. *Nature* **2001**, *410*, 345-348.
13. Prinz, G. A. *Phys. Today* **1995**, *48*, 58-63.
14. Uchida, K.; Takahashi, S.; Harii, K.; Ieda, J.; Koshibae, W.; Ando, K.; Maekawa, S.; Saitoh, E. *Nature* **2008**, *455*, 778-781.
15. Taniyama, T.; Wada, E.; Itoh, M.; Yamaguchi, M. *NPG Asia Materials* **2011**, *3*, 65-73.
16. Heinrich, B.; Burrowes, C.; Montoya, E.; Kardasz, B.; Girt, E.; Song, Y.-Y.; Sun, Y.; Wu, M. *Phys. Rev. Lett.* **2011**, *107*, 066604(1)-(4).
17. Johnson, M. *IEEE Spectrum* **1994**, *31*, 47-51.
18. Rishton, S. A.; Lu, Y.; Altman, R.A.; Marley, A. C.; Bian, X. P.; Jahnes, C.; Viswanathan, R.; Xiao, G.; Gallagher, W. J.; Parkin, S. S. P. *Microelectron. Eng.* **1997**, *35*, 249-252.

19. Ohno, H. *Science* **1998**, *281*, 951-956.
20. Fiederling, R.; Keim, M.; Reuscher, G.; Ossau, W.; Schmidt, G.; Waag, A.; Molenkamp, L. *Nature* **1999**, *402*, 787-790.
21. Ramachandran, S.; Tiwari, A.; Narayan, J. *J. Elect. Mater.* **2004**, *33*, 1298-1302.
22. Snure, M.; Kumar, D.; Tiwari, A. *JOM* **2009**, *61*, 72-75.
23. Ohno, H.; Shen, A.; Matsukura, F.; Oiwa, A.; Endo, A.; Katsumoto, S.; Iye, Y. *Appl. Phys. Lett.* **1996**, *69*, 363-365.
24. Tiwari, A.; Bhosle, V. M.; Ramachandran, S.; Sudhakar, N.; Narayan, J.; Budak, S.; Gupta, A. *Appl. Phys. Lett.* **2006**, *88*, 142511(1)-(3).
25. Griffin, K. A.; Pakhomov, A. B.; Wang, C. M.; Heald, S. M.; Krishnan, K. M. *J. Appl. Phys.* **2005**, *97*, 10D320(1)-(3).
26. Kikoin, K.; Fleurov, V. *Phys. Rev. B.* **2006**, *74*, 174407(1)-(9).
27. Vodungbo, B.; Zheng, Y.; Vidal, F.; Demaille, D.; Etgens, V. H.; Mosca, D. H. *Appl. Phys. Lett.* **2007**, *90*, 062510(1)-(3).
28. Wolf, S. A.; Awschalom, D. D.; Buhrman, R. A.; Daughton, J. M.; von Molnár, S.; Roukes, M. L.; Chtchelkanova, A. Y.; Treger, D. M. *Science* **2001**, *294*, 1488-1495.
29. Schmidt, G.; Ferrand, D.; Molenkamp, L. W.; Filip, A. T.; van Wees, B. J. *Phys. Rev. B.* **2000**, *62*, R4790-R4793.
30. Dong, X. Y.; Adelmann, C.; Xie, J. Q.; Palstrom, C. J.; Lou, X.; Strand, J.; Crowell, P. A.; Barnes, J.-P.; Petford-Long, A. K. *Appl. Phys. Lett.* **2005**, *86*, 102107(1)-(3).
31. Bowen, M.; Bibes, M.; Barthélémy, A.; Contour, J.-P.; Anane, A.; Lemaitre, Y.; Fert, A. *Appl. Phys. Lett.* **2003**, *82*, 233-235.
32. Schwartz, D. A.; Kittilstved, K. R.; Gamelin, D. R. *Appl. Phys. Lett.* **2004**, *85*, 1395-1397.
33. Sharma, P.; Gupta, A.; Rao, K. V.; Owens, F. J.; Sharma, R.; Ahuja, R.; Guillen, J. M. O.; Johansson, B.; Gehring, G. A. *Nature Mater.* **2003**, *2*, 673-677.
34. Baik, K. H.; Frazier, R. M.; Thaler, G. T.; Abernathy, C. R.; Pearton, S. J.; Kelly, J.; Rairigh, R.; Hebard, A. F.; Tang, W.; Stavola, M.; Zavada, J. M. *Appl. Phys. Lett.* **2003**, *83*, 5458-5460.
35. Shon, Y.; Lee, W. C.; Park, Y. S.; Kwon, Y. H.; Lee, S. J.; Chung, K. J.; Kim, H. S.;

- Kim, D. Y.; Fu, D. J. Kang, T. W.; Fan, X. J.; Park, Y. J.; Oh, H. T. *Appl. Phys. Lett.* **2004**, *84*, 2310-2312.
36. Dietl, T.; Ohno, H.; Matsukura, F. *Phys. Rev. B.* **2001**, *63*, 195205(1)-(21).
37. Martinez, B.; Sandiumenge, F.; Balcells, Ll.; Arbiol, J.; Sibieude, F.; Monty, C. *Phys. Rev. B.* **2005**, *72*, 165202(1)-(8).
38. Pérez, L.; Lau, G. S.; Dhar, S.; Brandt, O.; Ploog, K. H. *Phys. Rev. B.* **2006**, *74*, 195207(1)-(5).
39. Roberts, B. K.; Pakhomov, A. B.; Voll, P.; Krishnan, K. M. *Appl. Phys. Lett.* **2008**, *92*, 162511(1)-(3).
40. Prestgard, M. C.; Siegel, G.; Ma, Q.; Tiwari, A. *Appl. Phys. Lett.* **2013**, *103*, 102409(1)-(4).
41. Uchida, K.; et al. *Nature Mater.* **2010**, *9*, 894-897.
42. Uchida, K.; Adachi, H.; Ota, T.; Nakayama, H.; Maekawa, S.; Saitoh, E. *Appl. Phys. Lett.* **2010**, *97*, 172505(1)-(3).
43. Jia, X.; Liu, K.; Xia, K.; Bauer, G. E. W. *Europhysics Lett.* **2011**, *96*, 17005(p1)-(p6).
44. Uchida, K.; Ota, T.; Harii, K.; Ando, K.; Nakayama, H.; Saitoh, E. *J. Appl. Phys.* **2010**, *107*, 09A951(1)-(5).
45. Ando, K.; Saitoh, E. Spin Photodetector: Converseion of Light Polarization Information into Electric Voltage using Inverse Spin Hall Effect. In *Photodetectors* [online]; Gateva, Sanka, Ed.; InTech, 2012; Ch. 18, pp. 405-416. <http://cdn.intechopen.com/pdfs-wm/33526.pdf> (accessed July 7, 2015).
46. Schmidt, G. J. *Phys. D.: Appl. Phys.* **2005**, *38*, R107-122.
47. Tserkovnyak, Y.; Brataas, A.; Bauer, G. E. W.; Halperin, B. I. *Rev. Mod. Phys.* **2005**, *77*, 1375-1421.
48. Hahn. C.; de Loubens, G.; Viret, M.; Klein, O.; Naletov, V. V.; Youssef, J. B.; *Phys. Rev. Lett.* **2013**, *111*, 217204(1)-(5).
49. Cardellino, J.; Scozzaro, N.; Herman, M.; Berger, A. J.; Zhang, C.; Fong, K. C.; Jayaprakash, C.; Pelekhov, D. V.; Hammel, P. C. *Nature Nanotech.* **2014**, *9*, 343-347.
50. Dyakonov, M. I. Basics of Semiconductor and Spin Physics. In *Spin Physics in Semiconductors*; Dyakonov, M. I., Ed.; Springer: Verlag Berlin Heidelberg, 2008; Vol. 157, Ch. 1, pp. 1-28.

51. Crowell, P. A.; Crooker, S. A. Spin Transport in Ferromagnet/III-V Semiconductor Heterostructures. In *Handbook of Spin Transport and Magnetism*; Tsymbal, E. Y.; Zutic, I., Eds.; CRC Press: Boca Raton, 2012; pp. 463-465.
52. Bir, G. L.; Aronov, A. G.; Pikus, G. E.; *Zh. Eksp. Teor. Fiz.* **1975**, *69*, 1382-1397.
53. Bandyopadhyay, S.; Cahay, M. *Introduction to Spintronics*; CRC Press: Florida, 2008; pp. 209-210.
54. Borisenko, V. E.; Ossicini, S. *What is What in the Nanoworld*; Wiley-VCH: Weinheim, 2004; pp. 28.
55. Elliott R. J. *Phys. Rev.* **1954**, *96*, 266-279.
56. Yafet, Y. *Phys. Lett. A* **1983**, *98*, 287-290.
57. Saha, D.; Holub, M.; Bhattacharya, P.; Basu, D. Spin-Based Semiconductor Heterostructure Devices. In *Comprehensive Semiconductor Science and Technology*; Bhattacharya, P. Fornari, R.; Kamimura, H., Eds.; Elsevier: Amsterdam Oxford Burlington, 2011; Vol. 6, Ch. 15, pp. 566-567.
58. Dyakonov, M. I.; Perel, V. I. *Sov. Phys. Solid State* **1971**, *13*, 3023-3026.
59. Boross, P.; Dóra, B.; Kiss, A.; Simon, F. *Scientific Reports* **2013**, *3*, 3233(1)-(5).
60. Pramanik, S.; Kanchibotla, B.; Bandyopadhyay, S. Spins in Organic Semiconductor Nanostructures. In *Handbook of Nanophysics: Principles and Methods*; Sattler, K. D., Ed.; CRC Press: Boca Raton, 2010; Vol. 1, pp. 28-7 – 28-8.
61. Dzyaloshinsky, I. *J. Phys. Chem. Solids* **1958**, *4*, 241-255.
62. Moriya, T.; *Phys. Rev.* **1960**, *120*, 91-98.
63. Fischer, K. H.; Hertz, J. A. *Spin Glasses*; Cambridge University Press: Cambridge, 1991; Ch. 6, pp. 180-182.
64. Kavokin, K. V. *Phys. Rev. B* **2001**, *64*, 075305(1)-(7).
65. Rashba, E.I. *Sov. Phys. Solid State* **1960**, *2*, 1109-1122.
66. Bychkov, Y. A.; Rashba, E. I. *J. Phys. C: Solid State Phys.* **1984**, *17*, 6034-6045.
67. Dresselhaus, G. *Phys. Rev.* **1955**, *100*, 580-586.
68. Nowak, M. P.; Szafran, B.; Peeters, F. M.; Partoens, B.; Pasek, W. J. *Phys. Rev. B* **2011**, *83*, 245324(1)-(12).

69. Bulaev, D. V.; Loss, D. *Phys. Rev. B* **2005**, *71*, 205324(1)-(6).
70. de Sousa, R.; Das Sarma, S. *Phys. Rev. B* **2003**, *68*, 155330(1)-(6).
71. Stevens, M. J.; Smirl, A. L.; Bhat, R. D. R.; Najmaie, A.; Sipe, J. E.; van Driel, H. M. *Phys. Rev. Lett.* **2003**, *90*, 136603(1)-(4)
72. Sinova, J.; Culcer, D.; Niu, Q.; Sinitsyn, N. A.; Jungwirth, T.; MacDonald, A. H. *Phys. Rev. Lett.* **2004**, *92*, 126603(1)-(4).
73. Jungwirth, T.; Wunderlich, J.; Olejnik, K. *Nature Materials* **2012**, *11*, 382-390.
74. Werake, L. K.; Ruzicka, B. A.; Zhao, H. *Phys. Rev. Lett.* **2011**, *106*, 107205(1)-(4).
75. Ando, K.; Saitoh, E. *Nature Commun.* **2011**, *3*, 629(1)-6).
76. Clarke, E.; Harbord, E.; Murray, R. Carrier Spin Dynamics in Self-Assembled Quantum Dots. In *Optical Generation and Control of Quantum Coherence in Semiconductor Nanostructures*; Slavcheva, G.; Roussignol, P., Eds.; Springer: Berlin-Heidelberg, 2010; pp. 43-48.
77. Taniyama, T. Spin Conversion at Magnetic Interfaces. In *Spintronics for Next Generation Innovative Devices*; Sato, K.; Saitoh, E., Eds.; Wiley & Sons LTD: Chichester, 2015; pp. 142-143.
78. Oestreich, M.; Bender, M.; Hübner, J.; Hägele, D.; Rühle, W. W.; Hartman, Th.; Klar, P. J.; Heimbrodt, W.; Lampalzer, M.; Volz, K.; Stolz, W. *Semicond. Sci. Technol.* **2002**, *17*, 285-297.
79. Mikkelsen, M. H.; Myers, R. C.; Fuchs, G. D.; Awschalom, D. D. Single Spin Coherent in Semiconductors. In *Spintronics*; Dietl, T.; Awschalom, D. D.; Kaminska, M.; Ohno, H., Eds.; Elsevier: Amsterdam, 2008; pp. 4-5.
80. Mégy, R.; Bounouh, A.; Suzuki, Y.; Beauvillian, P.; Bruno, P.; Chappert, C.; Lecuyer, B.; Veillet, P. *Phys. Rev. B* **1995**, *51*, 5586-5589.
81. Gywat, O.; Krenner, H. J.; Berezovsky, J.; *Spins in Optically Active Quantum Dots*; Wiley-VCH: Weinheim, 2010; pp. 140-143.
82. Flatté, M. E.; Tifrea, I. *Manipulating Quantum Coherence in Solid State Systems*; Springer: Dordrecht, 2007; pp. 140-144.
83. Crooker, S. A.; Furis, M.; Lou, X.; Adelmann, C.; Smith, D. L.; Palstrom, C. J.; Crowell, P. A. *Science* **2005**, *30*, 2191-2195.
84. Hübner, J.; Oestreich, O. In *Spin Physics in Semiconductors*; Dyakonov, M. I., Ed.;



Springer: Berlin-Heidelberg, 2008; Vol. 157, pp. 123-129.

85. Kawakami, R. K.; McCreary, K.; Li, Y. Fundamentals of Spintronics in Metal and Semiconductor Systems. In *Nanoelectronics and Photonics: From Atoms to Materials, Devices, and Architectures*; Korkin, A.; Rosei, F., Eds.; Springer: New York, 2008; pp. 89-90.
86. Greilich, A.; Yakovlev, D. R.; Bayer, M.; Shabaev, A.; Efros, Al. L. Electron-Spin Dynamics in Self-Assembled (In,Ga)As/GaAs Quantum Dots. In *Electron Spin Resonance and Related Phenomena in Low-Dimensional Structures*. Fanciulli, M., Ed.; Springer: Berlin-Heidelberg, 2009; pp. 56-57.
87. Lou, X.; Adelmann, C.; Furis, M.; Crooker, S. A.; Palstrom, C. J.; Crowell, P. A. *Phys. Rev. Lett.* **2006**, *96*, 176603(1)-(4).
88. Kaftandjian, V. P.; Delsart, C.; Keller, J. C. *Phys. Rev. A* **1981**, *23*, 1365-1374.
89. Dyakonov, M. I.; Perel, V. I.; Theory of Optical Spin Orientation of Electrons and Nuclei in Semiconductors. In *Optical Orientation*; Meier, F.; Zakharchenya, B. P., Eds.; Elsevier: Amsterdam, 1984; pp. 39-47.
90. Hirsch, J. E. *Phys. Rev. Lett.* **1999**, *83*, 1834-1837.
91. Vignale, G. *J. Supercond. Nov. Magn.* **2010**, *23*, 3-10.
92. Murakami, S.; Nagaosa, N.; Zhang, S.-C. *Science* **2003**, *301*, 1348-1351.
93. Niimi, Y.; Morota, M.; Wei, D. H.; Deranlot, C.; Basletic, M.; Hamzic, A.; Fert, A.; Otani, Y. *Phys. Rev. Lett.* **2011**, *106*, 126601(1)-(4).
94. Karplus, R.; Luttinger, J. M. *Phys. Rev.* S. Murakami, N. Nagaosa, and S.-C. Zhang, *Science* *301*, 1348 (2003) **1954**, *95*, 1154-1160.
95. Gradhand, M.; Fedorov, D. V.; Zahn, P.; Mertig, I. *Phys. Rev. Lett.* **2010**, *104*, 186403(1)-(4).
96. Berger, L. *Phys. Rev. B.* **1970**, *2*, 4559-4566.
97. Smit, J. *Physica* **1955**, *21*, 877-887.
98. Smit, J. *Physica* **1958**, *24*, 39-51.
99. Tsurumi, T.; Hirayama, H.; Vacha, M.; Taniyama, T. *Nanoscale Physics for Materials Science*; CRC Press: Boca Raton, 2009; pp. 249-253.
100. Saitoh, E.; Ueda, M.; Miyajima, H.; Tatara, G. *Appl. Phys. Lett.* **2006**, *88*,

182509(1)-(3).

101. Hoffmann, A. *IEEE. Trans. Magnet.* **2013**, *49*, 5172-5193.
102. Hao, X.; Moodera, J. S.; Meservey, R. *Phys. Rev. B* **1990**, *42*, 8235-8243.
103. Moodera, J. S.; Meservey, R.; Hao, X. *Phys. Rev. Lett.* **1993**, *70*, 853-856.

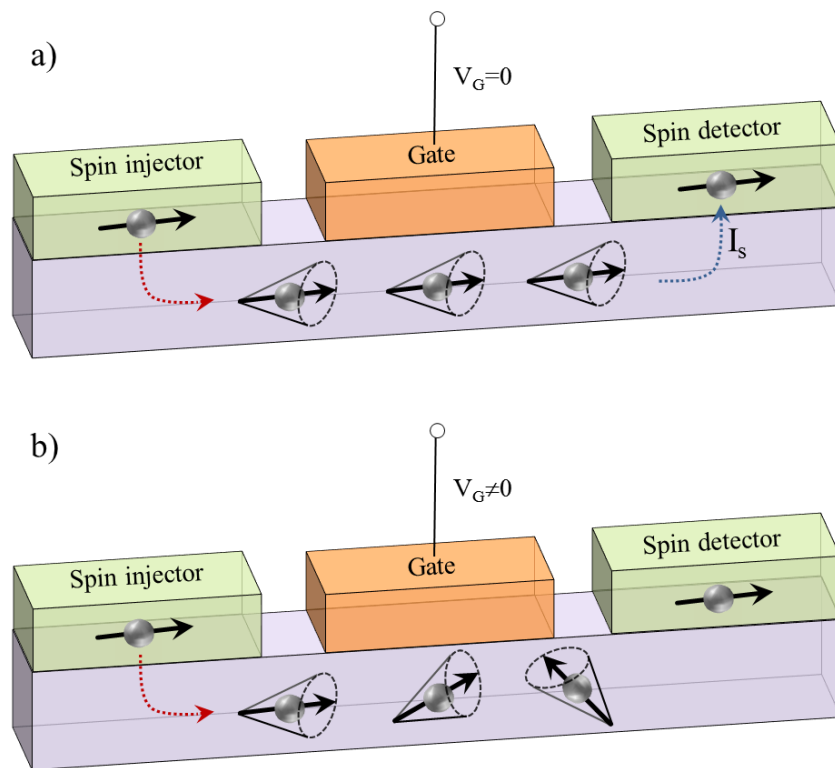


**Figure 1.1 The Datta-Das spin-field effect transistor.** Schematic diagram of a spin-FET showing the a) “on” and b) “off” states of operation. a) When the spin-FET is in the “on” state, an injected spin current passes through the semiconductor channel, maintains spin-polarization, and is read at the detector. This is the case for gate voltage,  $V_G = 0$ . b) When the spin-FET is in the “off” state, an applied gate voltage causes the injected spin current to precess and randomize so that no detectable spin current is present at the detector electrode.

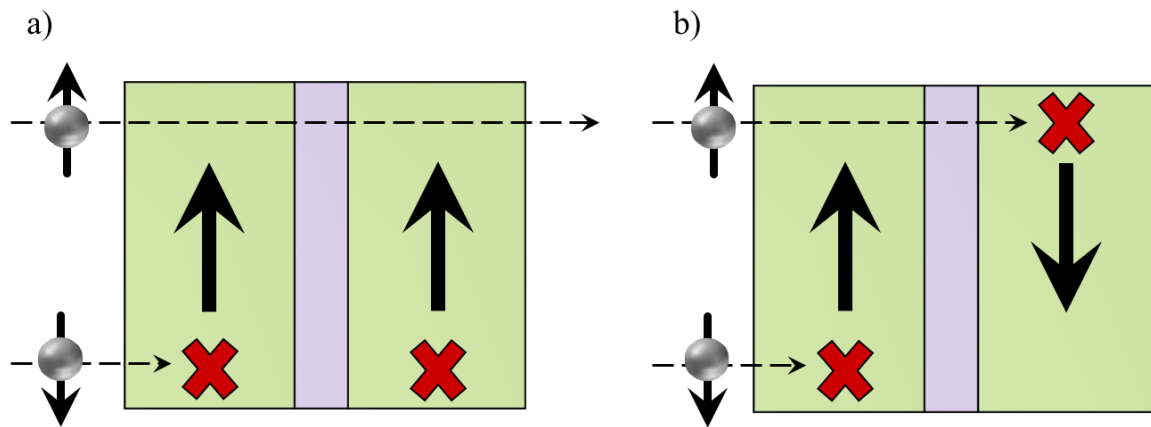


**Figure 1.2 Spin valve device schematic and operation principles.** Figure illustrating the possible operational configurations of a spin valve for a) when the two magnetic layers are aligned parallel to one another and b) when the magnetic layers are arranged antiparallel. In the parallel case, spin-polarized carriers with the same orientation as the magnetic layers will be able to pass through the device easily in a low-resistance channel. In the case where the magnetic layers are anti-aligned, both types of spin-polarized carriers (spin-up and spin-down) will be unable to pass through the spin valve, as both cases constitute high-resistance channels.

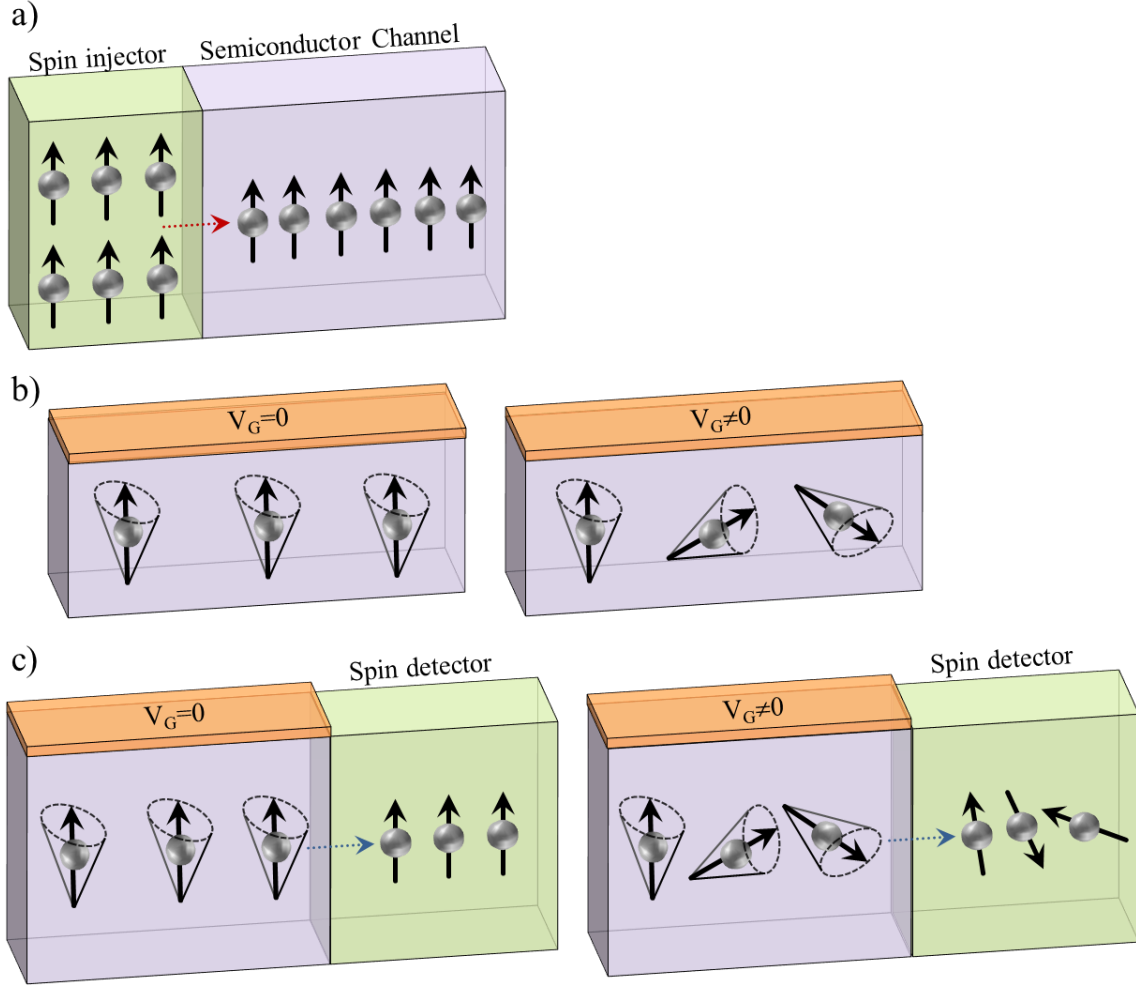


**Figure 1.3 Spin-dependent processes in a spin-FET.** Schematic illustrating the three-processes required for spin-FET operation: a) the injection of spin-polarized carriers, b) the transport of those carriers, and c) the detection of a spin-polarized current. Figure 1.3b also shows the behavior of the system in both the “on” (left) and “off” (right) states. According to Figure 1.3b, for an applied gate voltage, the spins will randomize and spin coherence is lost as an applied electric field enhances the Rashba spin-orbit coupling in the semiconductor channel. Figure 1.3c also shows the spin detection process in the absence (left) and presence (right) of a gate voltage. In this arrangement, the application of a gate voltage, which results in the randomization of spin-polarized carriers, translates to there being no coherent spin current measured via the detector.

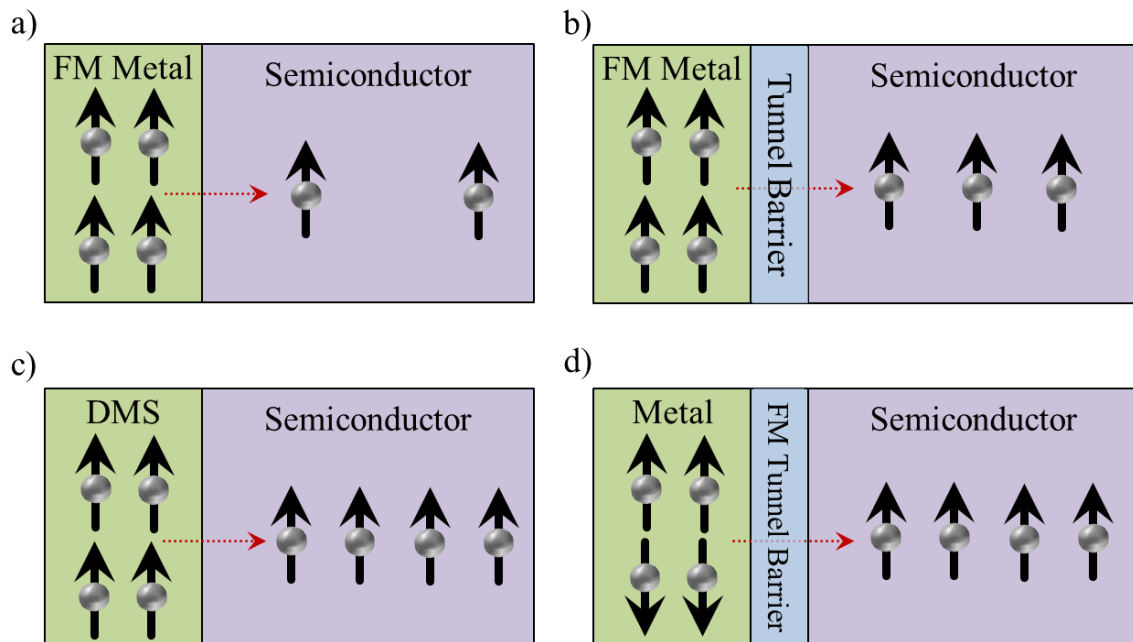


**Figure 1.4 Methods of electrical spin injection.** Illustration of the four main electrical spin injection techniques: a) spins are polarized in and injected from a ferromagnetic (FM) metal into a semiconductor channel, b) spins are polarized in and injected from a FM metal through an insulating tunnel barrier into the semiconductor channel, c) spins are polarized in a dilute magnetic semiconductor and are then directly injected into the semiconductor channel, and d) unpolarized electrons are injected through a dilute magnetic dielectric, ferromagnetic tunnel barrier into the semiconductor channel.

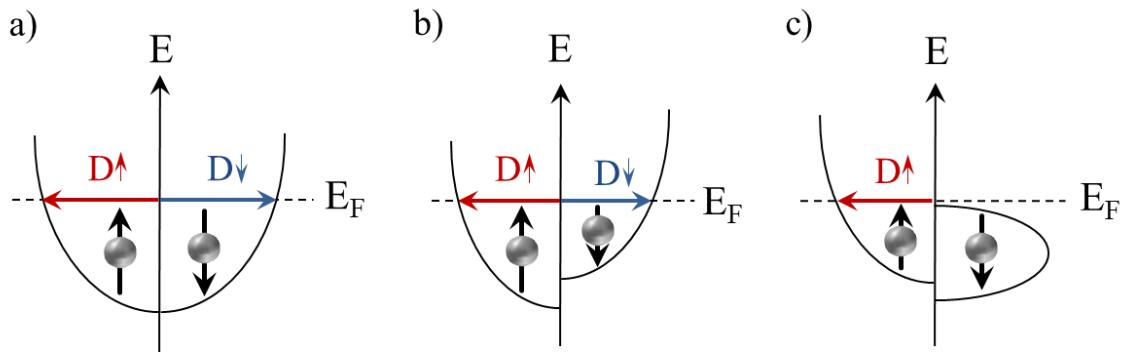


**Figure 1.5 Common spin injection materials: A density of states comparison:** Graphical representation of spin-up and spin-down densities of states for a) a traditional metal with no spin imbalance, b) a ferromagnetic metal where there is a difference in the number of spin-up and spin-down states, and c) a half-metallic metal where only one type of spin-state is filled at the Fermi energy, thereby allowing for a theoretical 100% polarized spin injection. In this figure,  $D$  indicates the density of states for spin-up (shown in red) and spin-down polarized electrons (blue).

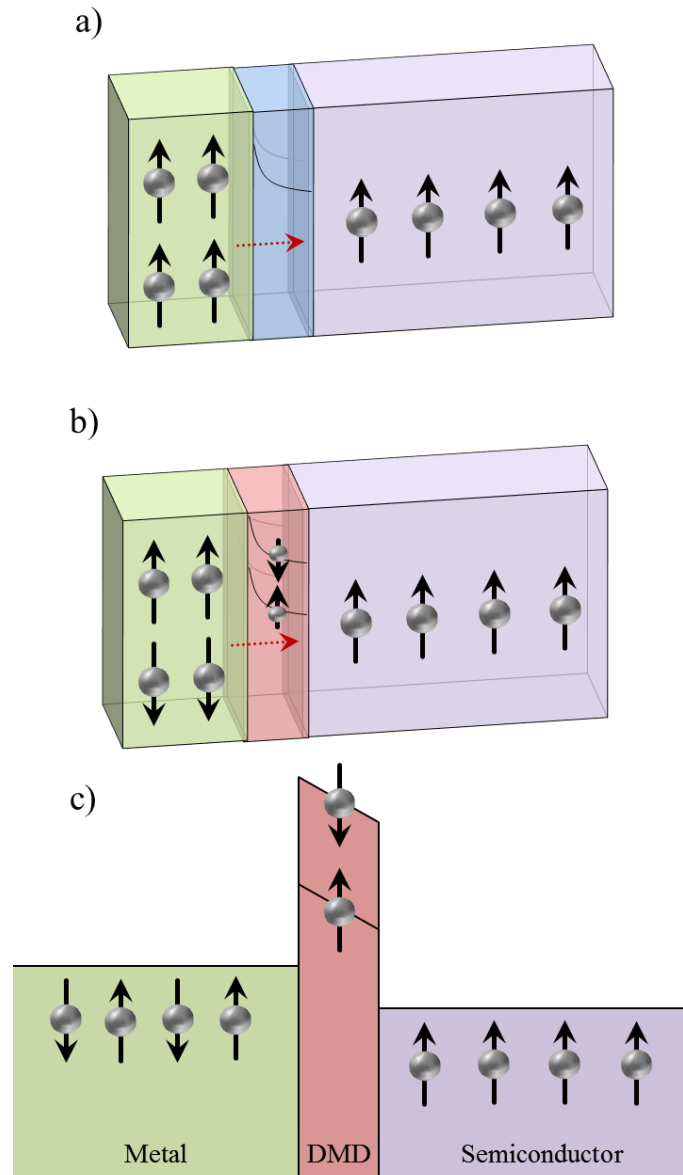


**Figure 1.6 Tunnel barriers for spin injection.** These figures illustrate the difference between different tunneling mechanisms for spin injection. In the case of a) a traditional oxide tunnel barrier, electrons are first polarized in a FM metal and are then tunneled into the semiconductor channel. For b) a dilute magnetic dielectric tunnel barrier, spins are unpolarized in the metal contact, but the tunneling energy requirements are different for spin-up and spin-down electrons.<sup>102,103</sup> As such, a spin-polarized current will be generated in the semiconductor upon tunneling. A side view of this DMD arrangement is shown in Figure 1.6c.



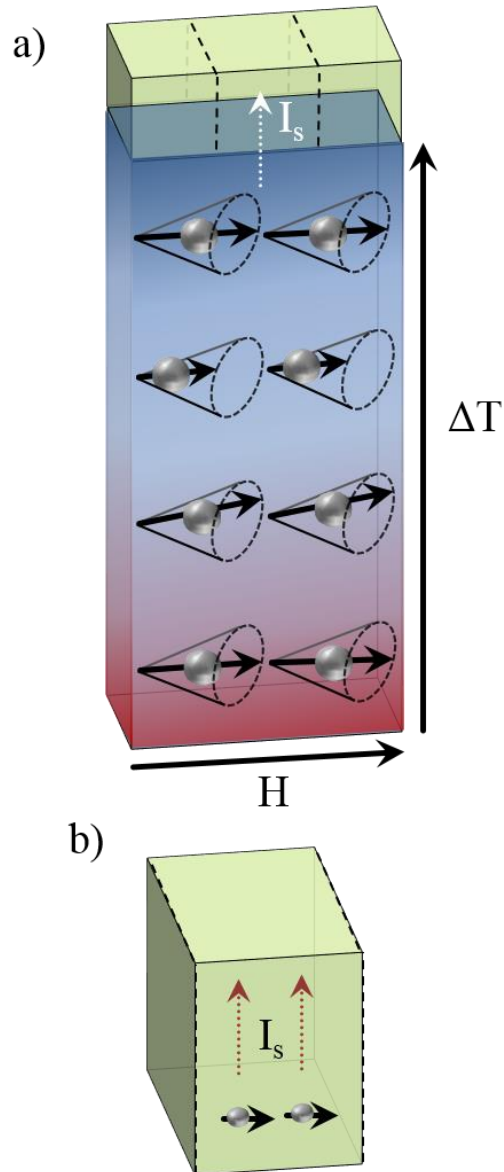


**Figure 1.7 Thermal spin injection: The magnon-mediated spin Seebeck effect.** Illustration showing a) the magnon-mediated spin Seebeck effect, in which a temperature gradient excites magnon motion in a ferrimagnetic insulator and b) the resulting pumping of spin current via magnon excitation at the interface of the heated material (the ferrimagnetic insulator, shown in temperature gradient) and the top, spin detection layer (shown in green).

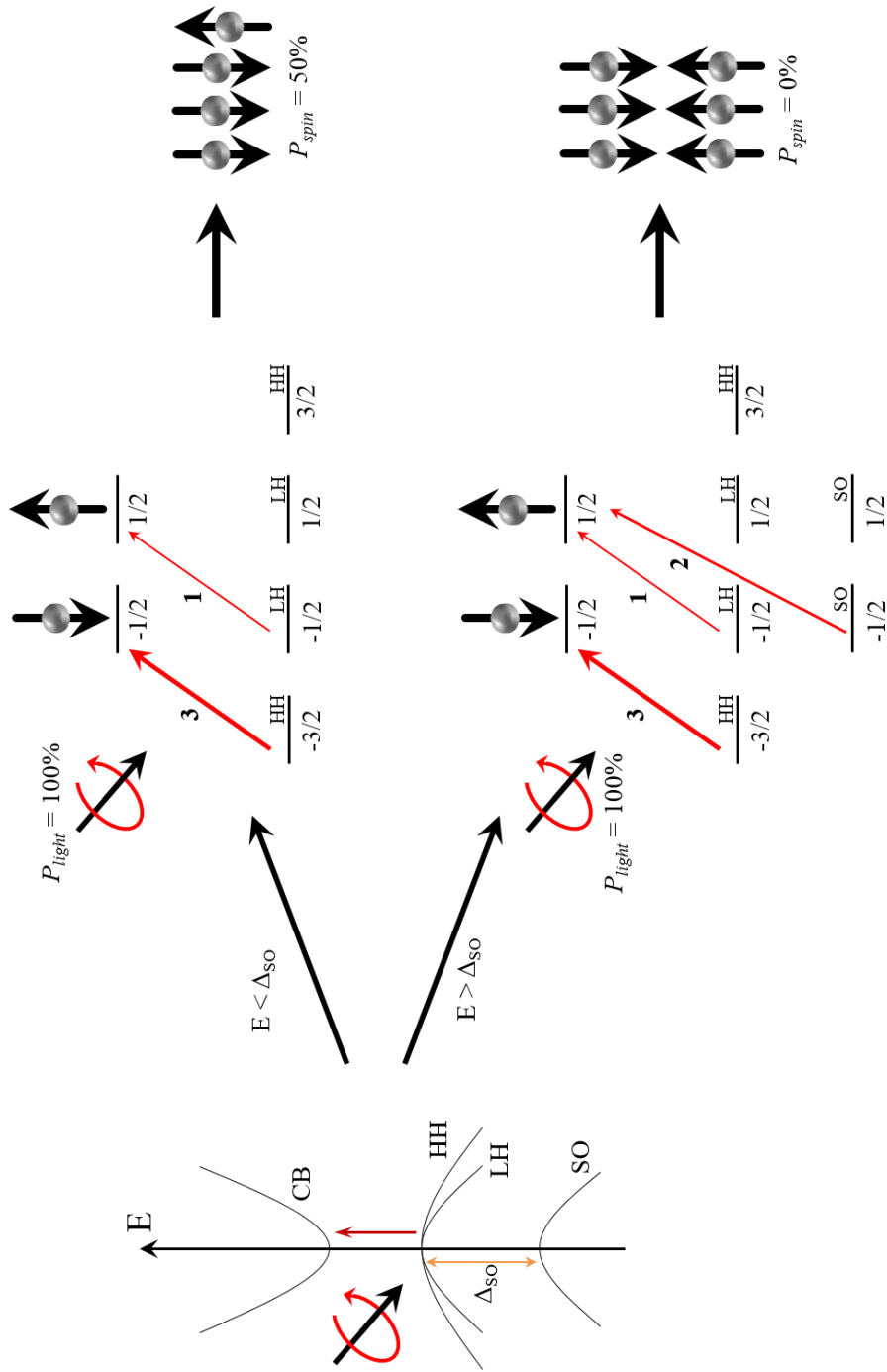


**Figure 1.8 Optical spin pumping.** The optical transition selection rules for the generation of spin current via circularly polarized light. If the energy of the light is less than the SO splitting, then a 50% polarized spin current is generated, as the transition for heavy holes (spin-down) is three times more likely than that of light holes (spin-up). If the energy is greater than the SO splitting, no spin-polarized current is generated, as there is an equal density of spin states (with the HH transition having a probability of 3, the LH transition having a probability of 1, and the SO transition having a probability of 2).

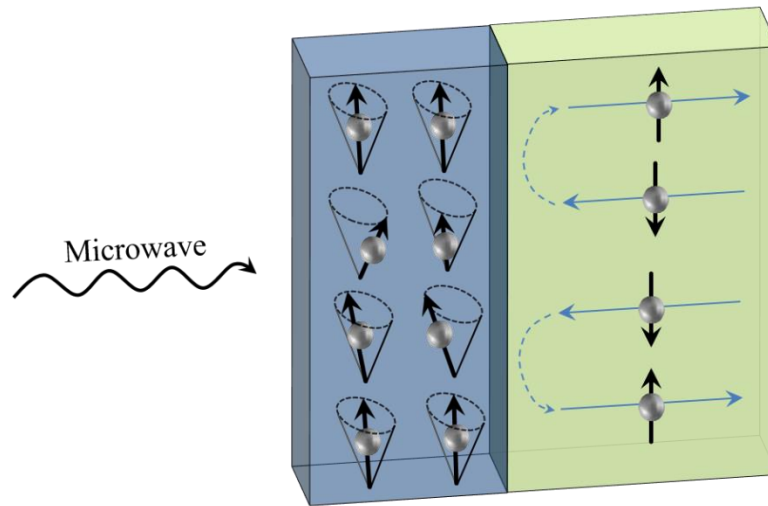


**Figure 1.9 Microwave spin pumping.** This schematic illustrates the process of microwave spin pumping. Microwave radiation is used to induce spin precession (in the layer shown in blue) and spin torque transfer between the injector (blue) and channel (green) layers allows for injection of a spin current.

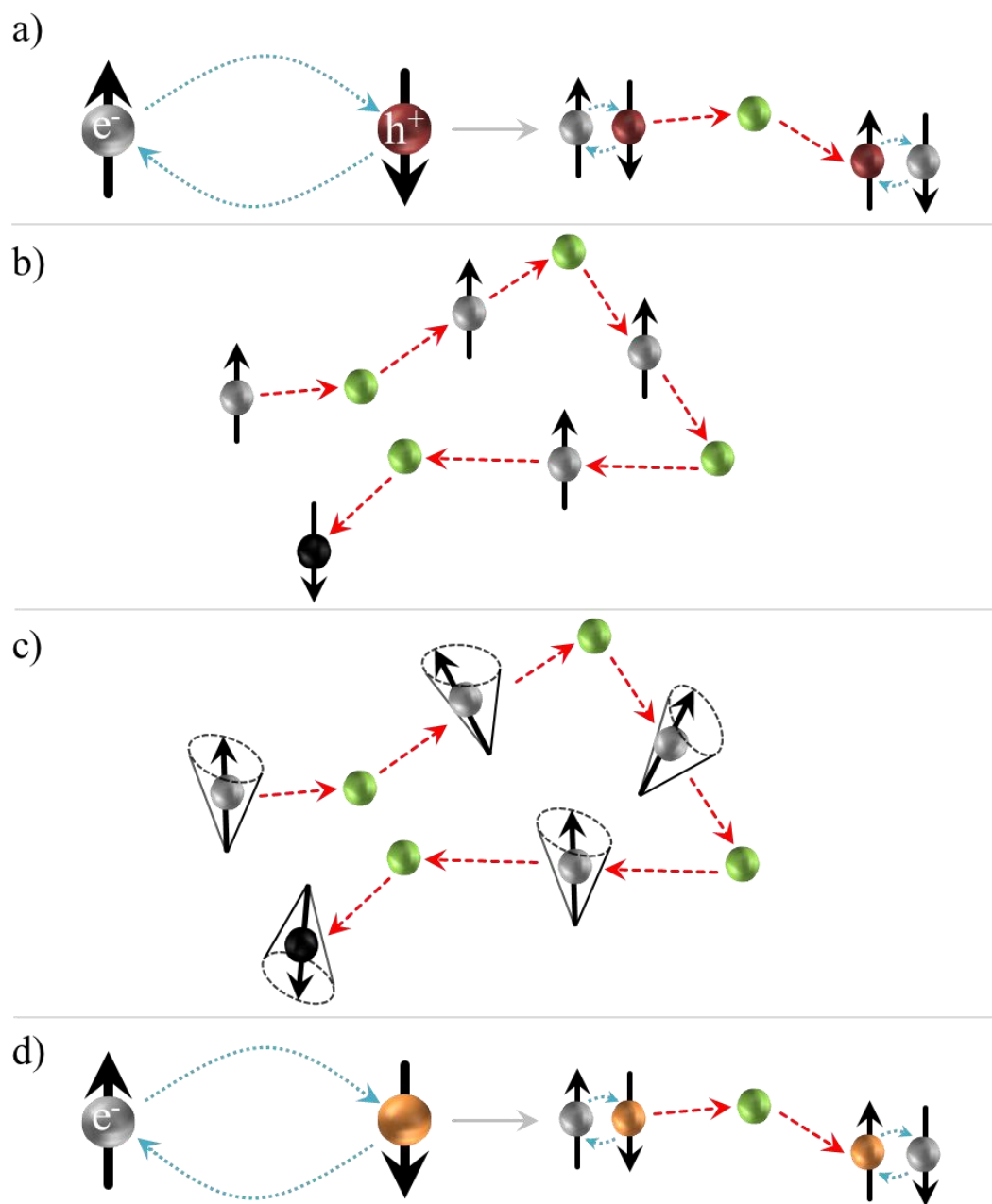


**Figure 1.10 Spin Relaxation Mechanisms.** Graphic illustrating the different spin relaxation mechanisms: a) Bir-Aronov-Pikus spin relaxation, b) Elliott-Yafet spin relaxation, c) Dyakonov-Perel spin relaxation, and d) Dzyaloshinskii-Moriya spin relaxation.

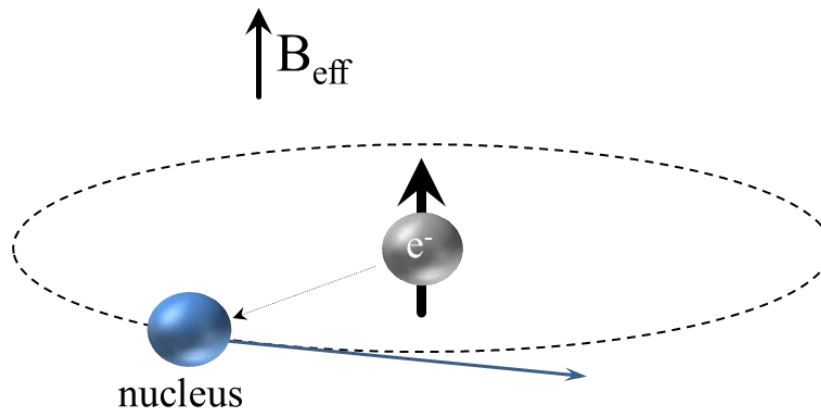


**Figure 1.11 Mechanism of spin-orbit interaction.** Illustration of the mechanism of spin-orbit interaction from an electron's frame of reference, in which an orbiting nucleus generates an effective, internal magnetic field. This field interacts and couples with the electron's spin orientation.

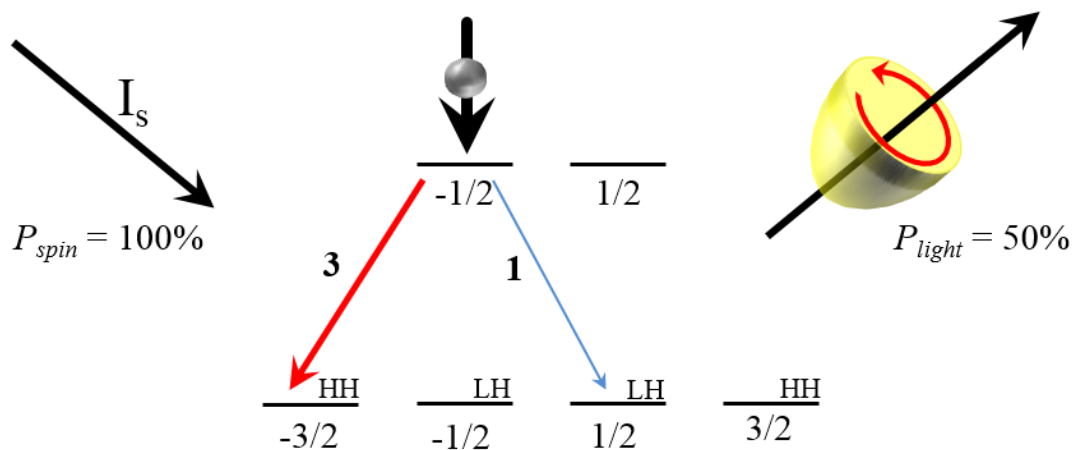


**Figure 1.12 Optical detection of spin-polarization.** Schematic showing the generation of circularly polarized light as a 100% polarized spin current is injected into a material (GaAs in this case). Because the recombination for heavy holes (HH) is 3 times as likely as the recombination for light holes (LH), a 50% circularly polarized light will be emitted.

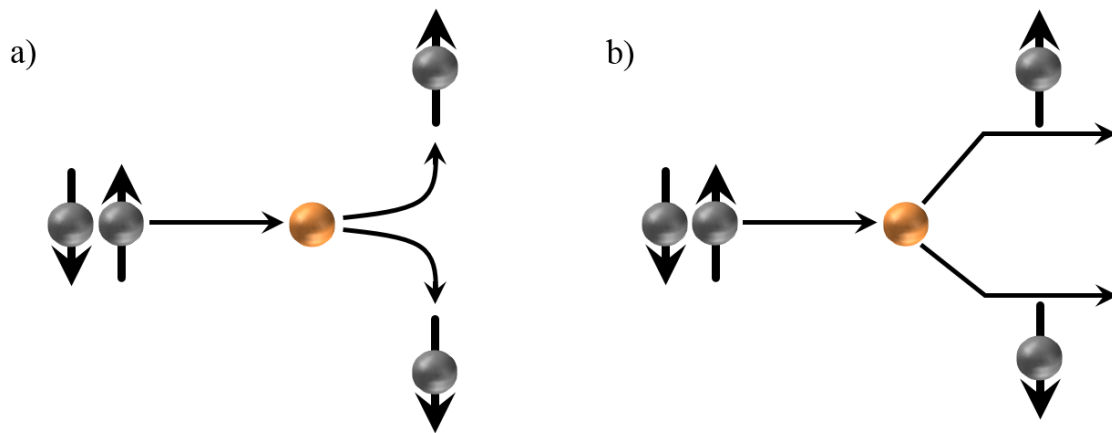


**Figure 1.13 Mechanisms of the extrinsic spin Hall effect.** Illustration showing the two main sources of extrinsic spin-orbit coupling in a system: a) skew-scattering and b) side-jump events. In each case, electrons with spin-up and spin-down orientations (both shown in gray) are scattered by impurities (orange), which scattering is dependent on their relative spin orientations.

## CHAPTER 2

### EXPERIMENTAL METHODS

The development of spin-FETs requires optimization of the three main spin processes present: spin injection, spin transport and manipulation, and spin detection. In order to study these spin-dependent phenomena, various materials, devices, and effects must be utilized. In this section, those techniques will be discussed. First, the fabrication of these materials to be studied is addressed. Because spin lifetime and diffusion length are often limited in most materials, on the order of picoseconds and nanometers, respectively, these materials are typically fabricated as thin films. The thin film materials studied herein are all in oxide-based systems. Oxides are ideal for device applications due to their relative stability, versatility, and ease of fabrication.<sup>1,2</sup> Thin film oxides are generally fabricated via a pulsed laser deposition (PLD) technique. For PLD, bulk ceramic pellets of the desired oxide composition are required, which are generally fabricated via a sol-gel technique. Following the deposition process, structural and elemental characterizations, including X-ray diffraction (XRD), X-ray absorption spectroscopy (XAS), X-ray photoelectron spectroscopy (XPS), atomic force microscopy (AFM), and UV-Vis transmittance spectroscopy, are performed. These techniques are briefly explained herein. In order to characterize the spin-dependent properties of the as-characterized oxide thin films, unique devices and experimental setups must be utilized to

study pertinent spin-related effects. These include the spin Seebeck effect, the Hanle effect, and inverse spin Hall effect.

### 2.1 Pulsed Laser Deposition and Sol-Gel Method

Pulsed laser deposition (PLD) is a nonequilibrium, thin film deposition technique in which a high energy, pulsed excimer laser is used to generate plasma that is deposited as a thin film on a substrate. More specifically, the pulsed laser is fired and the laser spot is focused onto a dense, ceramic target in a vacuum chamber (the PLD chamber). When this laser is focused onto the ceramic pellet, the surface of the pellet becomes superheated, allowing for the generation of plasma from the surface. This plasma, also referred to as the laser plume, moves normal to the ceramic target surface and will deposit on any exposed surface it reaches. If we position a substrate directly across from this ceramic target, the plasma will then deposit as a thin film on the substrate. Figure 2.1 shows a schematic of a PLD chamber in use.

Because PLD is a nonequilibrium technique, stoichiometry of the target is maintained in the thin film,<sup>3,4</sup> which makes PLD an ideal technique for growing complex and versatile oxides. Deposition of these materials starts with the fabrication of a bulk target of the desired stoichiometry, for which a sol-gel technique is used. In this method, shown in Figure 2.2, precursory oxide materials containing the desired elements are dissolved in water or nitric acid. Citric acid is then added to this solution as a chelating agent. The chelating agent prevents the constituent elements from clustering and precipitating out of solution during the refluxing of the solution. In refluxing, the solution is boiled for 24 hours. A condenser tube is used to prevent any loss of liquid during this



step – this glass tube has a large surface area and allows any steam boiled off to condense and fall back into the flask containing the solution. Following the refluxing, the solution is heated further to boil off the water. Once the water is removed, a gel remains, which is a mixture of the constituent elements and the chelating agent. As this solution is heated further, the organic chelating agent is burned out and a nanopowder containing the precursory elements is formed. To ensure no carbon remains in the powder, the material is then calcined at 600°C for several hours and this powder can then be pressed and sintered using a uniaxial press and a box furnace into a dense ceramic target for PLD.

Although the ceramic target stoichiometry is generally maintained, the thin film growth and the deposition rate may be optimized by modifying several deposition parameters during the PLD process. These include the substrate temperature, the laser pulse repetition rate, the rotation of the target during the ablation process, the laser energy, the presence of ambient gas (such as O<sub>2</sub> or N<sub>2</sub>) during the deposition, and the spot size of the laser on the ceramic target.<sup>3,4</sup> Each of these plays an important role in the deposition process and can have a large impact on the spin-dependent properties of the as-deposited thin films. In order to carefully monitor and study the impact of deposition parameters on film growth, all of the samples tested herein were deposited one by one using PLD.

The substrate temperature may be increased in order to aid in the oriented, crystalline growth of the thin film. An increased temperature will also promote film uniformity and homogeneity. These benefits must be balanced with other deposition parameters such as oxygen pressure, so that the deposited material maintains oxygen stoichiometry. The laser pulse repetition rate controls how quickly the ceramic target is

ablated. As the laser superheats the surface of the ceramic, crystallographic re-orientation may occur and the composition at the surface of the ceramic target may become slightly oxygen deficient. Because of this, the target can be rotated during the deposition process, so as to ensure a uniform composition of target material throughout the deposition. Additionally, both the laser pulse repetition rate and the target rotation must be considered in order to alter the deposition rate; that is, the average layer thickness, in nm or Angstroms, deposited per laser pulse.

Similarly, the laser energy density, or laser energy per spot size, has a huge impact on the deposition rate. As the energy density controls the size of the plume generated, it correlates directly to the rate at which films are deposited. However, increasing the energy significantly can also cause the plume to have a “splattering” effect, where the ejected material has such a high energy that it may cause a nonuniform deposition and/or increase the roughness of the as-deposited film. The final deposition parameter to be discussed is the oxygen pressure present during deposition. As mentioned previously, the deposition relies on the presence of oxygen in the chamber in order to maintain oxygen stoichiometry. Additionally, the deposition parameters may be modified in order to intentionally induce oxygen vacancies or other defects.<sup>5</sup> Because of this careful interplay of parameters, it is critical that each film deposited be characterized both structurally and elementally in order to fully understand the impact of the deposition parameters.

## 2.2 Thin Film Characterization Techniques

Following deposition, the thin films are characterized according to their elemental composition and phase, optical transparency, and roughness. These characterizations are critical in order to understand the quality of film growth, the thickness of the films, the possibility of contamination or dopants, and the overall effectiveness of the deposition process. Additionally, the information garnered from these techniques can be used as a baseline for modifying future deposition parameters. As such, these techniques are critical for understanding the thin film system completely. The methods used to complete these characterizations are described in the sections below.

### 2.2.1 X-ray Diffraction

In X-ray diffraction (XRD), X-rays are diffracted from the crystallographic lattice. If the diffraction of the X-rays meets Bragg's condition ( $n\lambda = 2d \sin \theta$ ), there is constructive interference, leading to peaks in the intensity spectra.<sup>6,7</sup> These peaks indicate different crystallographic orientations of various elements. This technique can tell us qualitatively if we have formed the desired composition and can be used to determine the phase and the structure of the material. This technique is not quantitative – meaning that it is not highly efficient at distinguishing the respective concentrations of elements in the formed films. Because of this, XRD has been used herein to confirm conformal or epitaxial growth of thin films as well as to rule out the possibility of high-concentration impurity formation. A schematic representation of this technique is shown in Figure 2.3a.

### 2.2.2 X-ray Photoelectron Spectroscopy

X-ray photoelectron spectroscopy (XPS) is a commonly used technique for determining the composition of the surface of a sample, as the penetration depth for this technique is typically ~10 nm.<sup>8</sup> Information gathered can be used to investigate the oxidation state of the elements present in the thin films. In this technique, X-rays are used to excite electrons from core-shell positions. These electrons are emitted as photoelectrons and are collected upon emission. These collected photoelectrons give a spectrum of intensities as a function of binding energy, with the peaks in intensity indicating the presence of an element with a specific oxidation state (Figure 2.3b). The individual elements can be defined by the binding energy at which the peaks in intensity occur. This technique is used to quantitatively investigate the elements present as well as their oxidation states in order to determine the composition of the films grown as well as gain knowledge about any surface impurity states present in the films.

### 2.2.3 X-ray Absorption Spectroscopy

X-ray absorption spectroscopy (XAS) is a unique tool used to gather information about the elements present in a thin film – including their oxidation state and their grain size. In XAS, high energy X-rays are absorbed by the material being studied. A specific energy edge (e.g., the K-edge or L-edge) is probed and the number of X-rays absorbed is measured (Figure 2.3c). In XAS, there are three main regions of interest, each of which is analyzed individually (see Figure 2.4). The three main areas to examine are: the below-edge structure, the X-ray absorption near-edge structure (XANES), and the extended X-ray absorption fine structure (EXAFS).<sup>9</sup> The below-edge segment contains information

about material, indicating whether the edge being probed is for a metal (contains information about states near the Fermi energy) or an insulator (contains information about core excitons). The near-edge (XANES) contains information about the element probed, as the information is gathered from the transition of core electrons to weakly bound states. The EXAFS contains information about the bonding in the material and, in this region, emitted photoelectrons are only weakly scattered, because of their relatively large energies. This technique requires high energy X-rays and is often performed at national laboratories. For the experiments reported herein, the XAS source at the Advanced Photon Source at Argonne National Lab was utilized. For reporting and analysis, X-ray absorption spectra can be plotted in many different ways. Data are typically reported as intensity versus incident energy. However, they can also be transformed to k-space or R-space to give further information about the arrangement or structure of atoms in the thin films. This technique is highly powerful and is used to determine the various oxidation states of elements as well as probe their respective concentrations and cluster sizes.

#### 2.2.4 Atomic Force Microscopy

Atomic force microscopy (AFM) is used to examine the surface texture of a material. In this technique, a fine-point cantilevered tip is used to probe a material surface by measuring the interaction energy between the tip of the cantilever and the surface in order to determine the texture of the surface. This technique is often used to quantify the quality of film growth – that is, to show roughness, investigate the growth method (island or layer-by-layer growth), and investigate the thickness of patterned thin films.

### 2.2.5 UV-Vis Spectroscopy

Ultraviolet-Visible spectroscopy (UV-Vis) is used to determine the optical transparency of thin films. UV-Visible range light is passed through the thin film to a detector. This detector measures the light intensity relative to the incident intensity and determines how much of the light was transmitted. This technique can tell us information about the optical transparency and the bandgap of certain materials, and can give information about mid-gap states.

### 2.2.6 The Hall Effect

In order to characterize the electrical behavior of thin films, the Hall effect is used. In this testing, a current is passed across a sample along the 'z'-axis, as in Figure 2.5, an external magnetic field is then applied in the 'x' direction, and the voltage is measured in the 'y' direction. Because of the movement of electrons in a magnetic field, they will encounter a Lorentz force that will cause the electrons to be deflected from their intended path, perpendicular to the flow of current, towards the transverse ends of the film, where the voltage measurement is indicated.<sup>10</sup> This technique can be used to determine the dominant carrier type, the carrier concentration, their mobility, and the diffusion coefficient of these carriers.

## 2.3 The Spin Seebeck Effect

Following initial thin film characterizations, the spin-dependent effects can be probed. As mentioned in the spin injection section, thermal spin injection can be achieved via the spin Seebeck effect. Using an arrangement as shown in Figure 2.6, a lateral

temperature gradient through the thickness of the sample and an out-of-plane magnetic field can be used to generate an orthonormal voltage in the thin film.<sup>11</sup> This technique can be used to thermally inject spin current and it can also be used to measure the spin detection properties of thin films, as the voltage generated is a measure of conversion between spin and charge current in the thin film layer according to the inverse spin Hall effect, which will be outlined in the Section 2.5. The voltage signal is anticipated to be on the order of nanovolts to microvolts.

## 2.4 The Hanle Effect

The Hanle effect has long been used to determine spin lifetime and spin diffusion properties in various materials, such as Si and GaAs.<sup>12,13</sup> This effect is defined as a decay in spin accumulation caused by application of an external magnetic field perpendicular to the direction of spin-polarization. This external field causes spin precession and thus spin relaxation over time. A Hanle device operates on the principles of drift and diffusion in a material, approximated according to eq. (2.1):

$$V \propto \int_0^{\infty} \left[ \frac{1}{2\sqrt{\pi Dt}} \cdot e^{-[(L-vt)^2/(4Dt)]} \cdot e^{-(t/\tau_s)} \right] \cdot \cos(\omega t) dt, \quad (2.1)$$

where V is the voltage signal generated, D is the diffusion coefficient, t is the time, L is the length of the sample, v is the velocity of the spin-polarized carriers,  $\tau_s$  is the spin lifetime, and  $\omega$  describes the precession of spins according to the external magnetic field.<sup>14</sup> In a Hanle experiment, spin-polarized carriers are injected into a channel, and

then drift and diffuse away from the local high point in concentration until the spin-polarization decays as a function of the spin relaxation mechanisms present in the material. In the presence of an external, out-of-plane magnetic field, however, this decay is enhanced as the spins begin to precess about this field, causing the spin-polarized carriers to decay more quickly, directly as a function of the magnitude of the external magnetic field. To study how the spin-polarization decays with application of this field, in order to determine spin lifetime and diffusion, the Hanle effect must be studied in an electrical device. The two most common ways to probe this behavior are the three- and four-terminal Hanle devices.

#### 2.4.1 Three-Terminal Hanle Effect

The three-terminal (3T) Hanle device is shown in Figure 2.7. In this arrangement, spin-up polarized carriers are injected into the semiconductor channel by 1) first polarizing spins in a FM contact and then 2) passing a current between this and a second, nonmagnetic contact. As current is passed, the spin-up polarized carriers inject into the channel and there is a resulting accumulation in spin-polarization beneath the injector contact. Spin-polarized carriers then begin to diffuse away from the injection point. However, the first and third contacts, on the far left and right sides of the device, are positioned far enough away such that the spins decay before reaching these contacts. Therefore, there is a local imbalance in the spin concentration between the second and third contacts, with spin-up carriers being significantly concentrated beneath the centermost contact. As such, as long as a spin-polarized current is being passed, a voltage can be measured between these contacts.



Despite the straightforwardness of this experiment, it has faced scrutiny over the last several years for providing inaccurate data. Although the reason behind this discrepancy remains unclear, it has been postulated that the use of a local arrangement complicates the signal. As such, we are unsure if the spin lifetime we are probing is the spin lifetime in the channel or is the spin lifetime in the FM-injector contact.<sup>15,16</sup> As such, the alternative, nonlocal four-terminal geometry was proposed.

#### 2.4.2 Four-Terminal Hanle Effect

As an alternative to the 3T geometry, the four-terminal (4T) Hanle device has shown much promise. In the four-terminal arrangement, as shown in Figure 2.8, spins are polarized in a FM contact and then injected by passing a current between this contact and a nonmagnetic contact (contact 1), similar to the 3T geometry. However, as the local spin accumulation builds up beneath the injector contact (contact 2), and the spin-polarized carriers diffuse away from this point, contact 3 is positioned close enough to contact 2 such that the spin-polarized carriers can transport beneath contact 3. Thus, there is also a local spin accumulation beneath contact 3 while a spin-polarized current is being passed and a measureable voltage is generated between contacts 3 and 4. By applying an external, out-of-plane magnetic field, the spins begin to precess and will then decay according to relaxation mechanics. This arrangement is referred to as the nonlocal Hanle arrangement because, in comparison to the 3T Hanle effect, the spin accumulation is not measured beneath the injection point, but at some nonlocal point relative to the spin injector contact.

The Hanle voltage behavior will experience a Lorentzian decay as a function of

the external, out-of-plane magnetic field (Figure 2.9) that will depend on  $d$ , the separation between contacts 2 and 3. The shape of the curve will either show a purely Lorentzian shape (Figure 2.9a), as predicted according to equation 2.1, or it will show a Lorentzian curve with damped oscillations in the tails, as has been predicted and measured for two different inner contact separation distances,  $d$  (Figure 2.9b).<sup>17</sup> These two cases correspond to a short- $d$  inner contact separation and a long- $d$  inner contact separation, for Figure 2.9a and Figure 2.9b respectively. By adapting and fitting the drift-diffusion equation, eq. 2.1, to the Hanle curve, the spin lifetime can be determined. From this, spin diffusion length and spin relaxation rate can be calculated and the transport can be attributed to the various spin relaxation mechanisms described in Section 1.3. Typical values of the spin lifetime range between 100's of picoseconds and a few nanoseconds, giving typical values of spin diffusion length on the range of nanometers.

In addition to the electrical Hanle effect, these measurements can also be performed using polarized light – the optical Hanle effect. This effect is tested in much the same way, except the injected spin current is measured via light polarization. These tests will show the same Lorentzian behavior as a function of the external, out-of-plane magnetic field. Either optically or electrically, the Hanle effect remains the most popular way to investigate spin relaxation mechanics and to measure the spin lifetime in a material. The specific structure used for testing herein will be explained further in Section 4.1.3.

## 2.5 The Inverse Spin Hall Effect

The spin Hall effect was previously defined as the conversion from charge current to spin current, which can occur intrinsically or extrinsically as a function of the SOC in the material or the SOC due to impurities, respectively.<sup>18-20</sup> Similarly, the inverse spin Hall effect (ISHE) can also be intrinsic or extrinsic, depending on the nature of the SOC in the system. The ISHE refers to the conversion from spin current to charge current. This effect is particularly used for spin detection applications, as this conversion gives a voltage that is readable via traditional electrical measurements. For an all-electrical system, in which spin-polarized carriers are injected and detected via traditional electrical measurement, the ISHE can be measured according to Figure 2.10. In this schematic, a polarized spin current is injected into and transported through a channel. As this current transports through the material, the SOC generates a transverse charge current. The SOC of the system can be described by the spin Hall angle ( $\theta_{SH}$ , SHA), which is a measure of the ratio of spin Hall conductivity to charge conductivity,  $\theta_{SH} = \sigma_{SH} / \sigma_e$ . In this equation, the spin Hall conductivity is defined as the ratio of spin current passed through a sample to the electric field generated by the ISHE in the transverse direction.<sup>21</sup> This can be measured by measuring the voltage response in a system where the electrical conductivity is known. The electrical conductivity can be determined via four-point probe testing.

The ISHE can also be used to detect spin currents injected via alternative means – either electrically, thermally, or via microwave spin pumping. For use in traditional spin-FET devices, detection of electrically generated spin currents will be the focus herein, with the primary goal of these studies to investigate the spin Hall angle and spin Hall conductivity in oxide semiconductor thin films. Additionally, the detection of thermal

spin injection will also be discussed. Using the techniques outlined herein, the following chapters discuss the growth, structural and electrical characterizations, and the spin-dependent phenomena which occur in a variety of both standard and complex oxide systems.

## 2.6 References

1. Opel, M. *J. Phys. D: Appl. Phys.* **2012**, *45*, 033001(1)-(31).
2. Bibes, M.; Barthélémy, A. *IEEE Trans. Electron Devices* **2007**, *54*, 1003-1023.
3. Kumar, D.; Sankar, J.; Narayan, J.; Synthesis and Characterization of Metal-Ceramic Thin Film Nanocomposites with Improved Mechanical Properties. In *Nanoengineering of Structural, Functional, and Smart Materials*; Schulz, M.; Kelkar, A.; Sundaresan, M., Eds.; CRC Press: Boca Raton, 2006; pp. 248-254.
4. Eason, R.; *Pulsed Laser Deposition of Thin Films: Applications Led-Growth of Functional Materials*; John Wiley & Sons: Hoboken, 2007; p. 5.
5. Xu, Q.; et al. *Appl. Phys. Lett.* **2008**, *92*, 082508(1)-(3).
6. Bragg, W. H.; Bragg, W. L. *Proceed. Royal Society London Series A* **1913**, *88*, 428-438.
7. Cullity, B. D.; *Elements of X-ray Diffraction*, 2; Addison-Wesley Publishing Group: Reading, MA, 1973; pp. 82-87.
8. Zhang, S.; Li, L.; Kumar, A. *Materials Characterization Techniques*. CRC Press: Boca Raton, 2008; pp.27-34.
9. Yano, J.; Yachandra, V. K. *Photosynth. Res.* **2009**, *102*, 241-254.
10. Ramsden, E. *Hall Effect Sensors: Theory and Application*; Elsevier: Oxford, 2006, pp. 1-5.
11. Uchida, K.; Adachi, H.; Ota, T.; Nakayama, H.; Maekawa, S.; Saitoh, E. *Appl. Phys. Lett.* **2010**, *97*, 172505(1)-(3).
12. Dash, S. P.; Sharma, S.; Le Breton, J. C.; Peiro, J.; Jaffrés, H.; George, J.-M.; Lemaître, A.; Jansen, R. *Phys. Rev. B* **2011**, *84*, 054410(1)-(11).
13. Furis, M.; Smith, D. L.; Kos, S.; Garlid, E. S.; Reddy, K. S. M.; Palstrom, C. J.; Crowell, P. A.; Crooker, S. A. *New J. Phys* **2007**, *9*, 347(1)-(18).
14. Huang, B.; Appelbaum, I. *Phys. Rev. B* **2008**, *77*, 165331(1)-(6).
15. Aoki, Y.; et al. *Phys. Rev. B* **2012**, *86*, 081201(1)-(4).
16. Tezuka, N.; Saito, T.; Matsuura, M.; Sugimoto, S. *IEEE Trans. Magnet.* **2014**, *50*, 2600204(1)-(4).

17. Roundy, R.; Prestgard, M. C.; Tiwari, A.; Mishchenko, E. G. Raikh, M. E. *Phys. Rev. B* **2014**, *90*, 115206(1)-(10).
18. Vignale, G. *J. Supercond. Nov. Magn.* **2010**, *23*, 3-10.
19. Murakami, S.; Nagaosa, N.; Zhang, S.-C. *Science* **2003**, *301*, 1348-1351.
20. Niimi, Y.; Morota, M.; Wei, D. H.; Deranlot, C.; Basletic, M.; Hamzic, A.; Fert, A.; Otani, Y. *Phys. Rev. Lett.* **2011**, *106*, 126601(1)-(4).
21. Sahin, C.; Flatté, M. E. *Phys. Rev. Lett.* **2015**, *114*, 107201(1)-(5).

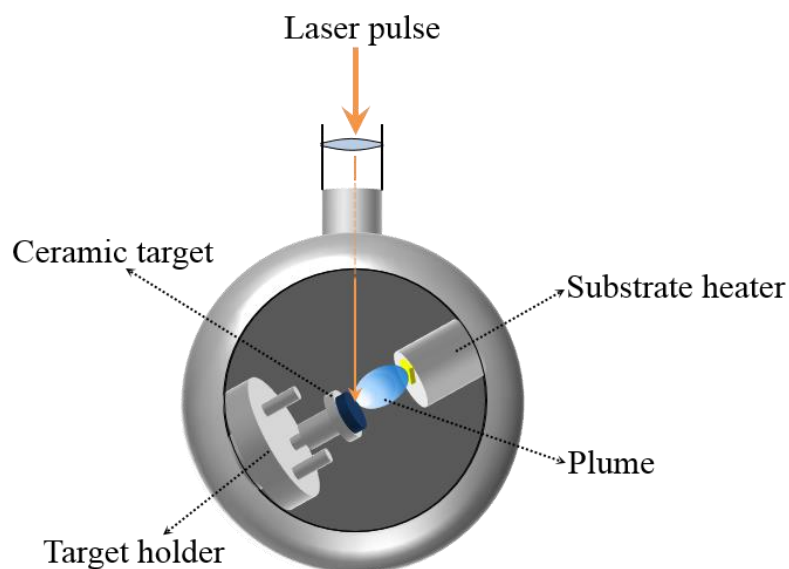


**Figure 2.1 Pulsed laser deposition schematic.** Illustration showing the pulsed laser deposition process in which a high-energy excimer laser is focused on a dense ceramic target in a vacuum chamber. This turns the target material to a plasma; a plume that deposits on a heated substrate positioned opposite the target.

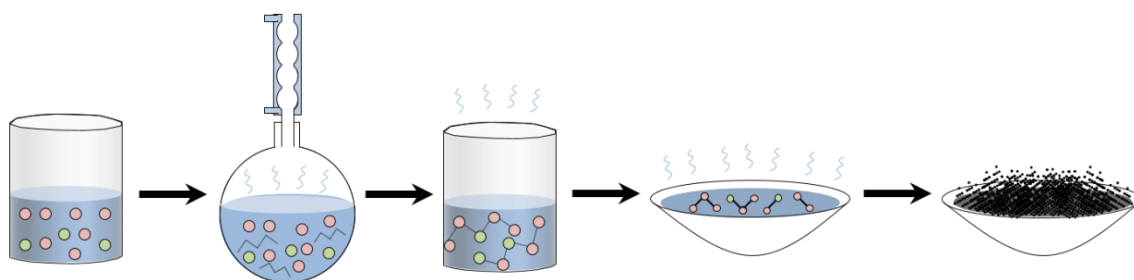


**Figure 2.2 Sol-gel process for nanopowder fabrication.** Schematic of the sol-gel process, including the following steps: dissolving precursory oxides in water and nitric acid, refluxing the solution for 24 hours, heating the solution to remove the water, gelation, and burning out the chelating agent to form the final nanopowder product.

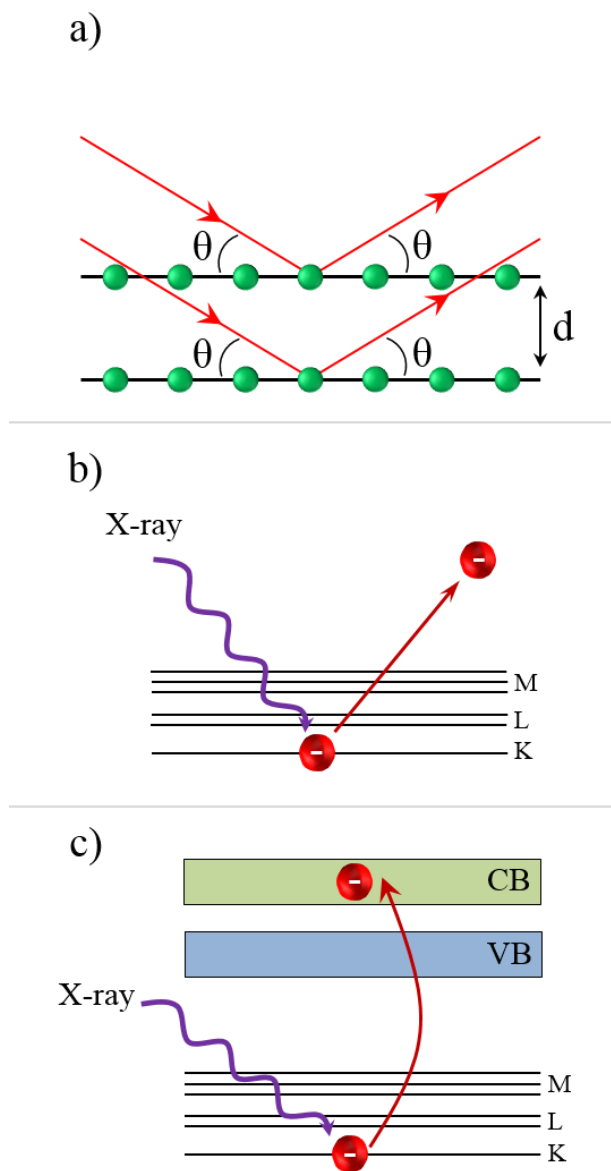


**Figure 2.3 X-ray diffraction, X-ray photoelectron spectroscopy, and X-ray absorption spectroscopy.** Figure showing the mechanism the three X-ray-dependent processes used for characterization: a) X-ray diffraction, where X-rays are diffracted off the crystal lattice, b) X-ray photoelectron spectroscopy, where a high energy X-ray exciting a core electron emits a photoelectron, and c) X-ray absorption spectroscopy, where a high energy X-ray excites an electron from the valence-band to the conduction band.



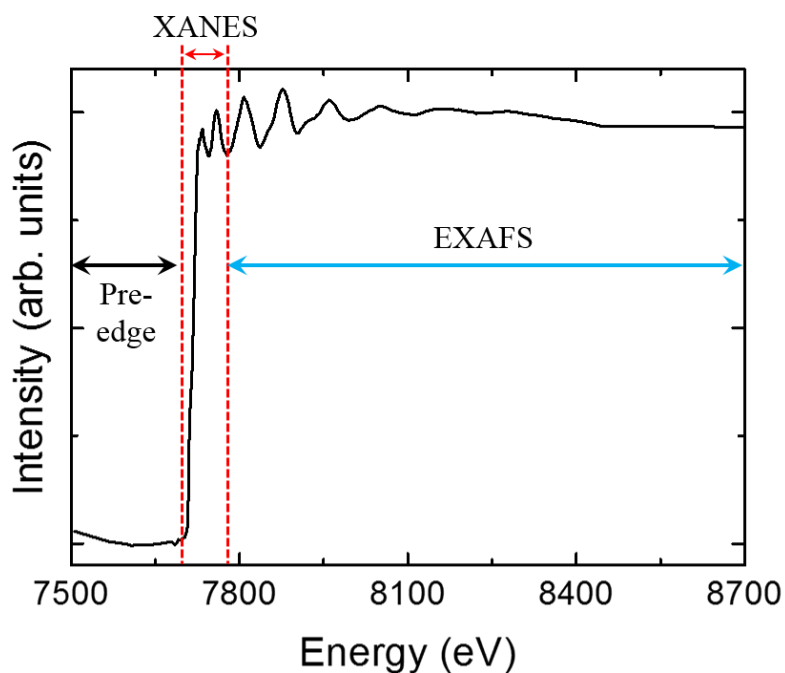


**Figure 2.4 X-ray absorption spectrum.** Graph showing the main regions of interest in X-ray absorption spectra. The regions include the pre-edge, the absorption near edge (XANES), and the extended absorption fine structure (EXAFS). Each region contains different information about the element being probed, including its identity, its oxidation state, and its cluster or agglomerate size.

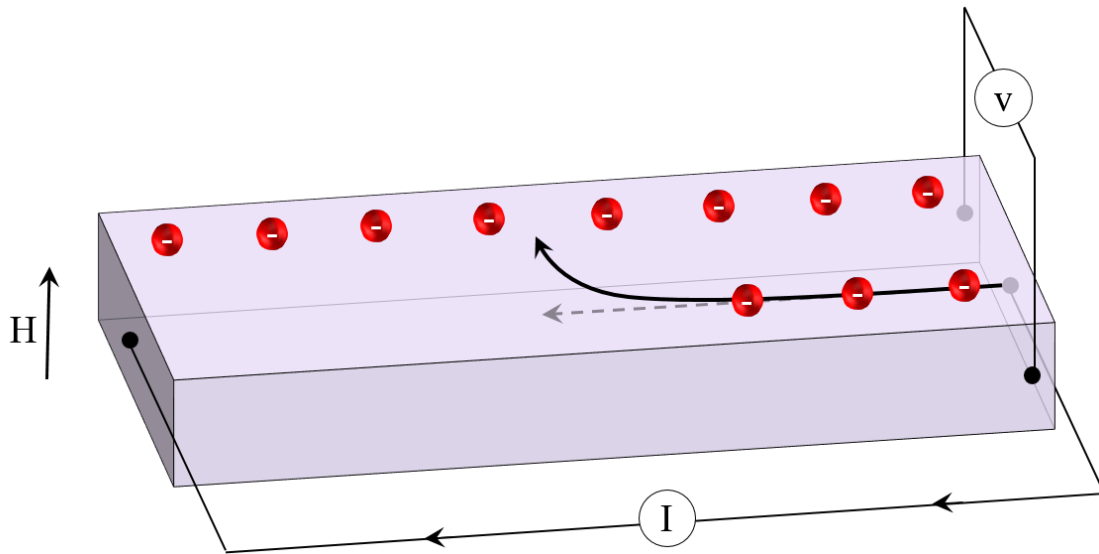


**Figure 2.5 The Hall effect.** Representation of the Hall effect in an n-type material. For a current applied left-to-right, electrons move right-to-left. If an external magnetic field is applied through the thickness of the thin film, the electrons are deflected towards the front and back of the device, such that a voltage is measureable across the sample, as depicted above.

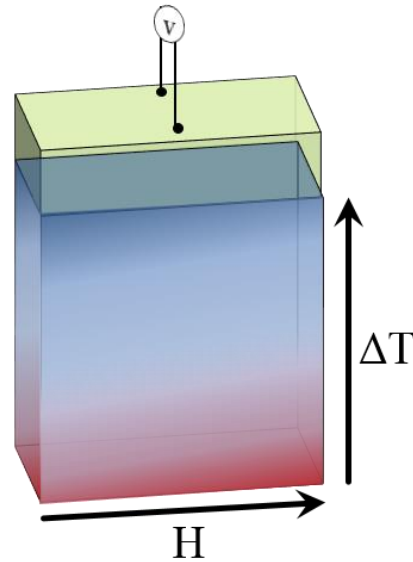


**Figure 2.6 The spin Seebeck effect.** Illustration of a SSE device in operation. A temperature gradient is applied through the thickness of the sample, a field is applied left-to-right, and a voltage is measured across the front and back (as shown) of the sample.

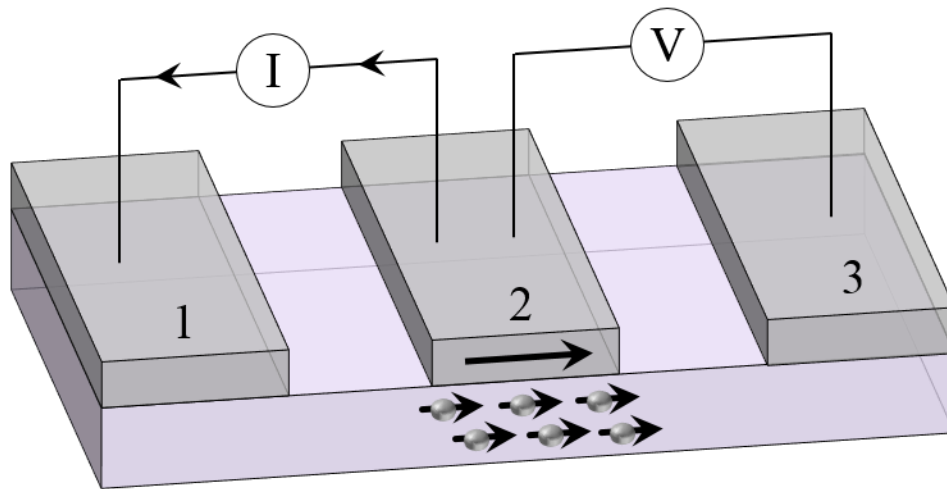


**Figure 2.7 The three-terminal Hanle effect.** Schematic showing the 3T Hanle geometry, in which spins are polarized in contact 2 (center) and are injected by passing a current between contacts 1 and 2 (left and center, respectively). The accumulation of carriers beneath contact 2 is measured by measuring the voltage between contacts 2 and 3.

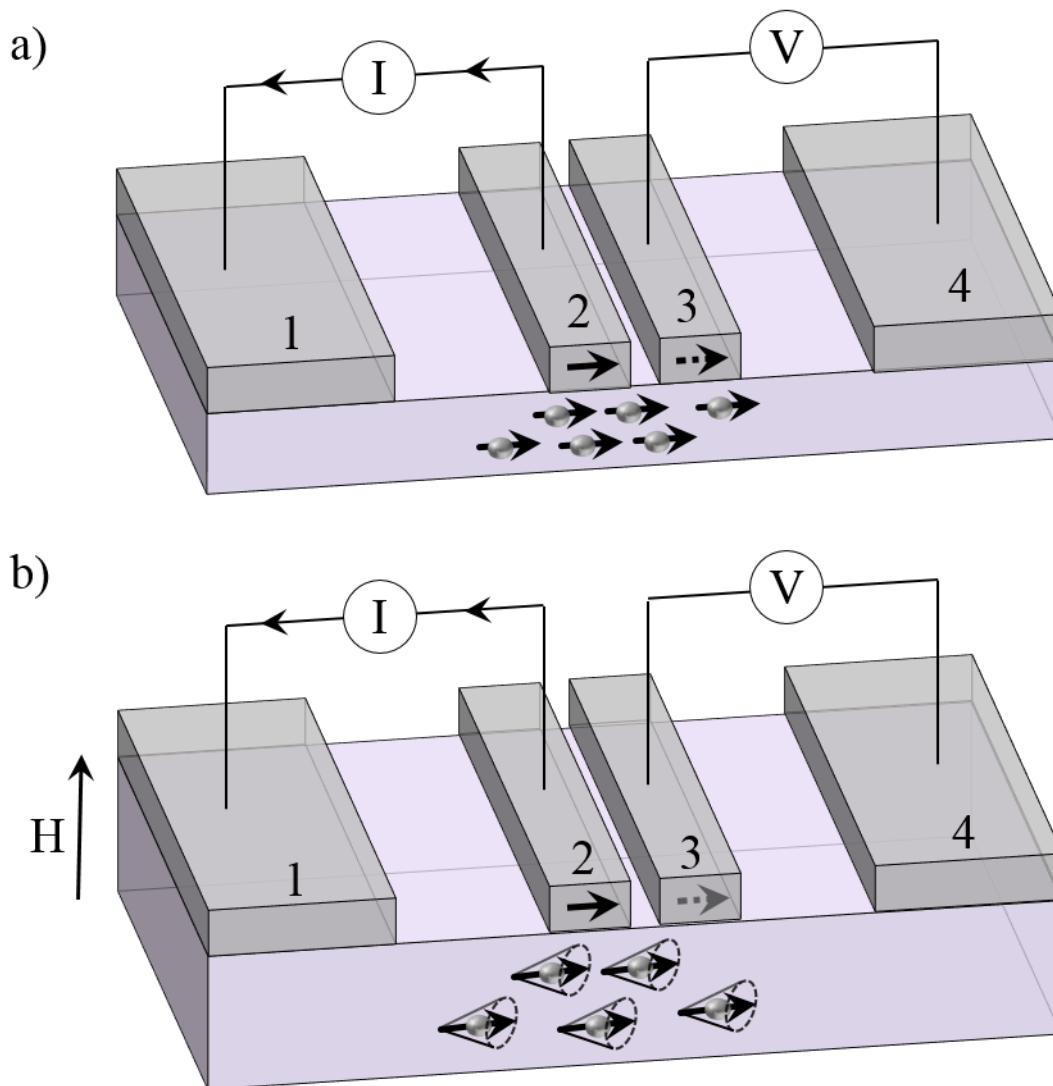


**Figure 2.8 The four-terminal Hanle effect.** Schematic showing the two states of a 4T Hanle device, for a) no external magnetic field and b) an external magnetic field applied out-of-plane. For no external field, the spins are injected, transport through the channel (purple), and are measured beneath contact 3 by measuring the voltage difference between contacts 3 and 4 (the two right most contacts respectively). When a magnetic field is applied, shown in Figure 2.8b, the spins begin to precess. If the magnetic field is strong enough, the precession cause the spins to randomize before they reach contact 3, and no voltage will be readable between contacts 3 and 4. For a mid-strength magnetic field, some of the spins will reach contact 3, so a diminished voltage signal will be read.

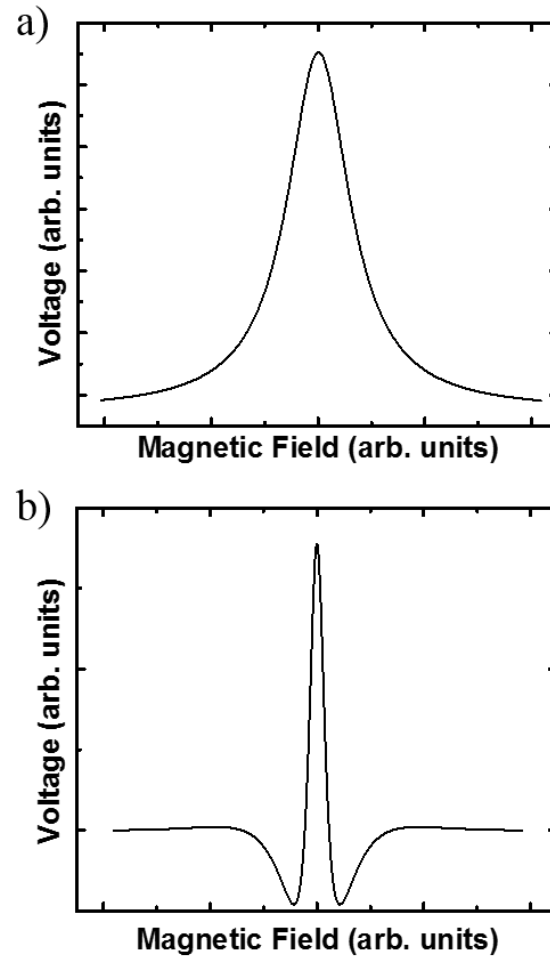


**Figure 2.9 The Hanle curve: Two cases.** Graphs showing the two possible Hanle curve shapes for a) a short- $d$  channel length, and b) a long- $d$  channel length. In this case,  $d$  corresponds to the separation between contacts 2 and 3 in Figure 2.8.

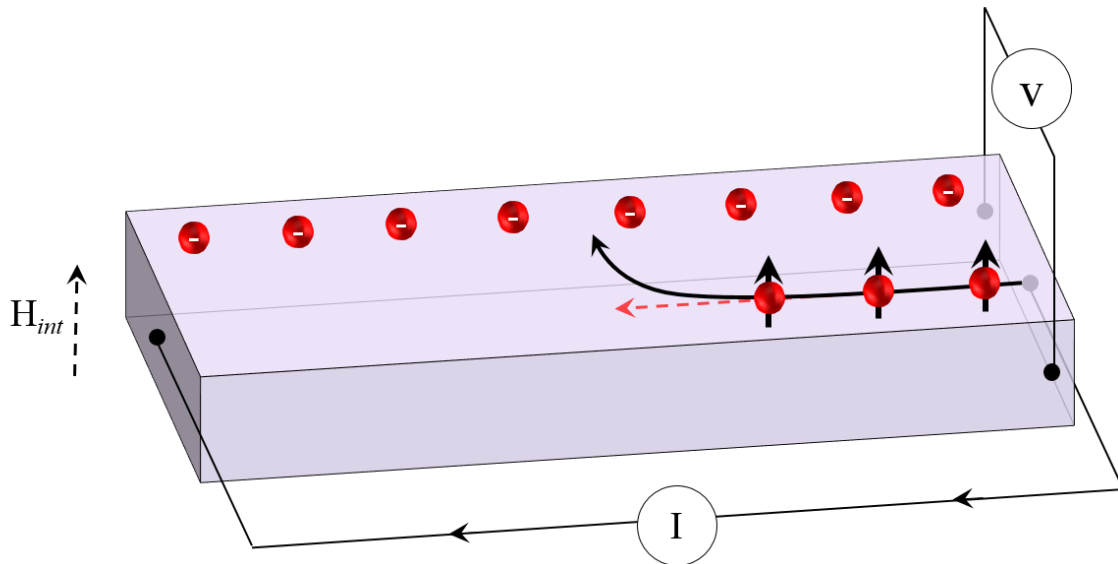


**Figure 2.10 The inverse spin Hall effect.** Device schematic showing the generation of charge current in response to spin current, the inverse spin Hall effect. For an electrically injected, spin-polarized charge current, the effective coupling of spin and orbital angular momenta will cause the electrons to be deflected due to their interaction with an internal magnetic field (which results from the orbital motion of electrons in the system), creating an effective Lorentzian force similar to that seen in the Hall effect (Figure 2.5). This effect will lead to a measurable voltage across the front and back (as indicated) of the sample.

## CHAPTER 3

### DILUTE MAGNETIC DIELECTRIC MATERIALS FOR SPIN INJECTION<sup>2</sup>

Herewith we have reported the magnetic properties of phase-separated Co-doped CeO<sub>2</sub> films (with a Ce:Co atomic-ratio of 0.97:0.03) grown on single-crystal SrTiO<sub>3</sub> (001) substrates. A comparison of the magnetic characteristics of these films with those of homogeneously doped CeO<sub>2</sub>:Co films of the same composition illustrates the significant differences in their magnetic behavior. These behavioral characteristics provide a model for determining if the magnetic behavior observed in this, as well as in other diluted magnetic dielectric systems, is due to homogeneous doping, a mixture of doping and transition metal cluster formation, or exists purely as a result of transition metal clustering. This work further illustrates the potential for homogeneously doped DMDs as tunnel barriers for spin-filtered injection.

---

<sup>2</sup> This chapter is based on the paper entitled: “Magnetic Characteristics of Phase Separated CeO<sub>2</sub>:Co Thin Films” M. C. Prestgard, G. Siegel, Q. Ma, and A. Tiwari, Appl. Phys. Lett. (2013) 103, 102409. © Copyright 2013, AIP Publishing LLC. Reprinted with permission.

### 3.1 Introduction

The miniaturization of devices is the main driving force for the development of the electronics industry and occurs with predictable regularity in accordance with Moore's law.<sup>1,2</sup> This miniaturization, however, is approaching a limit – one defined by the fact that the efficiency of current devices is physically constrained by material properties at such sizes. In order to overcome this hurdle, alternative facets of technological improvement other than miniaturization must be considered. One such area is spintronics, which allows the utilization of an electron's spin in addition to its charge.<sup>3-</sup>

6

Spintronic devices can be classified in two groups, active devices and passive devices. Though passive spintronics have been quite successful in their various applications, such as magnetic read-heads, magnetic RAM and so on, active spintronic devices are essential for this technology to advance further.<sup>3,4</sup> Realization of active spintronics requires the injection and manipulation of electrons' spins in semiconductors. Initial spin injection attempts showed serious limitations in efficiency, as material mismatches existed between the metallic ferromagnet used to inject the electrons and the semiconductor used as the base of the device.<sup>7,8</sup> Diluted magnetic semiconductors (DMS) have likewise been attempted for spin injection, however, overall low Curie temperatures have once again resulted in limited success.<sup>9,10</sup> Another potential route for injecting spin-polarized carriers into semiconductors is by using ferromagnetic tunnel barriers, which can act as a spin filter and allow only one kind of spin to tunnel into the semiconductor.<sup>11-15</sup> The feasibility of spin-dependent tunneling has been demonstrated using europium chalcogenides (EuX, X: O, S, Se).<sup>16,17</sup> However, europium chalcogenides



exhibit a  $T_c$  that is much lower than room temperature, making them useless for practical device applications. In order to be useful in real applications, the spin filter material needs to be ferromagnetic at room temperature.

Recent reports of the observation of room-temperature ferromagnetism (RTF) in dilute magnetically doped dielectrics (DMD) have created a lot of excitement in the field.<sup>18-20</sup> Cobalt-doped  $\text{CeO}_2$  is one of the most widely studied members of this family. It has been shown that when a small amount ( $\sim 3$  atomic %) of cobalt replaces Ce in  $\text{CeO}_2$ , the material exhibits RTF. Although the above reports have generated a lot of enthusiasm among spintronic researchers, they also raised some doubts about whether the observed behavior is an intrinsic property of the material or due to some kind of precipitates. To clarify this aspect, more studies utilizing state-of-the-art techniques of elemental determination are needed. In this paper we are reporting the growth, characterization, and magnetic properties of phase-separated cobalt-doped  $\text{CeO}_2$  films in order to better understand the behavioral differences between this and the homogeneously doped  $\text{CeO}_2$  films.

### 3.2 Experimental Procedure

The phase-separated  $\text{CeO}_2\text{:Co}$  films (with a Ce : Co atomic-ratio of 0.97 : 0.03) were prepared using a pulsed laser deposition (PLD) system. A traditional sol-gel technique was used to prepare  $\text{CeO}_2\text{:Co}$  powder. This was followed by subsequent sintering and iso-static pressing to generate a highly dense ceramic pellet for laser ablation. A Lambda Physik Compex Pro KrF excimer laser ( $\lambda = 248$  nm and pulse width of 25 ns) was used to ablate the dense ceramic target at a pulse repetition rate of 10 Hz.

The deposition was performed under an oxygen-deficient environment (base vacuum of  $10^{-5}$  mbar) to deliberately induce cobalt precipitation in the system. The ablated material was deposited on single-crystal STO (001), which was heated to 650°C during the deposition. The deposition rate, as determined using a P-10 Tencor profilometer, was found to be approximately 0.47 Å/shot, thus 11,000 laser pulses resulted in a film of thickness of approximately 520 nm.

A Philips X'Pert X-ray Diffractometer (Cu  $K\alpha$  radiation) was used for X-ray diffraction (XRD) measurements. X-ray photoelectron spectroscopy (XPS) was performed using a Kratos Axis Ultra DLD. A Quantum Design superconducting quantum interference device (SQUID) was used to perform magnetic property measurements at temperatures between 10 K and 350 K. Synchrotron X-ray absorption spectroscopy (XAS) measurements were performed at the 5BM-D beamline of the DND-CAT at Sector 5 of the Advanced Photon Source (Argonne, IL). The Co K edge XAS measurements of the film samples were carried out in fluorescence mode by collecting the Co  $K\alpha$  emission intensity using a 4-element Si-drift solid-state detector (SII NanoTechnology). The film sample was mounted vertically on a spinner with its normal surface bisecting the 90° angle between the X-ray incidence and photon detecting directions. The film sample spins during data collection to minimize Bragg diffraction from the substrate. A double crystal Si (111) monochromator was used for energy selection. The incident X-ray intensity was detuned by 65% for harmonic rejection. Bulk reference data were collected in transmission mode on metal Co foil and powder CoO and Co<sub>2</sub>O<sub>3</sub>. Fine CoO and Co<sub>2</sub>O<sub>3</sub> powders were uniformly spread on long pieces of Scotch tape (3M Corp), which were then folded to produce adequate absorption. The

Athena and Artemis software packages were used for XAS data analyses.

### 3.3 Results and Discussion

Figure 3.1 shows the XRD pattern for a  $\text{CeO}_2\text{:Co}$  thin film along with that for a pure STO substrate. Only the peaks corresponding to the (200) and (400) orientations of the parent  $\text{CeO}_2$  could be observed, indicating C-axis-oriented growth. This result is consistent with the growth mechanism previously reported for  $\text{CeO}_2$ -based systems.<sup>18,21</sup> The presence of cobalt could not be definitively determined by XRD, as the amount of doping was very small and, moreover, the anticipated cobalt peaks overlap the STO peaks, specifically those near  $41.7^\circ$  and  $47.6^\circ$ . In order to evaluate the state of cobalt in the film, further characterization was performed using an XAS technique.

Figure 3.2 shows XAS results for  $\text{CeO}_2\text{:Co}$  thin films. The experimentally observed XAS spectra are shown in Figure 3.2a, while Figure 3.2b and 3.2c show the k-space and the R-space Fourier transformation, respectively. We have also shown the data collected for Co metal,  $\text{Co}_2\text{O}_3$ , and CoO in the above figures. These standards were all used in a linear combination fit (LCF) model, using Athena.<sup>22</sup> The LCF modeled the Co K-edge data from the doped sample as a combination of pure cobalt and cobalt of varying oxidation states (pure cobalt –  $\text{Co}^0$ , CoO –  $\text{Co}^{2+}$ , and  $\text{Co}_2\text{O}_3$  –  $\text{Co}^{3+}$ ). The best fit of these three models indicated that, of the 3% cobalt dopant, 85.7% ( $\pm 0.7\%$ ) was in metallic precipitate form, 12.6% ( $\pm 0.9\%$ ) was in  $\text{Co}^{3+}$  form, and 1.7% ( $\pm 0.5\%$ ) was in  $\text{Co}^{2+}$ .

XAS studies were supplemented by the X-ray photoelectron spectroscopy (XPS). Figure 3.3 shows the  $2p_{3/2}$  spectra of cobalt recorded from a  $\text{CeO}_2\text{:Co}$  film. Deconvolution of this spectrum showed the presence of two sets of peaks, one at 778.3 eV

and the other centered at around 780.4 eV. The peak at 778.3 corresponds to metallic Co while the peak around 780.4 eV corresponds to a mixture of  $\text{Co}^{2+}$  and  $\text{Co}^{3+}$ .<sup>23,24</sup> Quantitative analysis of the XPS data showed that about 85% ( $\pm 1\%$ ) of the cobalt exists as clusters, and the remaining 15% ( $\pm 1\%$ ) is a mixture of the 2+ and 3+ valence states.

In Figures 3.4a-3.4e, we have shown the magnetization versus field (M versus H) data for the  $\text{CeO}_2\text{:Co}$  films at different temperatures over the range of 10 K to 300 K. The M versus H data show clearly visible hysteretic behavior at 10 K. A coercive field of  $\sim 850$  Oe was observed at this temperature. The coercivity of the films dropped as the temperature was increased and almost vanished at 300 K. However, the M versus H data still exhibited a saturation effect. Figure 3.4f shows the field-cooled (FC) and zero-field-cooled (ZFC) magnetization versus temperature (M versus T) data. The ZFC/FC M versus T data show bifurcation at about 250 K. The observed behavior is a characteristic of a superparamagnetic system. A material exhibits superparamagnetism when it is comprised of nanoscale magnetic clusters embedded in a nonmagnetic matrix.<sup>25</sup> So the magnetic results are consistent with the conclusions of XAS and XPS, which unambiguously indicated the presence of magnetic clusters. An estimate of the size of superparamagnetic clusters was made using the relation:<sup>25</sup>  $KV = 25k_B T_B$ , where K is the bulk anisotropy energy, V is the volume of the magnetic cluster,  $k_B$  is the Boltzmann's constant, and  $T_B$  is the blocking temperature where ZFC and FC shows bifurcation. Using the anisotropy energy (K) of  $\text{Co}^{26}$  as  $4 \times 10^6$  erg/cm<sup>3</sup> and the experimentally determined value of  $T_B$  as 250 K, the approximate diameters of the precipitates, assuming they are spherical in nature, was found to be  $\sim 7.4$  nanometers.

Quantitative analysis of the data revealed that the magnetic response of the system

is much more complex than expected from a simple system comprised of magnetic clusters embedded in a nonmagnetic matrix. Specifically, the observed saturation magnetization of the films is significantly higher than that expected for metallic cobalt. The films showed a saturation magnetization of  $2.4 \mu_B/\text{Co}$  at 10 K, which is 41% higher than the value expected for metallic cobalt ( $1.7 \mu_B/\text{Co}$ ).<sup>27</sup> This indicates that apart from forming clusters, some cobalt is also substituting for Ce in the  $\text{CeO}_2$  matrix. Furthermore, our results indicated that the cobalt ions which substitute Ce in the  $\text{CeO}_2$  matrix result in much higher magnetization as compared to the cobalt clusters.

In order to understand the above aspect, we will have to revisit the earlier work reported for homogeneously doped  $\text{CeO}_2:\text{Co}$  system.<sup>18</sup> Specifically, in the above report, it was found that in the homogeneously doped  $\text{CeO}_2:\text{Co}$  system, the orbital angular momentum of the Co remains unquenched. Because of this, the orbital angular momentum and spin angular momentum add up, giving rise to a net angular momentum,  $J = L + S = 4$ , which results in a spontaneous magnetic moment of  $M \sim 6.7 \mu_B$  per cobalt ion [ $M = g\mu_B\sqrt{J(J+1)}$ ;  $g=3/2$ ,  $J=4$ ].<sup>18,28</sup> By assigning a moment of  $1.7 \mu_B/\text{Co}$  to metallic cobalt precipitates and a moment of  $6.7 \mu_B/\text{Co}$  to cobalt ions substituting Ce in  $\text{CeO}_2$  matrix, we estimated a net magnetization of  $2.45 \mu_B/\text{Co}$  ( $\pm 0.05$ ) for the phase separated  $\text{CeO}_2:\text{Co}$  films based on the XPS and XAS results. This estimated value matches very well with the experimentally determined value of  $2.4 \mu_B/\text{Co}$ .

### 3.4 Conclusion

In summary, we have shown that when  $\text{CeO}_2:\text{Co}$  films are deposited under low oxygen pressure using a PLD system, it results in a phase-separated system, as shown by

XAS and XPS. These techniques revealed that in this phase-separated system, approximately 85% of the cobalt exists as clusters, while the rest substitutes into the  $\text{CeO}_2$  lattice. Phase-separated  $\text{CeO}_2\text{:Co}$  shows very unusual magnetic properties, which are very different from homogeneously doped films as well as from a conventional superparamagnetic system. This variation in the anticipated behavior is due to there being two distinct contributions to magnetic moment: first, from the cobalt clusters present, and secondly due to the substitution of cobalt for cerium in the lattice. Detailed quantitative analysis of our results showed that the 60% of the total moment of the film originates from the 85% of the cobalt atoms that precipitate as metallic clusters while the remaining 40% of the total moment comes from just 15% of the cobalt that enters substitutionally in the  $\text{CeO}_2$  matrix.

### 3.5 References

1. Brock, D. C.; Moore, G. E. *Understanding Moore's Law: Four Decades of Innovation*; Chemical Heritage Foundation: Philadelphia, 2006; pg. 25-26.
2. Percy, P. S. *Nature* **2000**, *406*, 1023(1)-(6).
3. Wolf, S. A.; Awschalom, D. D.; Buhrman, R. A.; Daughton, J. M.; von Molnár, S.; Roukes, M. L.; Chtchelkanova, A. Y.; Treger, D. M. *Science* **2001**, *294*, 1488-1495.
4. Prinz, G. A. *Science* **1998**, *282*, 1660-1663.
5. Park, W. K.; Ortega-Hertogs, R. J.; Moodera, J. S.; Punnoose, A.; Seehra, M.S. *J. Appl. Phys.* **2002**, *91*, 8093-8095.
6. Pearton, S. J.; et al. *J. Phys.: Condens. Matter* **2004**, *16*, R209-R245.
7. Datta, S.; Das, B. *Appl. Phys. Lett.* **1990**, *56*, 665-667.
8. Das Sarma, S.; Fabian, J.; Hu, X.; Zutic, I. *IEEE. Trans. Magnet.* **2000**, *36*, 2821-2826.
9. Yuan-Qiang, S.; Huai-Wu, Z.; Qi-Ye, W.; Yuan-Xun, L.; Xiao, J. Q. *Chinese Phys. Lett.* **2007**, *24*, 218-221.
10. Fukumura, T.; Yamada, Y.; Toyosaki, H.; Hasegawa, T.; Koinuma, H.; Kawasaki, M. *Appl. Surf. Sci.* **2004**, *223*, 62-67.
11. Hao, X.; Moodera, J. S.; Meservey, R.; *Phys. Rev. B* **1990**, *42*, 8235-8243.
12. Shvets, I. V.; Grigorenko, A. N.; Novoselov, K. S.; Mapps, D. J.; *Appl. Phys. Lett.* **2005**, *86*, 212501(1)-(3).
13. Tsymbal, E. Y.; Mryasov, O. N.; LeClair, P. R.; *J. Phys: Condes. Matter* **2003**, *15*, R109-R142.
14. Fiederling, R.; Keim, M.; Reuscher, G.; Ossau, W.; Schmidt, G.; Waag, A.; Molenkamp, L.W. *Nature* **1999**, *402*, 787-790.
15. Simmons, J. G.; *J. Appl. Phys.* **1963**, *34*, 2581-2590.
16. Miao, G.-X.; Muller, M.; Moodera, J. S.; *Phys. Rev. Lett.* **2009**, *102*, 076601(1)-(4).
17. Schmehl, A.; Vaithyanathan, V.; Hermberger, A.; *Nature Materials* **2007**, *6*, 882-888.

18. Tiwari, A.; Bhosle, V. M.; Ramachandran, S.; Sudhakar, N.; Narayan, J.; Budak, S.; Gupta, A.; *Appl. Phys. Lett.* **2006**, 88, 142511(1)-(3).
19. Slusser, P.; Kumar, D.; Tiwari, A. *JOM* **2011**, 63, 25-28.
20. Kumar, S.; Kim, Y. J.; Koo, B.H.; Choi, H.; Lee, C. G. *IEEE Trans. Magnet.* **2009**, 45, 2439-2441.
21. Kang, J. F.; Gong, G. C.; Lian, G. J.; Wang, Y. Y.; Han, R. Q. *Solid State Commun.* **1998**, 108, 225-227.
22. Gautam, S.; Kumar, S.; Thakur, P.; Chae, K. H.; Kumar, R.; Koo, B. H.; Lee, C. G. *J. Phys. D: Appl. Phys.* **2009**, 42, 175406(1)-(7).
23. Moulder, J. F.; Stickle, W. F.; Sobol, P. E.; Bomben, K.D. *Handbook of X-ray Photoelectron Spectroscopy*; Perkin-Elmer: Eden Prairie 1992.
24. Biesinger, M. C.; Payne, B. P.; Grosvenor, A. P.; Lau, L. W. M.; Gerson, A. R.; Smart, R. St.C. *Appl. Surf. Sci.* **2011**, 257, 2717-2730.
25. Bean C. P.; Livingston, J. D.; *J. Appl. Phys.* **1959**, 30, 120S-129S.
26. Gray, N. W.; Tiwari, A. *J. Appl. Phys.* **2011**, 110, 033903(1)-(7).
27. Murthy, V. S. R.; Jena, A. K.; Gupta, K. P.; Murty, G. S. *Structure and Properties of Engineering Materials*; Tata McGraw-Hill Education: New Delhi, 2003.
28. Ashcroft, N. W.; Mermin, N. D. *Solid State Physics*; Harcourt College Publishers: Fort Worth, 1975.



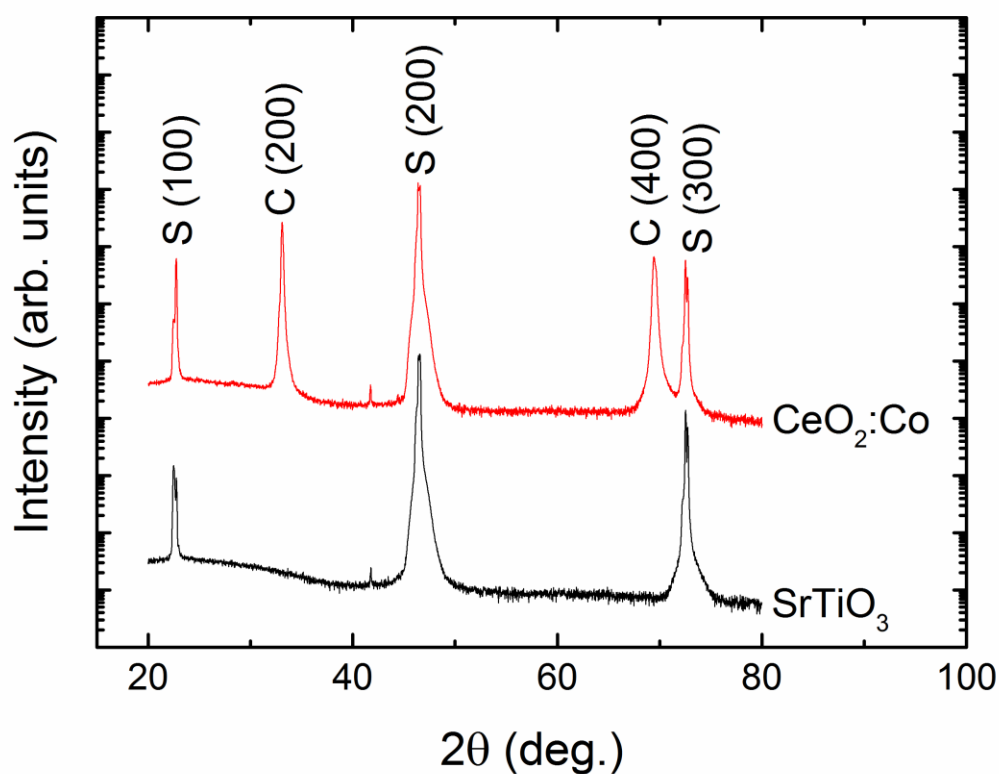


**Figure 3.1 X-ray diffraction patterns for  $\text{CeO}_2\text{:Co}$  thin films and the STO substrate.** XRD data for the  $\text{CeO}_2\text{:Co}/\text{STO}$  thin films (red) versus that of a pure STO substrate. On these diffraction patterns, the S peaks correspond to substrate, whereas the C peaks correspond to  $\text{CeO}_2$ . As can be seen, the film growth is highly oriented and no cobalt peaks could be detected.

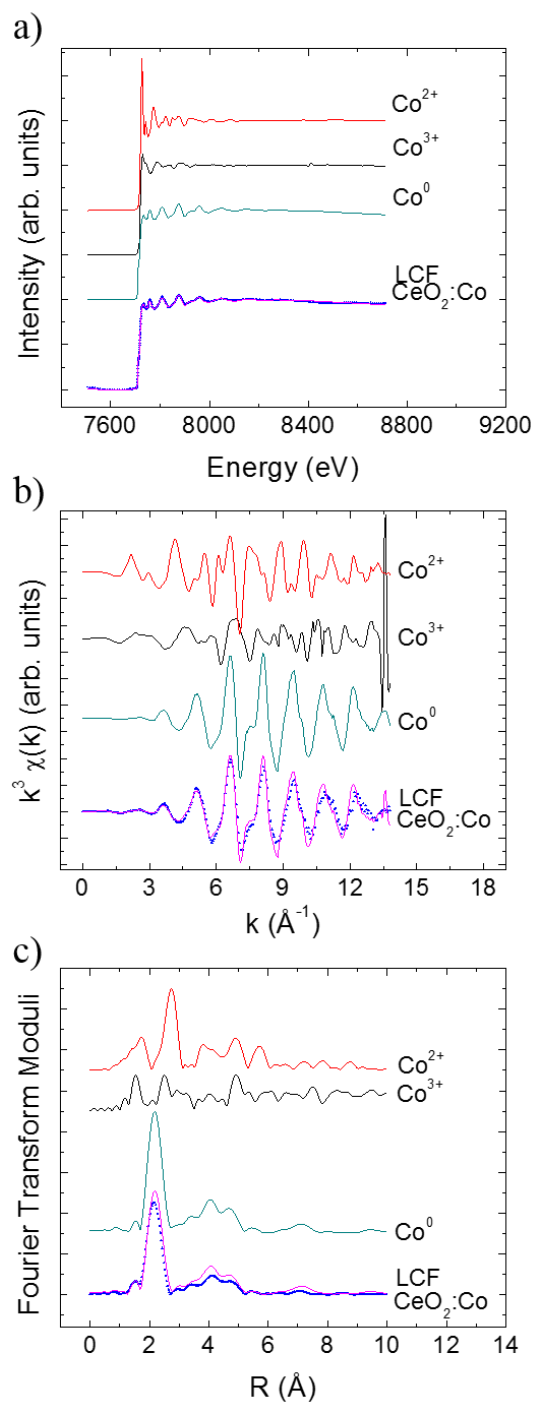


**Figure 3.2  $\text{CeO}_2:\text{Co}$  X-ray absorption spectra.** (a) X-ray absorption spectroscopy data for the Co K-edge of  $\text{CeO}_2:\text{Co}$  film deposited on STO (blue curve). Also shown is a fit to the linear combination fit (LCF) model (purple curve), along with the standard data for  $\text{CoO}$  (red),  $\text{Co}_2\text{O}_3$  (black), and  $\text{Co}$  metal (green), (b) K-space (wavenumber) and (c) R-space (real space) Fourier transform for the above data.

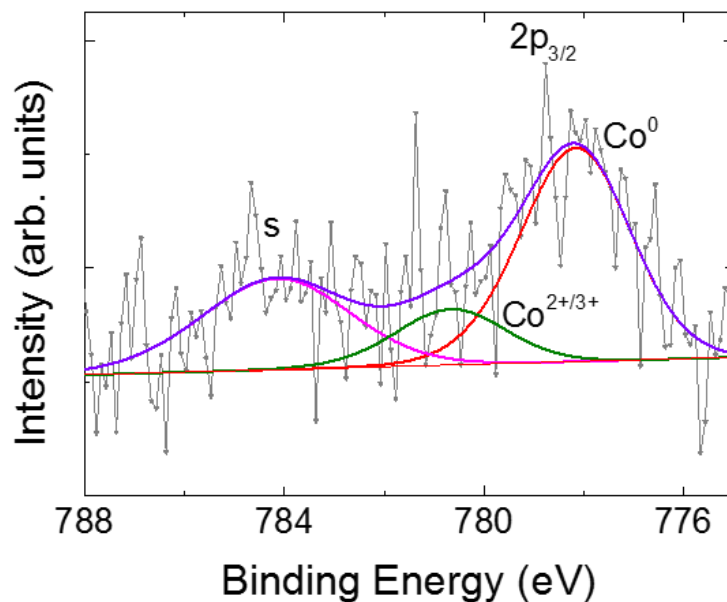


**Figure 3.3 X-ray photoelectron spectroscopy data for CeO<sub>2</sub>:Co thin films.** In this spectrum, the leftmost peak indicates a satellite peak, the peak at about 780.4 eV corresponds to 2p<sub>3/2</sub> peak of the Co<sup>2+</sup>/Co<sup>3+</sup>, and the peak at 778.3 eV corresponds to 2p<sub>3/2</sub> peak of the metallic cobalt. These fits were used to approximate the ratio of oxidized to metallic cobalt.

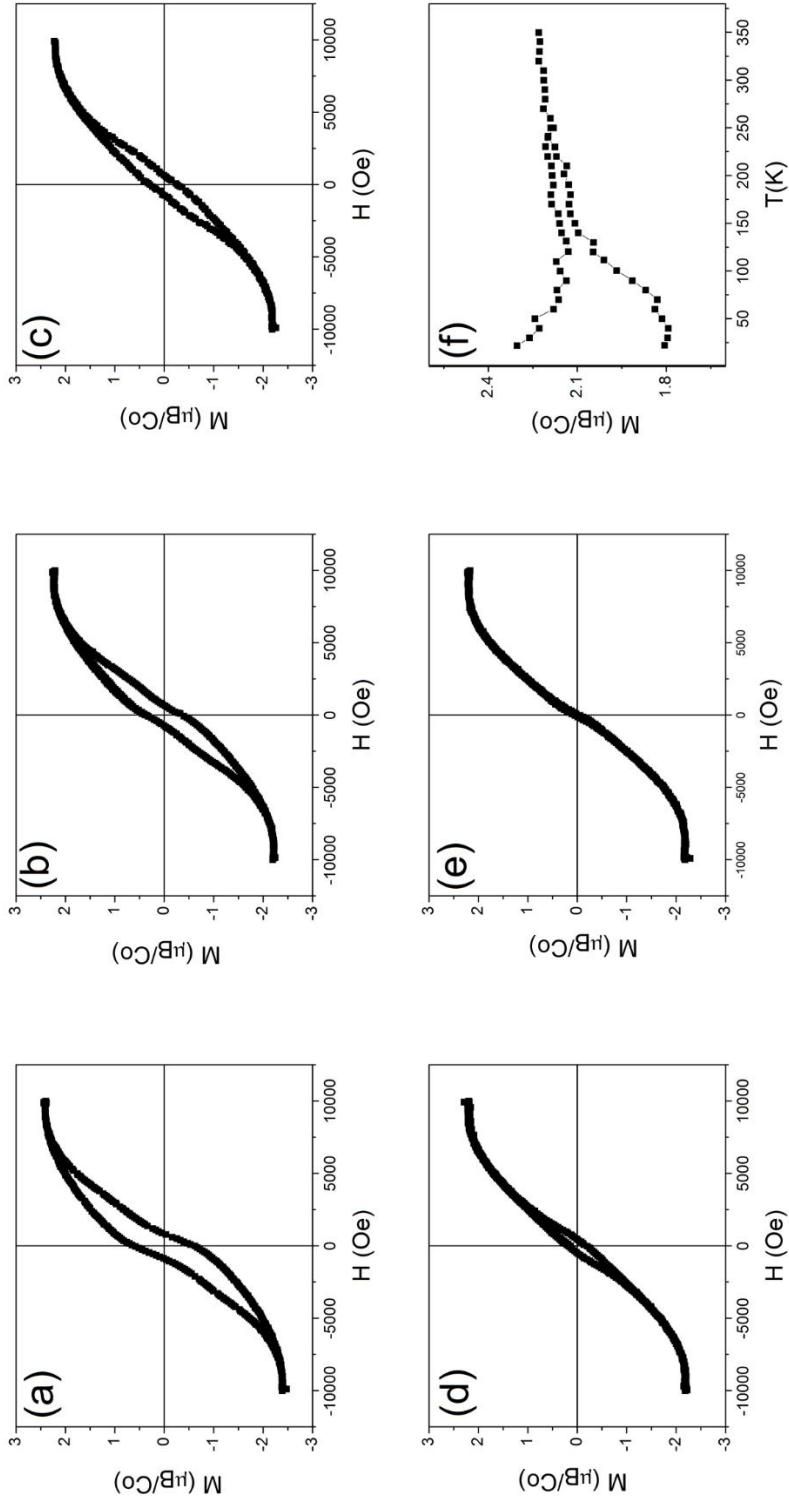


**Figure 3.4 M versus H data for the phase-separated  $\text{CeO}_2:\text{Co}$  thin films.** M versus. H curves at (a) 10 K, (b) 50 K, (c) 100 K, (d) 200 K, and (e) 300 K. The figure (f) shows the zero-field cooled (ZFC) and field cooled (FC) M versus T data for the same film measured at  $H = 6,000$  Oe.

## CHAPTER 4

### SPIN TRANSPORT IN ZINC OXIDE THIN FILMS AS OBSERVED USING NONLOCAL HANLE MEASUREMENTS<sup>3</sup>

Zinc oxide is considered a potential candidate for fabricating next-generation transparent spintronic devices. However, before this can be achieved, a thorough scientific understanding of the various spin transport and relaxation processes undergone in this material is essential. Herewith, we have reported our investigations into these processes via temperature-dependent Hanle experiments. ZnO thin films were deposited on C-axis sapphire substrates using a pulsed laser deposition technique. Careful structural, optical, and electrical characterizations of the films were performed. Temperature-dependent nonlocal Hanle measurements were carried out using an all-electrical scheme for spin injection and detection over the temperature range of 20 – 300 K. From the Hanle data, spin relaxation time in the films was determined at different temperatures. A detailed analysis of the data showed that the temperature dependence of spin relaxation time follows the linear-in-momentum Dyakonov-Perel mechanism.

---

<sup>3</sup> This chapter is based on the paper entitled: “Temperature dependence of the spin relaxation in highly degenerate ZnO thin films” M. C. Prestgard, G. Siegel, R. Roundy, M. Raikh, and A. Tiwari, J. Appl. Phys. (2015) 117, 083905. © Copyright 2015, AIP Publishing LLC. Reprinted with permission.

#### 4.1 Introduction

In current semiconductor device research, there is a strong emphasis on developing spintronic devices. These are devices that will be capable of utilizing the spin of an electron in place of, or in addition to, its charge, whereas present electronic devices only use the electron's charge.<sup>1</sup> Spintronic devices are also considered essential to compensate for the impending, size-limited failure of Moore's law, as current electronics capabilities will no longer be able to meet future consumer product demands. The field of semiconductor spintronics, despite its evident potential, requires a thorough understanding of spin transport and relaxation processes in semiconducting materials before such devices are ready for practical applications.<sup>2,3</sup>

Recently, there has also been a lot of interest in realizing transparent spintronic devices. Zinc oxide (ZnO) is considered an ideal material for such applications.<sup>4-6</sup> It is a transparent semiconductor with a large bandgap of 3.4 eV and a high room-temperature exciton binding energy of 60 meV. A fairly large spin Hall angle of  $\sim 1\%$  has also been recently observed in ZnO thin films.<sup>7</sup> The above observation is quite intriguing because, in ZnO, the valence-band splitting is very small ( $\sim 3.5$  meV), so in principle the spin-orbit coupling (SOC) in the material should also be small.<sup>8</sup> For example, if we compare the valence-band splitting of ZnO with the splitting of GaAs, the former is almost 2 orders of magnitude smaller than the latter.<sup>9</sup> This difference in splitting is generally considered to be proportional to the SOC, so there should be weaker SOC (and hence much longer spin relaxation times) in ZnO as compared to GaAs. However, recent experiments have shown that this is not the case and imply that our understanding of the various spin relaxation and transport processes in ZnO is far from complete.<sup>10</sup>

Here we report our investigations into the mechanisms of spin transport and relaxation in highly degenerate ZnO thin films. All-electrical, four-probe Hanle devices were fabricated to experimentally determine the spin relaxation rate in ZnO films. Based on the analysis of the temperature dependence of the spin lifetime, with values ranging between  $\sim 140$  ps at 300 K and  $\sim 153$  ps at 20 K, we attributed the dominant mechanism of the spin relaxation to the linear-in-momentum ( $k$ ) Dyakonov-Perel (DP) mechanism. This mechanism is specific to the wurtzite crystal structure of ZnO, in which a hexagonal C-axis reflection asymmetry is present.<sup>11</sup> A strong degeneracy of electrons in the samples was found to make the temperature dependence of spin relaxation time very weak.

#### 4.2 Experimental Procedure

Thin films of ZnO were deposited on C-axis-aligned sapphire substrates using a pulsed laser deposition (PLD) technique. For this, a highly dense ceramic target of ZnO was ablated using a pulsed laser (Lambda Physik COMPex Pro KrF Excimer Laser,  $\lambda = 248$  nm, pulse width = 25 ns) for 8,000 pulses at a repetition rate of 10 Hz. Depositions were performed under an oxygen pressure of  $10^{-4}$  Torr and substrate temperature of 700 °C. Ablation by 8,000 pulses gave approximately 200 nm thick films. The ZnO films thus prepared were characterized using X-ray diffraction, UV-Vis transmittance spectroscopy, temperature-dependent (measurements were conducted at 1  $\mu$ A over the temperature range of 20 - 300 K) four-point probe electrical conductivity measurements, Hall effect measurements, and nonlocal Hanle measurements. For making the nonlocal Hanle test device, a thin tunnel barrier layer of MgO ( $\sim 3$ -5 nm) was first deposited on the top of the ZnO film using PLD and then a NiFe layer ( $\sim 10$  nm) was deposited in a three-probe

pattern using photolithography and e-beam evaporation techniques (see Figure 4.1a). For depositing the NiFe contacts, positive photoresist was applied and patterned in the 3T arrangement (4.1a), and using e-beam evaporation, the NiFe contacts were deposited over the entire sample. The photoresist was then removed using acetone, as was the NiFe deposited on the photoresist, therefore leaving the desired NiFe 3T structure. The center NiFe probe was then cut using a focused ion beam (FIB, dual-beam FEI Helios Nanolab 600) to yield two contacts separated by a  $\sim 60$  nm gap, thereby giving the desired four-probe structure (Figure 4.1b). For nonlocal Hanle measurements, the probes were first magnetized by applying an in-plane magnetic field. Then a current ( $\pm 1$  mA) was passed from contact 1 to contact 2 and the voltage generated between contacts 3 and 4 was measured in the presence of a transverse magnetic field which was swept from -4 kG to 4 kG.

### 4.3 Results and Discussion

The XRD results obtained using Cu  $K_\alpha$  radiation are shown in Figure 4.2a. Only the peaks corresponding to the (0002) and (0004) planes of ZnO and the (0006) plane of the sapphire substrate were observed, indicating the highly C-axis-aligned nature of the films. Figure 4.2b shows the UV-Vis transmission spectroscopy results. These results clearly show that the ZnO thin films were transparent. The inset of Figure 4.2b shows the plot of absorption coefficient squared,  $\alpha^2$ , versus energy  $h\nu$ . A linear relationship indicates the direct nature of the film's bandgap.<sup>12</sup> In Figure 4.2c, the electrical conductivity ( $\sigma$ ) versus temperature data are shown. An increase in the electrical conductivity upon increasing the temperature confirmed the semiconducting behavior of



the films.

The Hall effect measurements were performed to calculate carrier concentration ( $n$ ), mobility ( $\mu$ ), and diffusion coefficient ( $D$ ). The carrier concentration at room temperature was  $n = 3.45 \times 10^{19} \text{ cm}^{-3}$  and decreased slightly with a decrease in temperature (see Figure 4.2d). From the carrier concentration, we calculated the room temperature Fermi energy as 115.9 meV (Fermi temperature,  $T_F \sim 1345 \text{ K}$ ) using the relation:

$$\mathcal{E}_F = \frac{\hbar^2}{2m^*} (3\pi^2 n)^{2/3} \quad (4.1)$$

In the above calculation we used the effective mass of electron,  $m^* = 0.3m_0$ , for ZnO.<sup>13</sup> Further discussion on calculation of the Fermi energy is given in Appendix A. High values of the carrier concentration and Fermi energy indicated the highly degenerate nature of the ZnO films. From the electrical conductivity and carrier concentration data, mobility values were determined using the relation:  $\mu = \sigma / en$ . The  $\mu$  versus  $T$  data are shown in Figure 4.2e. Using the mobility data, diffusion coefficient ( $D$ ) was calculated using the Einstein relation for the degenerate systems<sup>14</sup>:

$$D = \frac{\mu(T)k_B T}{e} \frac{F_{1/2}(\frac{\mathcal{E}_F}{k_B T})}{F_{-1/2}(\frac{\mathcal{E}_F}{k_B T})} \quad (4.2)$$

where  $F_j(x)$  is the Fermi-Dirac integral defined as,

$$F_j(x) = \frac{1}{j!} \int_0^\infty dt \frac{t^j}{e^{(t-x)} + 1} \quad (4.3)$$

At room temperature, a value of  $D \approx 3.2 \times 10^{-4} \text{ m}^2/\text{s}$  was obtained. The calculated values of  $D$  as a function of temperature are shown in Figure 4.2f (red curve).

For comparison we have also shown the  $D$  versus  $T$  data calculated using the Einstein relation for the nondegenerate case (black curve):

$$D = \frac{\mu(T) \cdot k_B T}{e} \quad (4.4)$$

The above equation is based on the exponential approximation where the Fermi distribution becomes Boltzmann-like. As can clearly be seen in Figure 4.2f, the highly degenerate nature of the films, as evidenced by the position of the Fermi energy and the relatively high carrier concentration compared to the conduction band effective density of states for ZnO ( $N_C \approx 4.1 \times 10^{18} \text{ cm}^{-3}$  and  $n \approx 3.5 \times 10^{19} \text{ cm}^{-3}$  at 300 K), strongly affects the values of the diffusion coefficient and its variation with temperature. In the case of a degenerate system (such as the films studied in the present paper), a much weaker temperature dependence of  $D$  is expected compared to a nondegenerate system. As will be shown later, the weak temperature dependence of  $D$  makes the temperature dependence of spin relaxation time weak also.

Most of the Hanle measurements reported in literature were performed using three-probe test structures, due to the ease of fabrication of these structures.<sup>15,16</sup> However, in traditional three-probe Hanle measurements, spin injection and detection is done using the same contact. Thus these measurements produce a convoluted signal which is the sum of two voltages, the voltage due to spin accumulation in the semiconductor channel and the voltage drop across the contact resistance. In contrast, in four-probe structures, any signal measured is a direct measure of spin transport occurring within the device, as spin accumulation is directly probed, and can be differentiated from the baseline voltage by investigating the dependence on external magnetic field.<sup>17,18</sup> Therefore, we used four-probe structures for performing Hanle measurements in this study.

Hanle measurements were performed at temperatures ranging from 20 – 300 K according to the schematic shown in Figure 4.1c. By passing a drift current between contacts 1 and 2, the spin-polarized electrons are injected at contact 2. Electrons accumulate near the second contact, and then diffuse towards the third contact. This gives a net spin accumulation at the third contact as well. The voltage measured between contacts 3 and 4 is a direct measure of the spin accumulation below contact 3. An out-of-plane transverse magnetic field was applied to record the Hanle curves. Figures 4.3a and 4.3b show the normalized Hanle signal at 300, 200, 100, 50, and 20 K for negative (4.3a) and positive (4.3b) applied current, all of which showed similar behavior.

A general theoretical expression for describing the shape of the Hanle voltage curve is given by the following equation<sup>19, 20</sup>:

$$V_s(B) = \frac{A\sqrt{D\tau}}{\sigma(T)} \cdot \exp\left(\frac{-d}{\sqrt{D\tau}}\right) \cdot (1 + \omega^2\tau^2)^{-1/4} \cdot \exp\left(\frac{-d}{\sqrt{D\tau}} \left\{ \sqrt{\frac{1}{2}(\sqrt{1 + \omega^2\tau^2} + 1)} - 1 \right\}\right) \cdot \cos\left\{ \frac{\tan^{-1}(\omega\tau)}{2} + \frac{d}{\sqrt{D\tau}} \sqrt{\frac{1}{2}(\sqrt{1 + \omega^2\tau^2} - 1)} \right\} \quad (4.5)$$

where  $\omega$  is the Larmor frequency,  $d$  is the distance between the two innermost contacts, and  $\tau$  is the spin lifetime.

The Larmor frequency is given by  $\omega = 2\pi g\mu_B B / \hbar$ , where  $g$  is the Lande  $g$ -factor,  $\mu_B$  is the Bohr magneton, and  $B$  is the applied out-of-plane magnetic field. For long devices with  $d$  much larger than the spin diffusion length,  $L_{SD} = \sqrt{D\tau}$ , eq. (4.5) predicts the  $V_s$  versus  $B$  curve with damped oscillations in the tails.<sup>17</sup> Since such oscillations are absent in our data, it is possible to use the small- $d$  asymptote of eq. (4.5),

$$V_s(B) = \frac{A\sqrt{D\tau}}{\sigma(T)\sqrt{2}} \frac{\sqrt{\sqrt{1 + \omega^2\tau^2} + 1}}{\sqrt{1 + \omega^2\tau^2}} \quad (4.6)$$

The shape predicted by eq. (4.6) is universal, in the sense that it depends only on the product  $\omega\tau$ . After the value  $\tau$  was determined from the fit, the corresponding spin diffusion length was calculated with this  $\tau$  and was compared with  $d$  to test whether the small- $d$  asymptote applies. The fit of our data in Figures 4.3a and 4.3b to eq. (4.6) for the negative and positive applied current appears to be excellent.

The calculated  $\tau$  values are shown in Figure 4.4a. The difference between the  $\tau$  values for the positive and negative currents was taken as the error bar. We see that the

spin lifetime at 20 K was  $\sim 150$  ps and decreased slightly with an increase in temperature from 20 K to 300 K. From this value of  $\tau$  and the value of the diffusion coefficient estimated above, we calculated the spin diffusion length to be  $\sim 205$  nm at room temperature (see Figure 4.4b), which is more than adequate for the industry standard, 22 nm transistor technology currently available. Moreover, since the estimated diffusion length is bigger than the contact spacing of  $d = 60$  nm, it explains the absence of damped oscillations in the tails of the  $V_s$  versus  $B$  curves in Figure 4.3 and justifies the use of eq. (4.6) for analyzing the Hanle data. The value of spin relaxation time observed in our degenerate samples agree within a factor of 2 with the high-temperature values reported by Althammer et al.<sup>21</sup> for a nondegenerate ZnO sample. However, the spin diffusion length observed in their study ( $\sim 6$  nm) was much smaller than the values observed ( $\sim 205$  nm) in our case. We believe that this difference arises because of the lower substrate temperature used by them for depositing ZnO film. Specifically, in order to prepare the desired multilayer device structure for magnetoresistance measurements, Althammer et al.<sup>21</sup> deposited ZnO film at 400 °C. Films prepared at such low temperatures are likely to be of low crystallinity and possess a high concentration of defects such as point defects and dislocations. These defects can significantly reduce the mobility of charge carriers in the film.<sup>22</sup> Using the values of electrical conductivity and the carrier concentration reported by Althammer et al.,<sup>21</sup> we estimated the mobility to be  $\sim 4.2 \times 10^{-5}$  m<sup>2</sup>/Vs in their films at room temperature, which is  $\sim 84$  times smaller than that observed in our films. The lower value of mobility will result in a smaller value of diffusivity ( $D$ ) and hence a smaller spin diffusion length.

In semiconductors, spin relaxation occurs mainly via one of the following three

mechanisms<sup>23</sup>: (a) Elliot-Yafet (EY), (b) Bir-Aronov-Pikus (BAP) and (c) Dyakonov-Perel (DP). The EY mechanism is observed in semiconductors which possess a small bandgap and a large spin-orbit splitting of the valence-band. Since ZnO has a large bandgap and a very small spin-orbit splitting of the valence-band, the EY mechanism is unlikely to play any significant role in the material. The BAP mechanism is observed in semiconductors where a significant concentration of both electrons and holes is present and comes from the spin-flip electron-hole exchange interaction. Since it is extremely difficult to introduce holes in ZnO, the BAP mechanism is also highly unlikely to be present in the material. Therefore, in ZnO, the primary source of spin relaxation is believed to be the Dyakonov-Perel mechanism.<sup>23,24</sup> Moreover, a specific of ZnO, as compared to III-V semiconductors such as GaAs, is that its wurtzite crystal structure gives rise to a strong linear-in-momentum,  $k$ , DP spin relaxation term.<sup>11</sup> This term comes from a linear-in- $k$  spin-orbit term in the electron Hamiltonian, which is allowed due to  $C$ -axis asymmetry in the ZnO crystal structure.<sup>11, 25</sup> In origin, this term is analogous to the linear-in- $k$  Rashba spin-orbit term in the Hamiltonian of a 2D electron.<sup>25</sup> The general expression for the spin relaxation rate, which is commonly used in literature,<sup>8</sup> is comprised of the sum of the conventional cubic and linear-in- $k$  terms:

$$\frac{1}{\tau_{DP}} = \alpha_{DP}^{(3)} \cdot T^3 \cdot \tau_p(T) + \alpha_{DP}^{(1)} \cdot T \cdot \tau_p(T), \quad (4.7)$$

where  $\alpha_{DP}^{(3)}$  and  $\alpha_{DP}^{(1)}$  are the material parameters and  $\tau_p(T)$  is the momentum relaxation time. We note that both terms are strongly temperature dependent, so that, according to

eq. (4.7), the time  $\tau_{DP}^{-1}$  should grow at least 15 times between 20 K and 300 K (i.e., over the temperature range of our study). However, as can be seen in Figure 4.5, this is not actually the case.

To account for the above discrepancy, we would like to point out that eq. (4.7) applies only for a nondegenerate electron gas. In the case of a degenerate system, where Fermi-Dirac statistics needs to be used, the two terms in eq. (4.7) take the following form:

$$\frac{1}{\tau_{DP}^{(3)}} = \alpha_{DP}^{(3)} \frac{\int_0^\infty d\varepsilon \cdot g(\varepsilon) \cdot \tau_p(\varepsilon) \cdot \varepsilon^3 \cdot \frac{\partial f_0}{\partial \varepsilon}}{\int_0^\infty d\varepsilon \cdot g(\varepsilon) \cdot \frac{\partial f_0}{\partial \varepsilon}} \quad (4.8)$$

$$\frac{1}{\tau_{DP}^{(1)}} = \alpha_{DP}^{(1)} \frac{\int_0^\infty d\varepsilon \cdot g(\varepsilon) \cdot \tau_p(\varepsilon) \cdot \varepsilon \cdot \frac{\partial f_0}{\partial \varepsilon}}{\int_0^\infty d\varepsilon \cdot g(\varepsilon) \cdot \frac{\partial f_0}{\partial \varepsilon}}, \quad (4.9)$$

where  $f_0$  is the Fermi distribution function, and  $g(\varepsilon) \propto \varepsilon^{1/2}$  is the density of states. In terms of the Fermi-Dirac integrals defined above, in eq. (4.4), these expressions can be cast in the form:

$$\frac{1}{\tau_{DP}^{(3)}} = \alpha_{DP}^{(3)} \cdot T^3 \cdot \tau_p \frac{F_{5/2}\left(\frac{\mathcal{E}_F}{k_B T}\right)}{F_{-1/2}\left(\frac{\mathcal{E}_F}{k_B T}\right)} \quad (4.10)$$

$$\frac{1}{\tau_{DP}^{(1)}} = \alpha_{DP}^{(1)} \cdot T \cdot \tau_p \frac{F_{1/2}\left(\frac{\mathcal{E}_F}{k_B T}\right)}{F_{-1/2}\left(\frac{\mathcal{E}_F}{k_B T}\right)} \quad (4.11)$$

In eqs. (4.10), (4.11) we neglected the energy dependence of  $\tau_p$  since the mobility,  $\mu = e\tau_p / m^*$ , has only weak temperature dependence between 20 K and 300 K.

In Figure 4.5, we have plotted eqs. (4.10) and (4.11) for the  $T_F$  values between 1000 K and 1500 K, along with the experimentally determined spin relaxation rates. The graph in the figure shown in red is for the eq. (4.10), with the upper bound being for  $T_F = 1000$  K and the lower bound being from  $T_F = 1500$  K. The same temperature bounds are true for the blue graph, which is for eq. (4.11). Since the  $T_F$  values in our films were well between  $\sim 1000$  K and 1500 K at all temperatures, these data sets represent an approximate range of spin relaxation rate values for the entire temperature range. As can be noticed from the figure, even with degeneracy taken into account, the cubic term maintains a steep temperature dependence, while the linear term describes the measured weak  $T$ -dependence of the spin relaxation time more accurately. Based on this, we conclude that it is the linear-in- $k$ , spin-orbit term in the Hamiltonian, specific to the wurtzite structure, which is responsible for the spin relaxation in our ZnO samples.



#### 4.4 Conclusion

In conclusion, we have shown that degenerately doped ZnO has a relatively long spin diffusion length ( $\sim 205$  nm). We demonstrated that the electron degeneracy plays a key role in the weak temperature dependence of the spin relaxation time observed. We also identified that the leading mechanism of spin relaxation is the linear-in- $k$  Dyakonov-Perel mechanism resulting from the wurtzite crystal structure of ZnO. As a final remark, we note that, aside from the DP mechanism, there are two other spin-orbit related mechanisms, which can lead to the spin relaxation in semiconductor structures. The Bir-Aronov-Pikus mechanism<sup>23</sup> is based on scattering of electrons by holes, and thus it is inefficient in degenerate n-type structures. Concerning the Elliot-Yafet mechanism<sup>23</sup>, the numerical estimates made by Harmon et al.<sup>25</sup> demonstrate that it is far too weak to account for the experimental spin relaxation times in ZnO.

#### 4.5 References

1. Awschalom, D. D.; Flatté, M. E. *Nature Phys.* **2007**, *3*, 153-159.
2. Prestgard, M. C.; Siegel, G. P.; Tiwari, A. *Adv. Mat. Lett.* **2014**, *5*, 242-247.
3. Chambers, S.A. *Materials Today* **2002**, *5*, 34-39.
4. Snure, M.; Kumar, D.; Tiwari, A.; *JOM* **2009**, *61*, 72-75.
5. Gedamu, D.; Paulowicz, I.; Kaps, S.; Lupan, O.; Wille, S.; Haidarschin, G.; Mishra, Y. K.; Adelung, R. *Adv. Mater.* **2014**, *26*, 1541-1550.
6. Mishra, Y. K.; Chakravadhanula, V. S. K.; Hrkac, V.; Jebril, S.; Agarwal, D. C.; Mohapatra, S.; Avasthi, D. K.; Kienle, L.; Adelung, R. *J. Appl. Phys.* **2012**, *112*, 064308(1)-(5).
7. Prestgard, M. C.; Tiwari, A. *Appl. Phys. Lett.* **2014**, *104*, 122402(1)-(4).
8. Ghosh, S.; Sih, V.; Lau, W.H.; Awschalom, D. D.; Bae, S.-Y.; Wang, S.; Vaidya, S.; Chapline, G.; *Appl. Phys. Lett.* **2005**, *86*, 232507(1)-(3).
9. Braunstein, R.; Kane, E. O. *J. Phys. Chem. Solids* **1962**, *23*, 1423-1431.
10. Fan, W.J.; Xia, J. B.; Agus, P. A.; Tan, S. T.; Yu, S. F.; Sun, X. W. *J. Appl. Phys.* **2006**, *99*, 013702(1)-(4).
11. Lew Yan Voon, L. C.; Willatzen, M.; Cardona, M.; Christensen, N. E. *Phys. Rev. B* **1996**, *53*, 10703-10714.
12. *Semiconductors and Semimetals*; Willardson, R. K.; Beer, A. C., Eds.; Academic Press: New York, 1967; pp. 71.
13. Baer, W. S. *Phys. Rev.* **1967**, *154*, 785-789.
14. Landsberg, P.T.; *Thermodynamics and Statistical Mechanics*; Oxford University Press: Oxford, 1978.
15. Dash, S. P.; Sharma, S.; Patel, R. S.; de Jong M. P.; Jansen, R. *Nature* **2009**, *462*, 491-494.
16. Gray, N. W.; Tiwari, A. *Appl. Phys. Lett.* **2011**, *98*, 102112(1)-(3).
17. Zhou, Y.; et al. *Phys. Rev. B* **2011**, *84*, 125323(1)-(7).
18. Roundy, R. C.; Prestgard, M. C.; Tiwari, A.; Raikh, M. E. *Phys. Rev. B* **2014**, *90*,

205203(1)-(8).

19. Sasaki, T.; Oikawa, T.; Suzuki, T.; Shiraishi, M.; Suzuki, Y.; Noguchi, K. *IEEE Trans. Magnet.* **2010**, *46*, 1436-1439.
20. Aoki, Y.; et al. *Phys. Rev. B* **2012**, *86*, 081201(1)-(4).
21. Althammer, M.; Karrer-Muller, E.-M.; Goennenwein, S. T. B.; Opel, M.; Gross, R. *Appl. Phys. Lett.* **2012**, *101*, 082404(1)-(4).
22. Brillson, L. J.; Zhang, Z.; Dutt, D. R.; Look, D. C.; Svensson, B. G.; Kuznetsov, A. Y.; Tuomisto, F. *Phys. Status Solidi B* **2013**, *250*, 2110-2113.
23. Bandyopadhyay, S.; Cahay, M. *Introduction to Spintronics*; CRC Press: Boca Raton, 2008.
24. Dyakonov, M. I.; Perel, V. I. *Sov. Phys. JETP* **1974**, *33*, 1053.
25. Harmon, N. J.; Putikka, W. O.; Joynt, R. *Phys. Rev. B* **2009**, *79*, 115204(1)-(6).

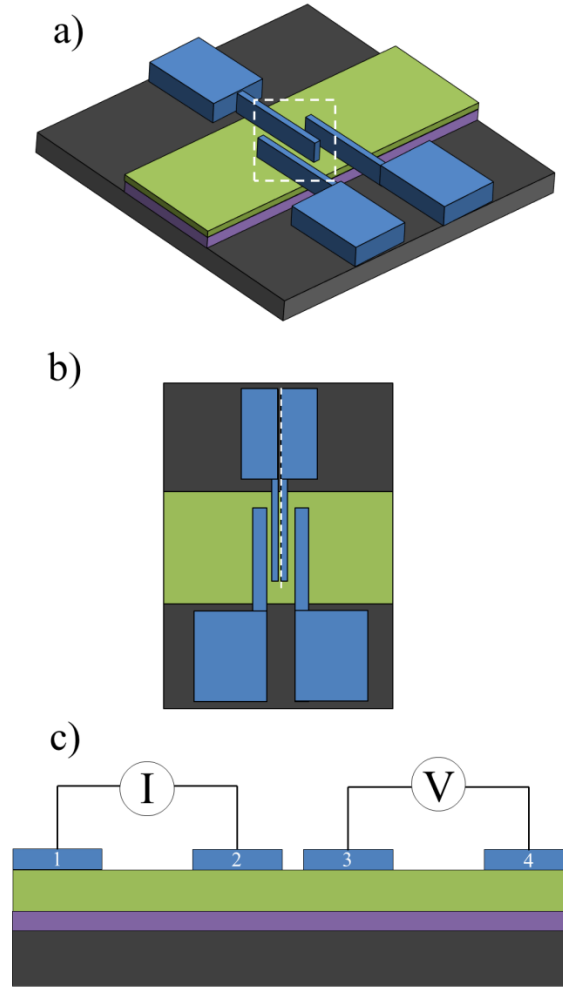


**Figure 4.1 Device structure used for nonlocal Hanle measurements.** For fabricating the desired 4T Hanle device, initially a) a three-probe structure was fabricated, where the base portion (in dark gray) represents the substrate, on top of that is the ZnO layer (in purple), a thin layer of MgO (in green), and NiFe contact pads (in blue). Following the fabrication of the three-probe structure, b) the four-probe device was fabricated by cutting the center contact in half using a FIB. For testing, c) the NiFe contact pads were magnetized in the plane of the device and a current was applied between contacts 1 and 2. The voltage generated between contacts 3 and 4 was measured in the presence of an external, out-of-plane magnetic field which was swept from -4 kG to 4 kG.

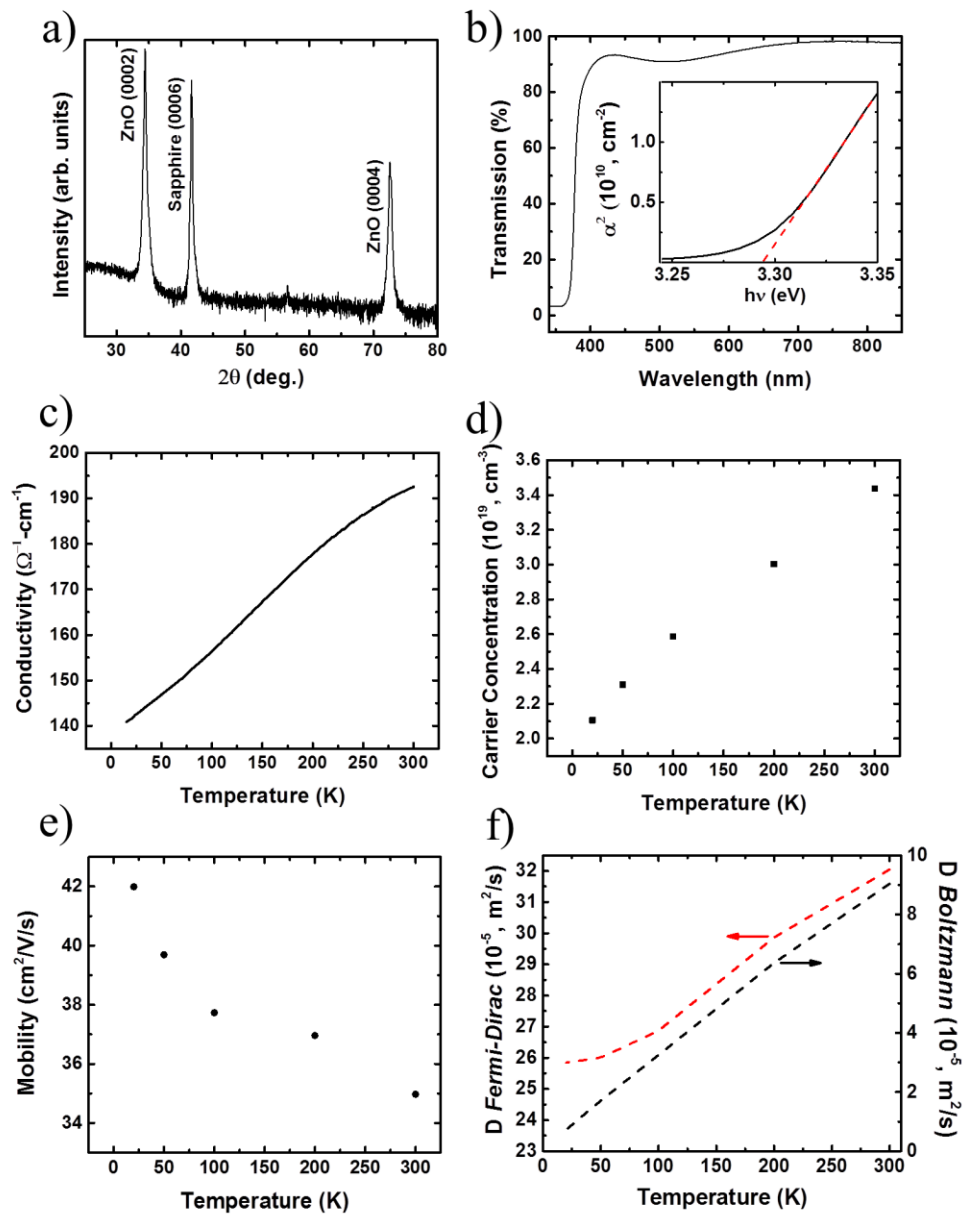


**Figure 4.2 ZnO thin film characterizations.** (a) X-ray diffraction showing C-axis-aligned growth of ZnO atop the sapphire (0001) substrate. (b) UV-Vis spectroscopy showing the transparency of the ZnO film. The inset shows the plot of absorption coefficient squared versus energy, indicating the direct bandgap nature of the film. (c) Conductivity versus temperature data. (d) Carrier concentration versus temperature data as determined via Hall effect measurements. (e) The calculated mobility of carriers in the ZnO film. (f) The diffusion coefficient as calculated using Fermi-Dirac (red curve) and Boltzmann statistics (black curve).

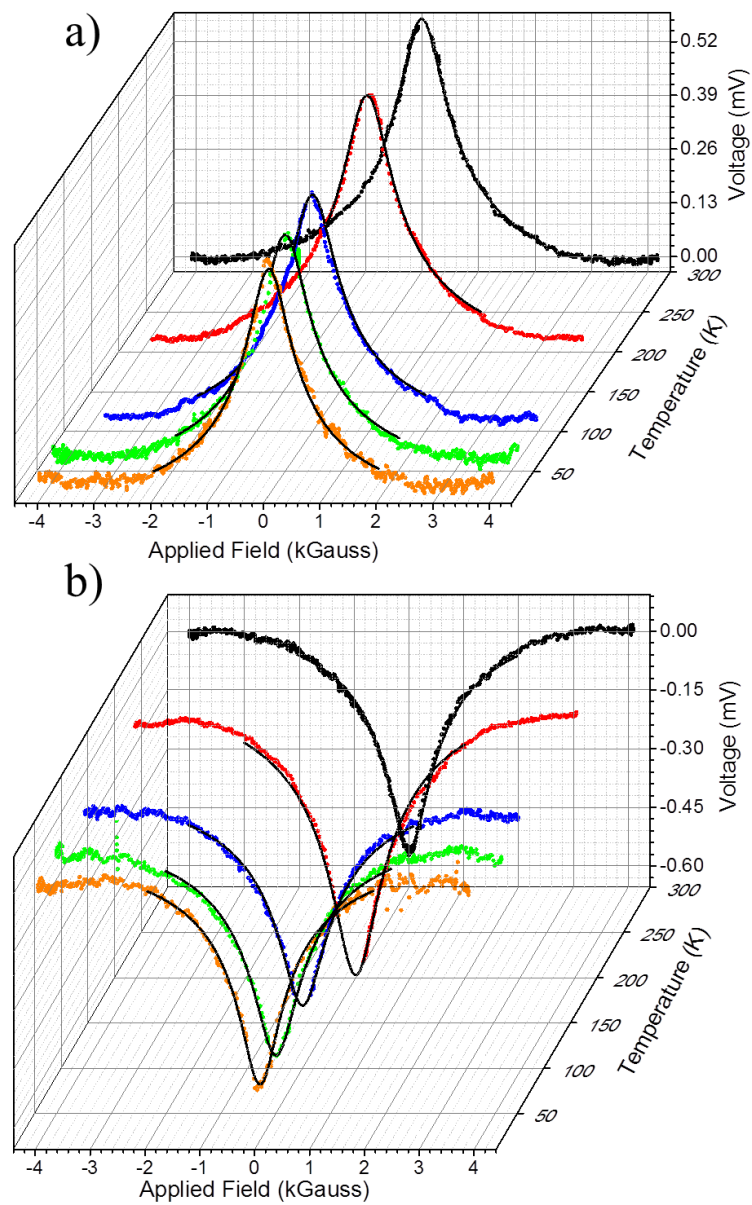


**Figure 4.3 ZnO Hanle curves and corresponding fittings.** The Hanle curves and fittings to eq. (4.6) for: (a) negative current and (b) positive current.

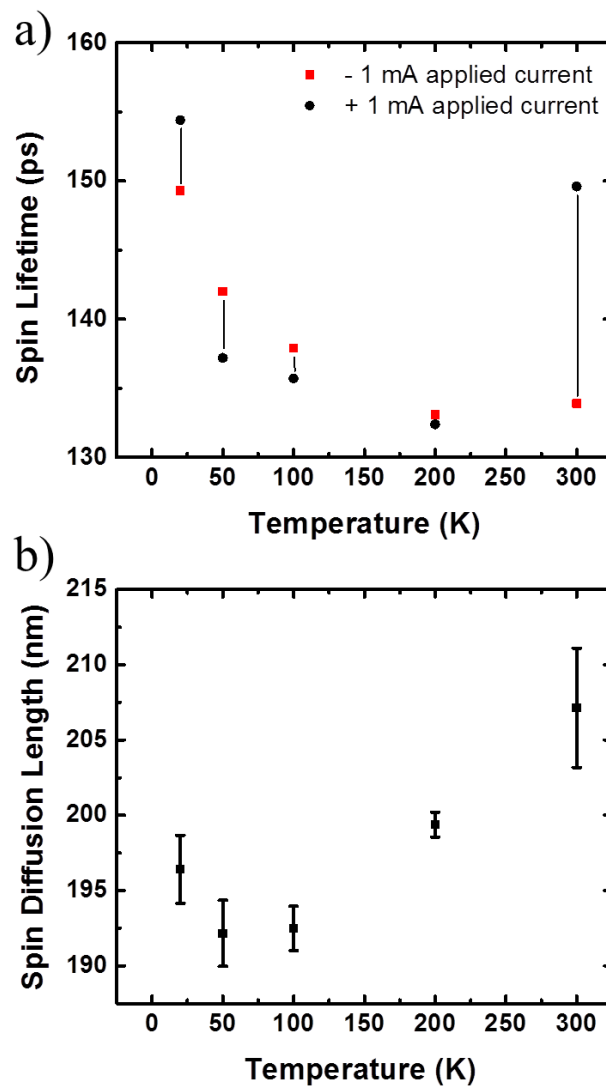


**Figure 4.4: Calculated spin lifetime and spin diffusion length in ZnO.** (a) The spin lifetime as a function of temperature for ZnO. The red and black points indicate the corresponding data for the negative and positive currents, respectively. (b) The calculated spin diffusion length as a function of temperature.

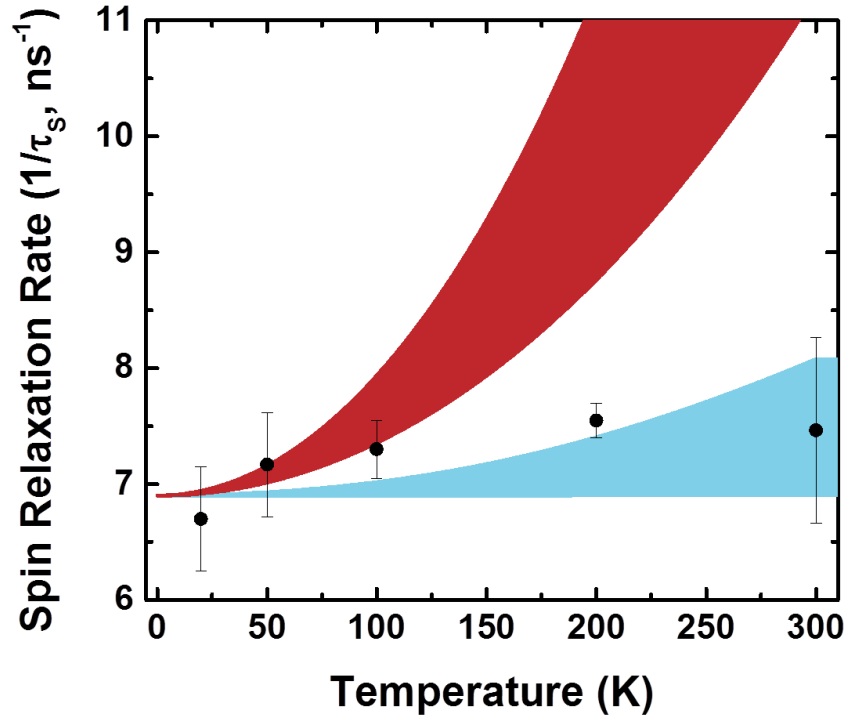


**Figure 4.5 Spin relaxation rate fit to linear and cubic Dyakonov-Perel terms.** The fitting of the spin relaxation data to eqs. (4.10) and (4.11) for  $T_F$  values between 1000 K and 1500 K. The portion in the graph indicated in red is for the fit to eq. (4.10), with the upper bound being for  $T_F = 1000$  K and the lower bound being from  $T_F = 1500$  K. The same bounds are true for the blue graph, which is for eq. (4.11).



## CHAPTER 5

### OBSERVATION OF THE INVERSE SPIN HALL

#### EFFECT IN ZINC OXIDE THIN FILMS<sup>4</sup>

The inverse spin Hall effect (ISHE) is a newly discovered, quantum mechanical phenomenon where an applied spin current results in the generation of an electrical voltage in the transverse direction. It is anticipated that the ISHE can provide a more simple way of measuring spin currents in spintronic devices. The ISHE was first observed in noble metals that exhibit strong spin-orbit coupling. However, recently, the ISHE has been detected in conventional semiconductors (such as Si and Ge), which possess weak spin-orbit coupling. This suggests that large spin-orbit coupling is not a requirement for observing the ISHE. Here, we have reported the observation of the ISHE in an alternative semiconductor material, zinc oxide (ZnO), using all-electrical means. In our study, we found that when a spin-polarized current is injected into ZnO film from a NiFe ferromagnetic injector via an MgO tunnel barrier layer, a voltage transverse to both the direction of the current as well as its spin-polarization is generated in the ZnO layer. The polarity of this voltage signal was found to flip on reversing the direction of the

---

<sup>4</sup> This chapter is based on the paper entitled: “Observation of the inverse spin Hall effect in ZnO thin films: an all-electrical approach to spin injection and detection” M. C. Prestgard and A. Tiwari, Appl. Phys. Lett. (2014) 104, 122402. © Copyright 2014, AIP Publishing LLC. Reprinted with permission.

injected current as well as on reversing the polarization of the current, consistent with the predictions of the ISHE process. Through careful analysis of the ISHE data, we determined a spin-Hall angle of approximately  $1.651 \times 10^{-2}$  for ZnO, which is two orders of magnitude higher than that of silicon. Observation of a detectable room-temperature ISHE signal in ZnO via electrical injection and detection is a groundbreaking step that opens a path towards achieving transparent spin detectors for next-generation spintronic device technology.

### 5.1 Introduction

As one of the most extensively studied semiconductor systems, zinc oxide and its derivatives have become increasingly prevalent in everyday technologies. The interest surrounding the ZnO system stems from its highly desirable and unique material properties. Specifically, ZnO has both a large bandgap of 3.37 eV and also a relatively high conductivity that can be easily tuned through simple material modifications.<sup>1-3</sup> In addition, and perhaps of most interest, are the optical properties of ZnO, namely its transparency and large exciton binding energy (60 meV).<sup>2,3</sup> These traits have resulted in the exploration and use of ZnO for room-temperature lasing and optoelectronic applications.<sup>4-6</sup> The versatile properties and numerous applications of ZnO give it both the potential to continue to satisfy current material needs as well as the capacity to provide a suitable framework for the future development of new and essential technologies. One such area that stands to benefit from this is the current electronics industry.

To this point, electronic devices, particularly transistors, have continued to

miniaturize directly according to the prediction now known as Moore's law.<sup>7-8</sup> However, as devices approach the nanometer scale, adverse effects resulting from quantum confinement limitations will soon dominate and thus greatly hinder any further miniaturization of electronic devices.<sup>9</sup> This impending failure of Moore's law has led researchers to begin focusing on using alternative technologies to further device capabilities.<sup>10,11</sup> Included in these alternative technologies are spintronic devices. Spintronic devices already constitute a significant part of the electronics industry, particularly in the form of magnetic read-heads and magnetic-RAMs.<sup>12,13</sup> However, these devices are based on all-metallic constituents. In order to advance spintronic technology further, it is important to develop all-semiconductor-based spintronic devices where the transport, manipulation, and the detection of spin-polarized electrons can be achieved via semiconductors themselves.<sup>13-16</sup> In the past, significant research efforts have been focused on semiconductor-based spintronic devices, and a good understanding has been reached on the first two aspects, namely, on the transport and manipulation of spin-polarized carriers. However, there has still not been much progress in the field of semiconductor-based spin detectors. There has recently been a focus on examining spin-based effects and how these effects can be utilized for detecting spin-polarized carriers in spintronic devices.<sup>17-20</sup> One such effect is the spin Hall effect (SHE) and its counterpart, the inverse spin Hall effect (ISHE).

The spin-Hall effects refer to the coupling of spin and charge currents within a material. In the SHE, an applied charge current generates a transverse spin current.<sup>21</sup> Although the SHE is a well-known, intrinsic material property, investigation into it has been limited by difficulties in the direct observation of spin currents. On the other hand,

in the case of ISHE, an applied spin current results in the generation of an electrical voltage in the transverse direction.<sup>22</sup> This makes observation of the ISHE much more easily attainable than the SHE, as the electrical voltage can be measured simply via traditional electrical means.

In an ISHE process, the magnitude of the voltage generated, that is, the ISHE signal, is directly proportional to the degree of spin-orbit coupling within a material.<sup>23</sup> For materials with large spin-orbit coupling, such as platinum, the transverse voltage generated can easily be used to detect spin accumulation. However, these materials cannot be integrated in traditional gate-type structures, which makes them nonideal for integration into current electronics. Because of this, it is necessary to discover semiconductor materials that show a strong ISHE signal. Recently, the ISHE has been reported in some common semiconductors, including Si and Ge, despite their having low spin-orbit coupling.<sup>20,24</sup> This is due to the fact that the ISHE signal is directly proportional to the product of the spin-orbit coupling and the resistivity of the material, which makes it possible to observe the ISHE in materials with low spin-orbit coupling through modulation of the resistivity through doping.<sup>20</sup> In this paper, we are reporting the observation of an ISHE signal in ZnO using an all-electrical method and the subsequent calculation of its spin-orbit coupling and analysis of the potential of ZnO for dual optoelectronic-spintronic devices.

## 5.2 Experimental Procedure

Thin films of ZnO were deposited using a pulsed laser deposition technique (PLD) under  $10^{-4}$  Torr of O<sub>2</sub> pressure at 700°C. For this, a highly dense ZnO target was

ablated using a Lambda Physik COMPEX Pro KrF excimer laser (wavelength =248 nm, pulse width = 25 ns, repetition rate= 10 Hz), giving approximately 200 nm thick films for a total of 8,000 incident laser pulses. The films were characterized using a Philips X'Pert X-ray diffractometer to examine the crystal quality and orientation. Further characterization of the ZnO films was performed using UV-Vis spectroscopy (Lambda 950 model spectrometer). Finally, in order to characterize the overall electrical quality of the films, resistivity versus temperature measurements were conducted in a closed-cycle cryostat over the temperature range 15 – 300 K. On the well-characterized ZnO films, an approximately 4 nm thick MgO tunnel barrier layer was deposited using PLD technique. The as-deposited layers were then patterned using a negative resist to form the desired “T” structure and etched using a dilute acid mixture (200 mL H<sub>2</sub>O: 1.5 mL H<sub>3</sub>PO<sub>4</sub>: 0.1 mL HCl). The negative resist was then removed using acetone. Photolithography was then performed in order to pattern the substrate for the e-beam evaporation of the rectangular NiFe channel (Denton SJ20C).

### 5.3 Results and Discussion

The structural characterizations showed that the ZnO films were of high crystal quality, transparent, and possessed relatively high conductivities. As shown in Figure 5.1, the XRD results indicate that the ZnO thin films grown were highly C-axis aligned. The UV-Vis spectroscopy results proved that the ZnO thin films were transparent, thereby again confirming their high quality (see Figure 5.2a). The next characterization of the ZnO film was the measurement of electrical resistivity as a function of temperature. The results, as presented in Figure 5.2b, illustrate that the ZnO thin films were insulating, as

was to be expected, but at the same time they were of relatively low resistivity as compared to stoichiometric ZnO. Following these characterizations and the subsequent depositions of MgO and NiFe, the completed devices (illustrated in Figures 5.3a and 5.3b) were loaded into the ISHE electrical measurement system for testing.

The operation of the test device can be understood by examining the schematic shown in Figure 5.3a. An in-plane magnetic field was applied in order to magnetically polarize the spins in the NiFe film. The polarized carriers were then forced to move from point 'a' in the NiFe to point 'd' in the ZnO. This was done by applying a current between these two points. By passing a current between 'a' and 'd', the spin-polarized carriers in the NiFe first travel from point 'a' to point 'b'. At point 'b', the polarized carriers then tunnel from the NiFe through the MgO barrier into the ZnO (point 'c'), as is shown in the cross-sectional view in Figure 5.3b. Upon tunneling into the ZnO, the ISHE voltage signal develops between points c' and c'' due to the SOC in the ZnO layer. After this, the polarized carriers continue traveling along the long ZnO channel until they reach point 'd'.

In order to probe the ISHE signal, the spin orientation of the injected carriers was modulated by changing the direction of the applied magnetic field. Specifically, the magnetic field along the length of the NiFe strip was swept from +3 kG to -3 kG, during which time the voltage signal in the transverse channel was measured between points c' and c''. As the direction of the magnetic field was reversed, it was expected that the voltage should change from  $+V_{\text{ISHE}}$  to  $-V_{\text{ISHE}}$  upon changing the sign of the applied field. However, the actual signal (Figure 5.3) was found to be more complicated. This is because there is an additional contribution to the voltage which arises because of the

magnetoresistance (MR) of the NiFe layer. However, when we examine the relative values of the voltages at the applied magnetic fields of +3 kG and -3 kG, the presence of the anticipated ISHE signal is evident. Specifically, as can be seen in Figure 5.4, there is a noticeable difference between the voltage at +3 kG and -3 kG, thereby indicating that the curve is not purely due to MR. As per the predictions of the ISHE theory, it was also expected that the ISHE signal should flip upon changing the sign of the spin injection current, which was verified via the +1 mA and -1mA scans, Figures 5.4a and 5.4b.

By subtracting out the MR contribution, the ISHE signal (Figure 5.5) was determined. Figures 5.5a and 5.5b shows the ISHE signal for the positive and negative applied current, respectively. The experimentally determined data are shown as solid points, with curves illustrating the anticipated behavior. The low-field data points, from approximately +0.5 kG to -0.5 kG, are shown with less color saturation than the high-field data. This is because the large MR background that was present significantly limits detection of the ISHE signal within this low-field range. Thus the color saturation in Figure 5.5 allows us to differentiate between the well-defined, high-field data and the uncertain, low-field data. From these plots, we are able to quantitatively determine the value of  $V_{\text{ISHE}}$ . As was explained previously, the  $V_{\text{ISHE}}$  is simply the average of the voltages at positive and negative 3 kG field values. From this, we then calculated the degree of spin-orbit coupling, specifically the spin-Hall angle, in the ZnO film. As can be seen in eq. (5.1), the spin-Hall angle ( $\theta_{\text{SHE}}$ ) depends on the  $V_{\text{ISHE}}$ , the resistivity of the ZnO film ( $\rho_{\text{N}}$ ), the injected spin-polarized charge current ( $I_{\text{s}}$ ), and the width of the ZnO channel ( $w$ ).

$$\theta_{SHE} = \frac{V_{ISHE} \cdot w}{\rho_n \cdot I_s} \quad (5.1)$$

For this calculation,  $V_{ISHE}$  was determined to be approximately 0.6  $\mu\text{V}$  from Figure 5.5. Resistivity was taken as 5.19  $\text{m}\Omega\text{-cm}$ , based on the aforementioned resistivity versus temperature measurements (Figure 5.1d). The width of the channel was approximately 1 mm. The spin current,  $I_s$ , was taken as 0.7 mA, keeping into consideration the fact that a NiFe/MgO tunnel junction can maintain a maximum polarization of 70% on tunneling. Note that here we have assumed that the devices maintains one hundred percent of its polarization on tunneling from the NiFe into the ZnO. However, the actual  $I_s$  may be smaller than 0.7 mA, which makes our calculations here a low-end estimation of the spin-orbit coupling in ZnO. Based on these values, the spin-Hall angle was determined to be approximately  $1.6 \times 10^{-2}$ . Comparing these values to those of silicon, germanium, and platinum, we can see that ZnO has a much large spin-Hall angle than silicon and germanium (with previously reported spin-Hall angles of approximately  $1 \times 10^{-4}$  and  $1 \times 10^{-3}$ , respectively) and lower than that of platinum (average spin-Hall angle previously reported as approximately  $8 \times 10^{-2}$ ).<sup>20,24,25</sup>

#### 5.4 Conclusion

To summarize, through these all-electrical investigations, we have shown the potential of ZnO thin films in the realm of spintronic devices. We have shown that, at room temperature, there is a visible ISHE signal, which allows us to accurately quantify the spin-orbit coupling in ZnO. This quantification has shown us that the spin-Hall angle



of ZnO is approximately 100 times that of Si and 10 times that of Ge, thereby illustrating its potential over other semiconductors. We believe, through minimal material modifications to ZnO, it should be possible to enhance its ISHE response to a point where it can provide as strong of a signal as Pt. With this strong evidence supporting the use of ZnO in spin detection techniques, it seems only a matter of time before we are able to develop transparent devices capable of coupling the optoelectronic properties of ZnO with its newfound spintronic potential.

### 5.5 References

1. Pearton, S. J.; et al. *J. Appl. Phys.* **2003**, *93*, 1-13 (2003).
2. Coleman, V. A.; Jagadish, C. Basic Properties and Applications of ZnO. in *Zinc Oxide Bulk, Thin Films, and Nanostructures: Processing, Properties, and Application*, Jagadish, C.; Pearton, S. J., Eds.; Elsevier: Oxford, 2006; 1-16.
3. Ghosh, S.; Sih, V.; Lau, W. H.; Awschalom, D. D.; Bae, S.-Y.; Wang, S.; Vaidya, S.; Chapline, G.; *Appl. Phys. Lett.* **2005**, *86*, 232507(1)-(3).
4. Bagnall, D. M.; Chen, Y. F.; Zhu, Z.; Yao, T.; Koyama, S.; Shen, M. Y.; Goto, T. *Appl. Phys. Lett.* **1997**, *70*, 2230-2232.
5. Nanto, H.; Minami, T.; Shooji, S.; Takata, S.; *J. Appl. Phys.* **1984**, *55*, 1029-1034.
6. Wang, Z. L.; *Appl. Phys. A* **2007**, *88*, 7-15.
7. Schaller, R. R. *IEEE Spectrum* **1997**, *34*, 52-59.
8. Thompson, S. E.; Parthasarathy, S. *Materials Today* **2006**, *9*, 20-25.
9. Risch, L. *Mater. Sci. Eng. C* **2002**, *19*, 363-368.
10. Jackson, T. N. *Nat. Mater.* **2005**, *4*, 581-582.
11. Das Sarma, S. *Am. Sci.* **2001**, *89*, 516-523.
12. Johnson, M.; *J. Phys. Chem. B* **2005**, *109*, 14278-14291.
13. Wolf, S. A.; Awschalom, D. D.; Buhrman, R. A.; Daughton, J. M.; von Molnár, S.; Roukes, M. L.; Chtchelkanova, A. Y.; Treger, D. M.: *Science* **2001**, *294*, 1488-1495.
14. Prestgard, M. C; Siegel, G.; Ma, Q.; Tiwari, A.; *Appl. Phys. Lett.* **2013**, *103*, 102409(1)-(4).
15. Awschalom, D. D.; Flatté, M. E.; *Nat. Phys.* **2007**, *3*, 153-159.
16. Zutic, I.; Fabian, J.; Das Sarma, S.; *Rev. Mod. Phys.* **2004**, *76*, 323-410.
17. Gorodetski, Y.; Niv, A.; Kleiner, V.; Hasman, E. *Phys. Rev. Lett.* **2008**, *101*, 043903(1)-(4).
18. Valenzuela, S. O.; Tinkham, M.; *Nature* **2006**, *442*, 176-179.
19. Uchida, K.; Takahashi, S.; Harii, K.; Ieda, J.; Koshibae, W.; Ando, K.; Maekawa, S.;

- Saitoh, E.; *Nature* **2008**, *455*, 778-781.
20. Ando, K.; Saitoh, E.; *Nature Commun.* **2012**, *3*, 629(1)-(6).
21. Hirsch, J. E. *Phys. Rev. Lett.* **1999**, *83*, 1834-1837.
22. Saitoh, E.; Ueda, M.; Miyajima, H.; Tatara, G. *Appl. Phys. Lett.* **2006**, *88*, 182509(1)-(3).
23. Kimura, T.; Otani, Y.; Sato, T.; Takahashi, S.; Maekawa, S. *Phys. Rev. Lett.* **2007**, *98*, 156601(1)-(4).
24. Koike, M.; Shikoh, E.; Ando, Y.; Shinjo, T.; Yamada, S.; Hamaya, K.; Shiraishi, M.; *Appl. Phys. Express* **2013**, *6*, 023001(1)-(3).
25. Ando, K.; Takahashi, S.; Harii, K.; Sasage, K.; Ieda, J.; Maekawa, S.; Saitoh, E. *Phys. Rev. Lett.* **2008**, *101*, 036601(1)-(4).

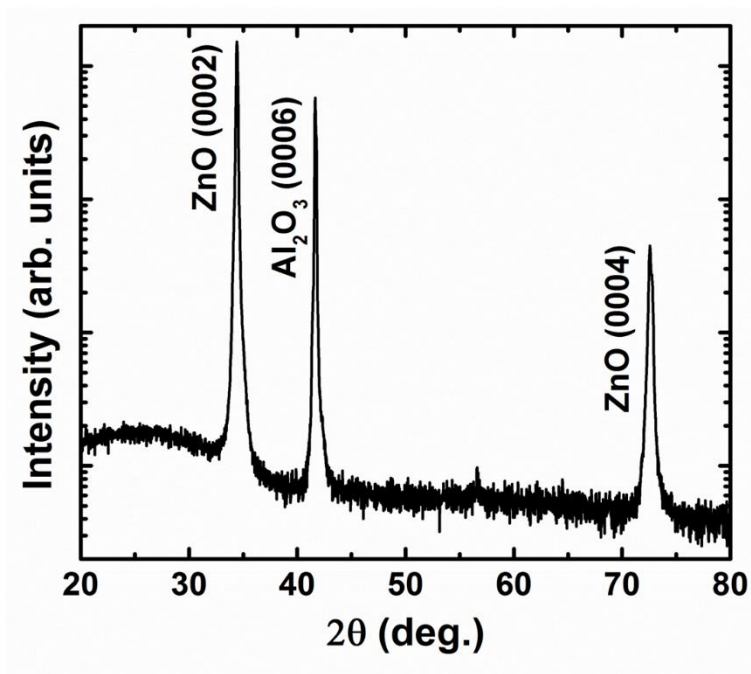


**Figure 5.1 X-ray diffraction pattern of the ZnO thin films.** X-ray diffraction results for the ZnO thin films, showing that the films grown were high quality and C-axis aligned.

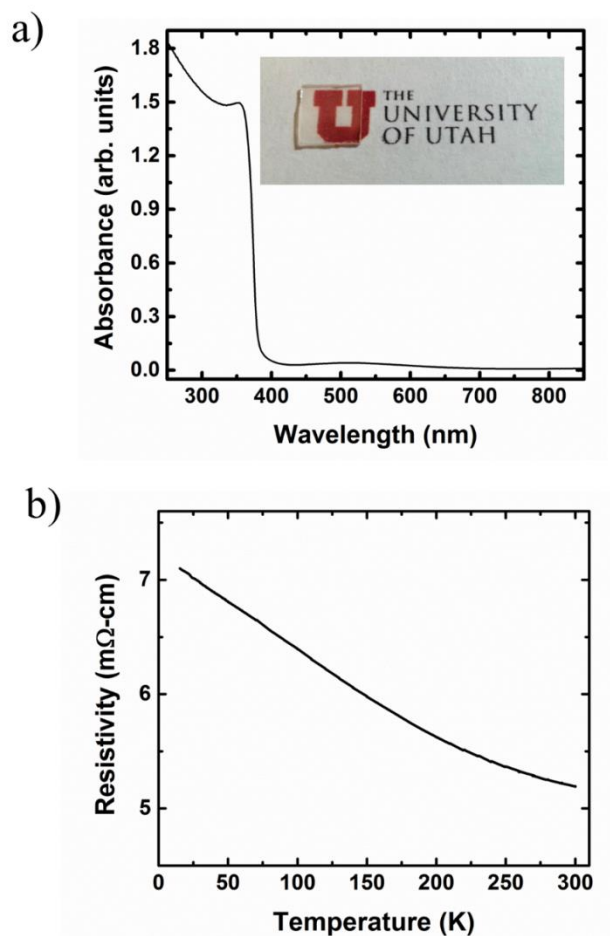


**Figure 5.2 Optical and electrical ZnO thin film characterizations.** (a) UV-Vis spectroscopy data for ZnO. The inset shows a photograph of the ZnO/sapphire sample, illustrating its transparency. (b) Resistivity versus temperature measurements showing that the sample has a relatively low resistivity as compared to stoichiometric ZnO, but that the prepared films were still semiconducting.

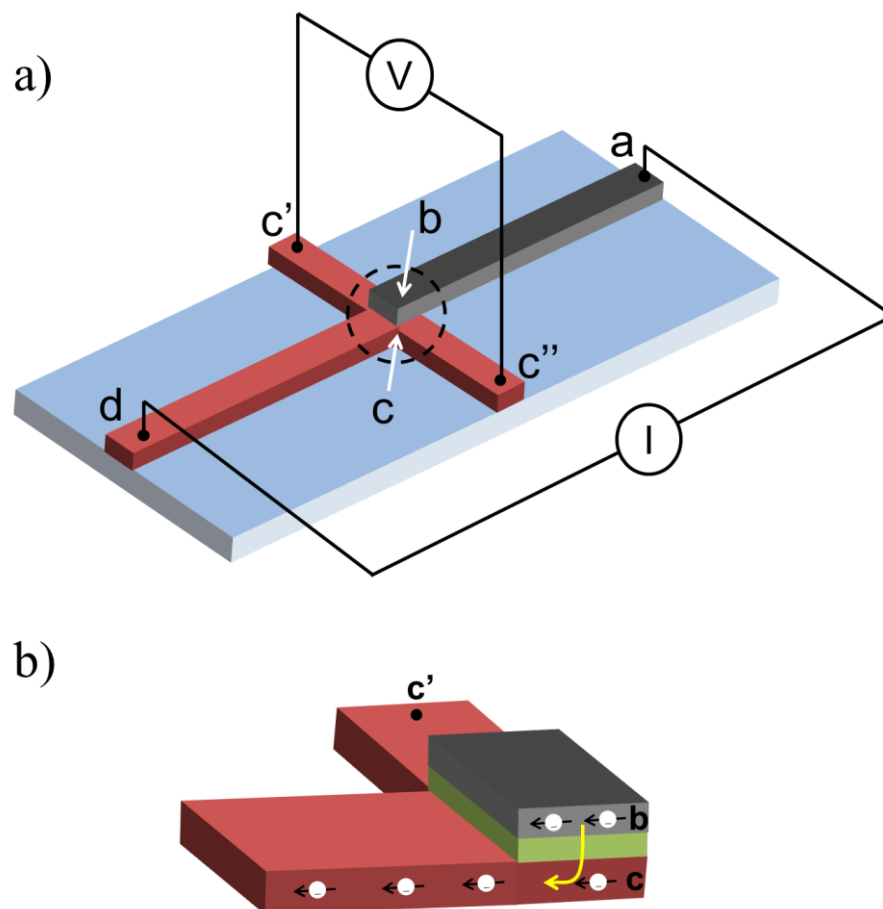


**Figure 5.3 ZnO inverse spin Hall effect device structure.** Schematic illustrations of (a) the entire ISHE device structure and (b) a close-up of the ZnO/MgO/NiFe junction. The dashed circle in Figure 5.3a indicates the close-up region shown in part b, which illustrates the tunneling of polarized electrons from the NiFe into the ZnO via the MgO tunnel barrier. The red indicates ZnO, the blue is for the sapphire substrate, green for MgO, and dark gray for NiFe.

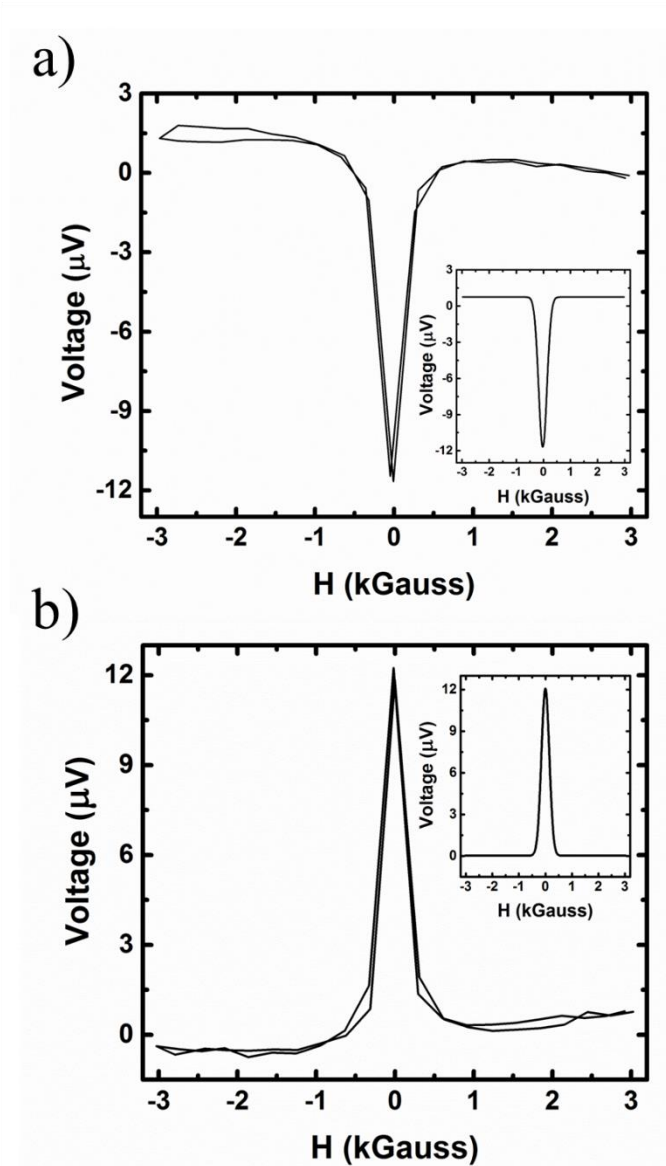


**Figure 5.4 ISHE Device signal: Deconvolution of magnetoresistance, bias, and ISHE contributions.** The voltage between points  $c'$  and  $c''$  as a function of the applied, in-plane magnetic field. These data are a sum of the background, NiFe magnetoresistance contribution, as well as the ZnO inverse spin Hall effect signal. Figures 5.4a and b indicate the scans at +1 mA applied current (from the NiFe to the ZnO) and -1 mA applied current (from the ZnO to the NiFe), respectively. The inset for each shows the background signal used for subtracting the MR contribution from the data.

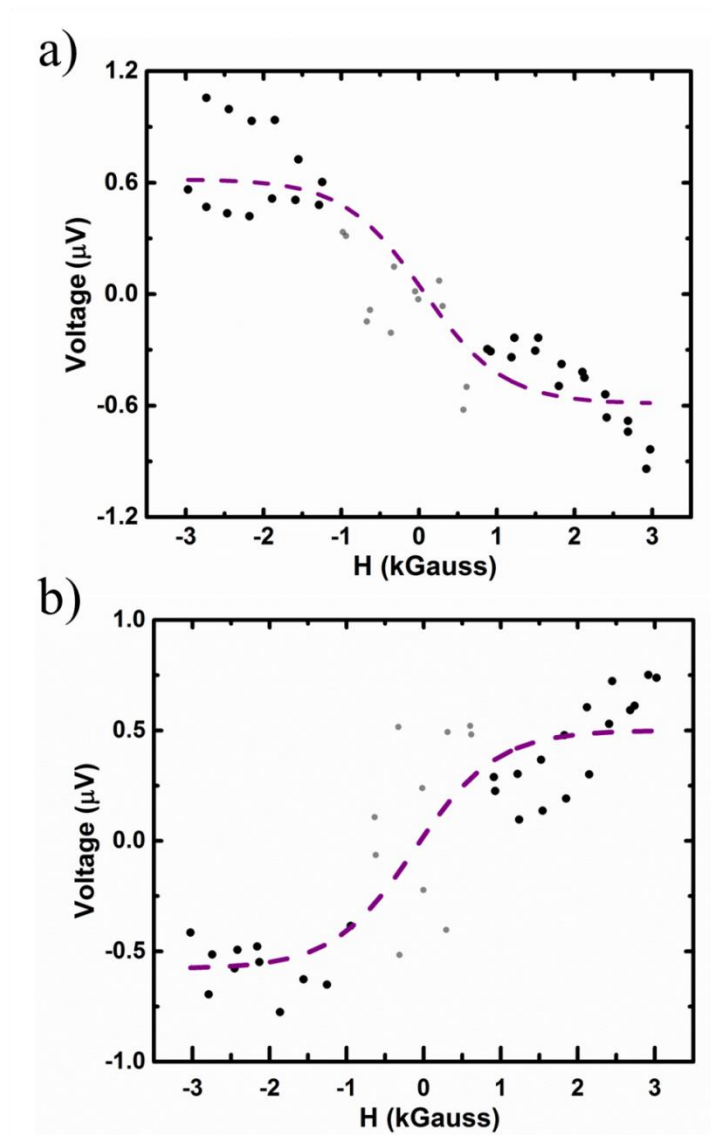


**Figure 5.5 Inverse spin Hall effect signal.** These data were obtained by subtracting out the background contribution from the data presented in Figure 5.4. The gray data points indicate data that are uncertain due to the large magnetoresistance contribution around -0.5 kG to +0.5 kG. The dashed line shows the anticipated ISHE behavior. The data shows a good agreement to the anticipated behavior.



## CHAPTER 6

### SPIN-ORBIT COUPLING IN ZINC OXIDE:

#### INTRINSIC OR EXTRINSIC?

The inverse spin-Hall effect (ISHE) describes the conversion of spin current to charge current in a material due to its spin-orbit coupling (SOC). This effect is particularly useful for the electrical detection of pure spin currents in spintronic devices. Using both electrical and thermal spin injection techniques, we have measured an ISHE response in pulsed laser deposited ZnO thin films. A relatively high spin Hall angle (SHA) of between 1.6% and 9.4% was measured at room temperature via all-electrical testing for samples deposited between 0.1 and 10 mTorr of oxygen. Investigation into the temperature dependence of the SHA in these ZnO films revealed that the mechanism of spin Hall conductivity in ZnO is affected by both intrinsic contributions and extrinsic contributions due to skew-scattering from impurities in the thin films. The temperature dependence of the SHA was confirmed by the thermal spin injection experiments, which utilize the spin Seebeck effect (SSE) to generate spin current. In order to rule out the possibility that the thermal response measured was simply due to the Nernst effect, measurements of the Nernst effect in ZnO and the proximity-induced anomalous Nernst effect in ZnO/YIG were performed. These results showed that the SSE voltage, and resulting SHA calculations, are not complicated by these additional effects. This work

illustrates ZnO has potential as a spin detector, with a spin Hall angle due to extrinsic spin-orbit coupling, nearing that of common metals.

### 6.1 Introduction

The development of next-generation spintronic devices, such as spin caloritronics, requires the effective injection, transport, and detection of spin-polarized carriers. Although progress has been made in the injection and transport of spins, spin detection capabilities have remained limited.<sup>1,2</sup> Metals such as platinum have long been used as spin detectors because of their relatively large spin-orbit coupling (SOC).<sup>3</sup> The SOC allows for the conversion of spin current to charge current through the inverse spin Hall effect (ISHE).<sup>4</sup> The strength of the ISHE response is typically described in terms of the spin Hall angle (SHA), which ranges from 0.3% up to 10% for Au<sup>5,6</sup>, between 1.3% to ~11% for Pt<sup>7,8</sup>, and up to 33% for W.<sup>9</sup> The SHA is defined as the ratio of the spin Hall conductivity (SHC) to the electrical conductivity of the material:  $\theta_{SH} = \sigma_{SH} / \sigma_e$ .<sup>6</sup> Because the SHA is inversely proportional to electrical conductivity, the use of semiconductor spin detectors has recently gained interest, as the electrical properties of these materials are easily tunable through doping.<sup>10</sup>

Values of the SHA have been reported for a variety of semiconductors, such as Si, Ge, and ZnO, as ~0.01%, ~0.1%, and ~1%, respectively.<sup>10-12</sup> The conditions under which these films are grown have a large impact on the films' respective SHAs, as the growth parameters can easily be modified in order to change the electrical conductivity of the resulting films. By optimizing the electrical conductivity, a SHA may be observable even if the material has a small SOC, which is defined by the SHC of the system. Values of the

SHC can be calculated from the SHA and the electrical conductivity in order to reveal information about the nature of the SOC in the material.<sup>13</sup> This requires a study of the temperature dependence of the SHC.<sup>14</sup>

An investigation into this temperature dependence can reveal the origins of the SOC: whether the conversion between spin and charge current is intrinsic due to the band structure of the material or extrinsic due to scattering from defects in the material lattice.<sup>14</sup> The extrinsic origin can further be divided into skew-scattering and side-jump events.<sup>15-18</sup> In skew-scattering, impurities or phonons act as scattering centers and the SOC of the system is determined by the effective SOC of the impurities. Side-jump events are characterized by a splitting of spin-up and spin-down polarized currents due to interactions with defects (including both phonons and defects) in the material. The side-jump mechanism is generally only present in systems that contain very high levels of defects.<sup>18</sup>

Measurement of the SHA through the ISHE requires injection of a spin current. For this study, both the electrical and thermal injection of spin-polarized carriers have been studied. Electrical injection was performed by polarizing electron spins in a permalloy strip, injecting those carriers into the ZnO, and measuring the resulting voltage in a transverse channel as a function of the polarization direction.<sup>12</sup> For thermal spin injection, the spin Seebeck effect (SSE) in a ferrimagnetic insulator (YIG, Yttrium iron garnet) was utilized. In this system, an applied temperature gradient excites magnon motion in the ferrimagnetic layer and pumps spin current into the ZnO due to spin torque transfer at the YIG/ZnO interface.<sup>19,20</sup> This method injects pure spin current; however, this effect can be plagued by the related Nernst effect, which is discussed further in

## Appendix C.

Herein, we are reporting the SHA in ZnO thin films as a function of temperature and composition. The thin films for this study were deposited using a pulsed laser deposition (PLD) technique under a variety of ambient oxygen pressures. The SHA dependence on oxygen pressure was measured and the ZnO thin films deposited under 10 mTorr O<sub>2</sub> were determined to exhibit the largest SHA, ~9.4% at room temperature. Temperature-dependent measurements of both the electrical and thermal injection showed that the SHA decreased with a decrease in temperature. Additionally, the temperature dependence of the spin Hall conductivity (SHC) showed that the SOC in ZnO is primarily extrinsic due to skew-scattering from impurities.

### 6.2 Experimental Methods

The ZnO thin films were deposited on sapphire substrates using a pulsed laser deposition (PLD) technique. A Lambda Physik COMPex Pro KrF excimer laser (pulse width: 25 ns, wavelength: 248 nm) was used to ablate a ceramic ZnO target at a repetition rate of 10 Hz for 8,000 laser pulses. Films were deposited under various oxygen pressures (0.1 mTorr, 1 mTorr, and 10 mTorr), while the sapphire substrates were heated to 650°C. Using these parameters gave films ~200 nm thick, as determined using a Tencor P-10 profilometer. A MgO tunnel barrier layer was subsequently deposited via PLD at room temperature. For this deposition, 30 laser pulses were used to ablate a ceramic MgO target at 1 Hz under vacuum ( $10^{-6}$  Torr), which gave ~3 nm thick films. The ZnO/MgO films were patterned using a dilute acid mixture of hydrochloric and phosphoric acids in water, as was described in Ref. 12. Following patterning of the ZnO/MgO films to the

desired structure, a 10 nm thick strip of NiFe permalloy was deposited using e-beam evaporation according to the method described in Chapter 5 (and the appropriate supplementary information in Appendix B). For testing the samples, electrical spin injection and detection experiments were performed as a function of temperature, giving a  $V_{\text{ISHE}}$  for all samples and temperatures tested. A schematic of this setup is shown in Figure 6.1a.

For SSE testing, ZnO thin films were deposited using PLD. These films were grown on commercially available  $\text{Y}_3\text{Fe}_5\text{O}_{12}/\text{Gd}_3\text{Ga}_5\text{O}_{12}$  substrates (YIG/GGG, MTI Corporation, see Appendix C for additional information). The ZnO films were deposited at 10 mTorr  $\text{O}_2$  at  $650^\circ\text{C}$  and with a repetition rate of 10 Hz for 1,000 laser pulses, giving films  $\sim 25$  nm thick. For testing these films, the sample was arranged as is shown in Figure 6.1b. In this arrangement, the top of the sample (the ZnO layer) was cooled by the coldhead base and the GGG substrate was heated to give a  $\Delta T$  of 3 K across the thickness of the sample. The voltage generated along the length of the ZnO films was measured while the external magnetic field was swept from 0.6 T to -0.6 T. The resulting V-H dependence was used to determine the ISHE voltage resulting from the SSE (referred to herein as  $V_{\text{SSE}}$ ), from which the SHA was calculated. More details are given in Appendix C.

Subsequent Nernst and proximity-induced anomalous Nernst tests were performed to ensure these effects were not responsible for the observed  $V_{\text{SSE}}$  signal. Nernst effect testing was performed on a ZnO/sapphire sample in the same method as previously described for SSE testing, except in this case, the temperature gradient was applied from the sapphire to the ZnO, as is shown in Figure 6.1c. The proximity-induced

anomalous Nernst effect testing was performed using the arrangement shown in Figure 6.1d. In this arrangement, the temperature gradient was applied along the width of the ZnO/YIG/GGG sample, the magnetic field was applied in the plane (through the thickness) of the sample, and the voltage was measured along the length of the ZnO film. This arrangement gives only the Nernst effect due to the proximity induced ferromagnetic behavior in the ZnO, with no subsequent SSE response. The resulting proximity-induced anomalous Nernst effect voltage,  $V_N$ , was subtracted from the  $V_{SSE}$  response to give the true  $V_{SSE}$  signal.

### 6.3 Results and Discussion

#### 6.3.1 Electrical spin injection

In order to determine the SHA of the various ZnO thin films, each of the samples was tested according to the method previously outlined in Ref. 12. In this arrangement, the electrons are first polarized in the NiFe contact and then are injected into the ZnO through an MgO tunnel barrier. As this spin current moves into the ZnO channel, a voltage is generated in the transverse direction because of the inverse spin Hall effect (ISHE). The resulting charge voltage was probed by sweeping the applied magnetic field, in order to modulate the orientation of the injected spin current. The final signal measured was then examined to determine the  $V_{ISHE}$ . Because of the local device arrangement, the charge voltage signal also included a background magnetoresistance contribution, which was deconvoluted according to the steps outlined in Chapter 5.

Extraction of the pure ISHE voltage showed the anticipated Boltzmann-like shape for each of the samples tested. An example of one of the V-H curves is shown in Figure

6.2a for the 1 mTorr sample at 300 K. Based on the measured  $V_{ISHE}$  for each of the samples (values shown in Table 6.1, 6.2, and 6.3 for the ZnO films deposited under 0.1 mTorr, 1 mTorr, and 10 mTorr, respectively), the SHA was calculated according to eq. (6.1),

$$\theta_{SH} = \frac{V_{ISHE} \cdot w}{\rho_n \cdot I_S}, \quad (6.1)$$

where  $\theta_{SH}$  is the SHA,  $V_{ISHE}$  is the inverse spin Hall effect voltage,  $w$  is the width of the ZnO channel,  $\rho_n$  is the electrical resistivity of the ZnO film, and  $I_S$  is the spin current.<sup>12</sup> Based on the sample geometry,  $w$  is equal to 1 mm and  $I_S$  is equal to ~0.7 mA, based on the estimations made in Chapter 5. A spin current of 1 mA was injected; however, due to fundamental limits of spin injection, polarization should be ~70% for NiFe with an MgO tunnel barrier. A value of 0.7 mA provides a high-end estimate of the spin injection current; note that a lower value for the  $I_S$  would provide increased SHA values, and thus these calculations are the low-end estimate of the SHA in ZnO. The  $V_{ISHE}$  and  $\rho_n$  are dependent on the sample being tested and the temperature at which the measurement was completed.

In Figures 6.3a and 6.3b, the SHA dependence on composition and temperature are shown, respectively. From the compositional dependence of the SHA, it can easily be seen that an increase in the oxygen pressure during deposition results in a significant increase in the SHA of ZnO films. For samples deposited at 0.1 mTorr, the SHA is equal to ~1.65%, whereas the SHA is ~3.3% for the 1 mTorr samples and ~9.5% for ZnO films

deposited at 10 mTorr O<sub>2</sub>. The SHA also showed a consistent trend with temperature, increasing with an increase in temperature, as shown in Figure 6.3b. The observed trend with temperature mimics that of Pt, where a very small increase with increasing temperature is typically seen.<sup>14</sup> For the 0.1 mTorr sample, a ~46% increase was seen. The 1 mTorr and 10 mTorr samples showed much larger increases with increasing temperature, ~150% and ~140%, respectively, for the 1 mTorr and 10 mTorr samples from 50 K to 300 K. A contour plot showing the combination of the temperature and compositional dependencies of the SHA is given in Figure 6.4. In order to confirm the observed temperature dependence of the SHA, subsequent thermal spin injection experiments were performed.

### 6.3.2 Thermal Spin Injection

For thermal spin injection testing, the spin Seebeck effect (SSE) was utilized to pump spin current into the ZnO films, according to the method previously outlined. Because in this method the injected spin current is often much lower than in electrical spin injection experiments, only the sample with the largest SHA, the 10 mTorr sample, was tested. The SSE curve measured at 300 K is shown in Figure 6.2b. The temperature dependence of this response showed that the voltage decreased with a decrease in temperature, shown in Figure 6.5a. To determine the temperature dependence of the SHA, we must use eq. (6.1), rewritten below as eq. (6.2), adapted for the thermal injection of spin current:

$$\theta_{SH} = \frac{V_{SSE} \cdot w}{\rho_n \cdot I_s^{magnon}}, \quad (6.2)$$



where the constants are the same as previously outlined, with the only differences being that  $V_{\text{ISHE}}$  has been replaced by  $V_{\text{SSE}}$  and  $I_s$  is now written as  $I_s^{\text{magnon}}$ . Because the spin current is pumped via magnon excitation in the YIG,  $I_s$  is no longer temperature-independent. Rather,  $I_s$  is determined according to eq. (6.3) (simplified version shown as eq. (6.4)):

$$I_s = \Delta T \cdot \left( \frac{P(T)}{\alpha(T)} \right) \int_0^{T_M/T} \frac{T}{T_M} \cdot \frac{s^2 ds}{4 \sinh^2(s/2)} \quad (6.3)$$

$$I_s(T) = \Delta T \cdot \frac{P(T)}{\alpha} \cdot I_s'(T), \quad (6.4)$$

where  $\Delta T$  is the temperature gradient applied,  $\alpha$  is the Gilbert-damping constant, which is assumed to be temperature independent,<sup>21</sup>  $I_s'$  is a temperature-dependent term that depends on the magnon temperature and is calculated from the integral in eq. (6.3), and  $P(T)$  is a nearly temperature-independent constant.  $I_s'$  and  $P(T)$  can be further expanded according to eqs. (6.5) and (6.6), respectively<sup>21,22</sup>:

$$I_s'(T) = \frac{T}{4T_M} \left\{ \begin{aligned} & 2 \frac{T_M}{T} \left[ \frac{T_M}{T} + 4 \log(1 - \exp(-T_M/T)) + \frac{T_M}{T} (-\coth(T_M/2T)) \right] + 16 \\ & - 8 \sum_{k=1}^{\infty} \frac{\exp(-T_M \cdot k/T)}{k^2} \end{aligned} \right\} \quad (6.5)$$

$$P(T) = \frac{0.1k_B\tau_s(T)}{8\pi^5\hbar^3} \times N_{\text{int}}(T) \cdot (J_{sd}^2 S_0) \cdot \chi_n \left( \frac{a}{\lambda_s(T)} \right)^3 \cdot \left( \frac{a_s}{\Lambda} \right), \quad (6.6)$$

where  $T_M$  is the magnon-temperature (560 K for YIG)<sup>22</sup>,  $\tau_s$  is the spin lifetime,  $N_{\text{int}}$  is the number of spins at the interface,  $\lambda_s$  is the spin diffusion length,  $J_{sd}$  is the strength of the s-d exchange interaction at the ZnO/YIG interface,  $S_0$  is size of localized spins,  $a$  is lattice parameter, and  $a_s/\Lambda$  is a term defining effective block spin of the YIG.<sup>22</sup> While  $I_s'$  can be easily calculated from the  $T_M$  and the temperature of the experiment,  $T$ , calculating  $P(T)$  can be quite difficult, as significant knowledge is required about the layers used and the interaction between those layers. As such,  $P(T)$  is usually assumed to be temperature independent in Pt/YIG systems.<sup>22</sup> To assume that this approximation is valid in our system, we need to take into account the spin lifetime,  $\tau_s$ , the spin diffusion length,  $\lambda_s$ , and  $N_{\text{int}}$ , the number of spins at the interface as a function of temperature. Previously reported value for  $\tau_s$  and  $\lambda_s$  as a function of temperature can be used to determine if a temperature-independent  $P$  is a valid approximation in ZnO.<sup>23</sup> For determining the  $N_{\text{int}}$  in ZnO, we can assume that  $N_{\text{int}}$  scales with  $n$ , the carrier concentration. Taking these values into consideration, the  $P(T)$  term shows only a ~3-4% decrease on decreasing the temperature from 300 K to 25 K. Considering that the  $I_s'$  term decreases nearly 90% over the same temperature range, the temperature dependence of  $P$  is significantly smaller than the temperature dependence of  $I_s'$ , so neglecting it for these calculations is a valid assumption.

Because the  $\Delta T$ ,  $P$ , and  $\alpha$  terms are temperature independent, the  $I_s$ , and thus the SHA, scale with  $I_s'$  as follows, eq. (6.7):

$$\frac{I_s(T)}{I_s(300K)} = \frac{I'_s(T)}{I'_s(300K)} \quad (6.7)$$

Thus, the SHA as a function of temperature can thus be expressed as eq. (6.8) (rewritten as eq. (6.9)):

$$\frac{\theta_{SH}(T)}{\theta_{SH}(300K)} = \frac{V_{SSE}(T)}{V_{SSE}(300K)} \cdot \frac{\rho_n(300K)}{\rho_n(T)} \cdot \frac{I'_s(300K)}{I'_s(T)} \quad (6.8)$$

$$\theta_{SH}^{rel} = \frac{V_{SSE}^{rel}}{\rho_n^{rel} I_s'^{rel}}, \quad (6.9)$$

where  $\theta_{SH}^{rel}$  is the relative SHA;  $\theta_{SH}^{rel} = \theta_{SH}(T) / \theta_{SH}(300K)$ , and  $V_{SSE}^{rel}$ ,  $\rho_n^{rel}$ , and  $I_s'^{rel}$  are the relative  $V_{SSE}$ , electrical resistivity, and spin current, respectively, and are shown as a function of temperature in Figure 6.5. The relative electrical resistivity was measured as a function of temperature in the ZnO thin films and the relative spin current was calculated according to eqs. (6.5) and (6.7). In order to calculate the relative  $V_{SSE}$  as shown in Figure 6.5a, the background Nernst effect response was removed from the as-measured spin-Seebeck curves (Figure 6.2b) according to the method described below.

### 6.3.3 Proximity-induced anomalous Nernst effect

The Nernst effect describes the generation of a voltage in a ferromagnetic material perpendicular to both an applied temperature gradient and an external magnetic field. The

Nernst effect response was measured in bulk ZnO and was determined to be within the noise level. However, in the thin films tested, ZnO was deposited on a ferromagnetic insulator, YIG. This allows for the possibility of proximity-induced, anomalous ferromagnetism in the ZnO thin films, as has been illustrated previously in graphene/YIG thin films.<sup>24</sup> In order to determine the magnitude of the proximity-induced anomalous Nernst effect, an alternative SSE testing arrangement (Figure 6.1d) is used. In this arrangement, the temperature gradient is applied along the width of the sample, the voltage is measured along the length, and the magnetic field is applied through the thickness. For any spin current that is injected into the ZnO, because the magnetic field is applied in the same direction, the cross product of the magnetization and the spin-polarization vector,  $\sigma$ , is zero, meaning that no spin Seebeck response will be generated in this arrangement. Thus, any voltage resulting in this testing is purely due to the proximity-induced anomalous Nernst effect in the ZnO, and will thus be defined as  $V_{ANE}$ .

A sample, resulting V-H curve is shown in Figure 6.6. As can be seen, there is a relatively small  $V_{ANE}$  signal, ~40-50 nV. This signal was observed at all temperatures to have a value of ~30 – 50 nV, with a very slight increase in the  $V_{ANE}$  on increasing the temperature. Comparing to the reported spin Seebeck curve shown in Figure 6.2b, the  $V_{ANE}$  background response is smaller. The relative  $V_{SSE}$  data shown in Figure 6.5a were then calculated by subtracting out the  $V_{ANE}$  background from the original spin Seebeck curves. The SHA values were calculated using the values for relative  $V_{SSE}$  at all temperatures. The relative SHA versus temperature is plotted in Figure 6.7. This graph shows a comparison to the relative values determined from electrical spin injection experiments, showing very good agreement between the two spin injection techniques.

### 6.3.4 Spin Hall conductivity

After the SHA was calculated and confirmed via electrical and thermal spin injection experiments, the spin Hall conductivity (SHC) was investigated. The SHC was calculated according to the following equation, eq. (6.10):

$$\sigma_{SH} = \theta_{SH} \cdot \sigma_n, \quad (6.10)$$

where  $\theta_{SH}$  is the spin Hall angle and  $\sigma_n$  is the electrical conductivity. Using the temperature dependent data, the SHC was calculated as a function of temperature. As can be seen in Figure 6.8, the SHC increases slightly with an increase in the temperature. It has been reported that a strongly temperature-dependent SHC is indicative of the presence of defect scattering in the sample, although others have attributed such a strong dependence to a large intrinsic SOC.<sup>14,25</sup> However, without further analysis, the temperature dependence of the SHC cannot reveal the relative strength of the defect contribution to the SOC, specifically the ratio of extrinsic to intrinsic SOC, or the nature of the defects present, that is, impurity or phonon skew-scattering.

### 6.3.5 Spin Hall resistivity and spin-orbit coupling

In order to comment on the relative strength of the intrinsic and extrinsic SOC, the SHC can be modeled as parallel conduction pathways with the total spin Hall conductivity being equal to the sum of the intrinsic and extrinsic SOC contributions to the SHC, according to eq. (6.11):

$$\sigma_{SH} = \sigma_{SH}^{\text{int}} + \sigma_{SH}^{\text{ext}}, \quad (6.11)$$

where  $\sigma_{SH}$  is the spin-Hall conductivity,  $\sigma_{SH}^{\text{int}}$  is the intrinsic spin Hall conductivity, and  $\sigma_{SH}^{\text{ext}}$  is the extrinsic spin Hall conductivity.<sup>14, 26</sup> The  $\sigma_{SH}^{\text{ext}}$  term describes the extrinsic SHC due to both skew-scattering and side-jump events at impurities and phonons.<sup>14</sup> The  $\sigma_{SH}^{\text{ext}}$  is often described as an extrinsic series resistor, with the contributions to the resistivity being from impurities and phonons:  $\rho_{SH}^{\text{ext}} = \rho_{SH}^{\text{imp}} + \rho_{SH}^{\text{phon}}$ , where the spin Hall resistivity (SHR) is defined as:  $\rho_{SH} = \sigma_{SH} / (\sigma_n^2 + \sigma_{SH}^2)$ .<sup>14</sup> For future calculations, the side-jump contribution to the total resistance will be ignored, as this effect is only expected to be nonnegligible in very highly defective samples.<sup>3</sup> According to the effective scaling between side-jump and skew-scattering events, given by Tse and Das Sarma as  $\sigma_{SJ} / \sigma_{SS} \approx (\hbar / \tau) / \varepsilon_F$ ,<sup>27</sup> the side-jump contribution should be  $\sim 1 \times 10^{-5}$  times smaller than the skew-scattering contribution; based on the value of 115.9 meV for the Fermi energy and a spin lifetime of  $\sim 100$  ps.<sup>23</sup>

Adapting eq. (6.11) using the series resistor model, we can determine the anticipated intrinsic and extrinsic behavior. Based on the series resistor model and the equation for SHR, we can calculate both the extrinsic SHC contribution, eq. (6.12), and the overall SHC, eq. (6.13):

$$\sigma_{SH}^{\text{ext}} = \frac{-\rho_{SH}^{\text{ext}}}{\rho_n^2} = -\frac{\rho_{SH}^{\text{imp}} + \rho_{SH}^{\text{phon}}}{\rho_n^2} \quad (6.12)$$

$$\sigma_{SH} = \sigma_{SH}^{int} - \frac{\rho_{SH}^{imp} + \rho_{SH}^{phon}}{\rho_n^2} \quad (6.13)$$

Returning to eq. (6.12), we can assume two different cases: 1) that the SHR due to only impurity skew-scattering is important or 2) that both impurity and phonon skew-scattering play a role. In the first case, neglecting phonon skew-scattering gives the following equation for the total SHR (eq. (6.14)):

$$-\rho_{SH} = \sigma_{SH}^{int} \rho_n^2 - \rho_{SH}^{imp} \quad (6.14)$$

Similarly, for the second case where both impurity and phonon skew-scattering are considered, the total SHR is given by eq. (6.15):

$$-\rho_{SH} = \sigma_{SH}^{int} \cdot \rho_n^2 + \theta_{SH}^{phon} \cdot (\rho_n - \rho_n^{imp}) + \sigma_{SH}^{imp} (\rho_n^{imp})^2 \quad (6.15)$$

These equations were determined according to the methods and assumptions outlined in Ref. 14. Using these equations, the respective intrinsic and extrinsic SHC terms can be extracted. For the first case, plotting the negative SHR versus electrical resistivity, a linear fit of the data will give a slope equal to the intrinsic SHC and an intercept equal to the SHR due to the impurity contribution. These fits, shown in Figure 6.9, gave values of the intrinsic and extrinsic impurity contributions to the total SHC and are reported in Table 6.4.

As can be seen, for each of these fits, the intrinsic SHC is negative and has a

smaller magnitude than the extrinsic contribution. Because the SHC can be positive or negative in semiconductors, depending on impurity concentrations, the negative intrinsic SHC is not unexpected.<sup>28,29</sup> Additionally, based on these results, we expect that a large extrinsic contribution from skew-scattering at impurities is responsible for the large SHA observed. This is also to be expected, as ZnO has a small SOC and observation of the ISHE requires that either the resistivity of the films be very large or that the SOC be enhanced through extrinsic effects.

For the 1 mTorr and 10 mTorr samples, the linear fit is quite good. For the 0.1 mTorr sample, however, there appear to be two regions of linear behavior at high and low values of the electrical resistivity (translating to low and high temperatures, respectively). Thus, the 0.1 mTorr sample data were also fit to the second case, eq. (6.15), as shown in Figure 6.10. Because the 0.1 mTorr sample fit to eq. (6.15) was much better than the fit to eq. (6.14), we expect that the phonon skew-scattering term is nonnegligible for this sample.<sup>14</sup> This indicates that the extrinsic SOC due to skew-scattering still dominates over the intrinsic SOC, and that additional scattering mechanisms are present in the 0.1 mTorr sample, which is consistent, as the low oxygen pressure during deposition increases the risk of defect formation.

#### 6.4 Conclusion

In conclusion, by studying the temperature and compositional dependencies of the spin Hall angle in ZnO, we were able to determine that extrinsic SOC dominates in ZnO. These experiments were performed by growing various films using a pulsed laser deposition technique, while varying the oxygen pressure during which these films were



deposited, and then measuring their spin Hall angle as a function of temperature. Based on these data, we are able to see that the spin Hall angle in ZnO is not only highly dependent on the composition used, it is also highly temperature dependent. From these data, we have found a maximum in spin Hall angle to occur in the ZnO deposited at 10 mTorr O<sub>2</sub>, with a value of approximately 9.5%, which rivals that of some common metals. The temperature dependence of this trend was confirmed via spin Seebeck effect measurements on the 10 mTorr sample. Using the method outlined in Ref. 14, we were then able to calculate the spin Hall conductivity from this data for both the intrinsic and extrinsic SOC. It was also found that the SOC is affected by both intrinsic and extrinsic factors, with the 1 mTorr and 10 mTorr samples having extrinsic impurity skew-scattering contributions, and the 0.1 mTorr sample having both impurity as well as phonon-skew-scattering contributions.

### 6.5 References

1. Wolf, S. A.; Awschalom, D. D.; Buhrman, R. A.; Daughton, J. M.; von Molnár, S.; Roukes, M. L.; Chtchelkanova, A. Y.; Treger, D. M.; *Science* **2001**, *294*, 1488-1495.
2. Awschalom, D. D.; Flattè, M. E. *Nature Physics* **2007**, *3*, 153-159.
3. Hoffmann, A.; *IEEE Trans. Magnet.* **2013**, *49*, 5172-5193.
4. Hung, H. Y.; et al. *J. Appl. Phys.* **2013**, *113*, 17C507(1)-(3).
5. Seki, T.; Hasegawa, Y.; Mitani, S.; Takahashi, S.; Imamura, H.; Maekawa, S.; Nitta, J.; Takanashi, K.; *Nat. Mater.* **2008**, *7*, 125-129.
6. Mosendz, O.; Vlaminck, V.; Pearson, J. E.; Fradin, F. Y.; Bauer, G. E. W.; Bader, S. D.; Hoffmann, A. *Phys. Rev. B* **2010**, *82*, 214403(1)-(10).
7. Ando, K.; Takahashi, S.; Harii, K.; Sasage, K.; Ieda, J.; Maekawa, S.; Saitoh, E. *Phys. Rev. Lett.* **2008**, *101*, 036601(1)-(4).
8. Pai, C.-F.; Liu, L.; Li, Y.; Tseng, H. W.; Ralph, D. C.; Buhrman, R. A. *Appl. Phys. Lett.* **2012**, *101*, 122404(1)-(4).
9. Sherman, E. Y.; Najmaie, A.; van Driel, H. M.; Smirl, A. L.; Sipe, J. E. *Solid State Commun.* **2006**, *139*, 439-446.
10. Ando, K.; Saitoh, E.; *Nat. Commun.* **2012**, *3*, 629(1)-(6).
11. Koike, M.; Shikoh, E.; Ando, Y.; Shinjo, T.; Yamada, S.; Hamaya, K.; Shiraishi, M.; *Appl. Phys. Express* **2013**, *6*, 023001(1)-(3).
12. Prestgard, M. C.; Tiwari, A. *Appl. Phys. Lett.* **2014**, *104*, 122402(1)-(4).
13. Hirsch, J. E. *Phys. Rev. Lett.* **1999**, *83*, 1834-1837.
14. Isasa, M.; Villamor, E.; Hueso, L. E.; Gradhand, M.; Casanova, F. *Phys. Rev. B* **2015**, *91*, 024402(1)-(7).
15. Vignale, G. *J. Supercon. Nov. Magn.* **2010**, *23*, 3-10.
16. Berger, L. *Phys. Rev. B.* **1970**, *2*, 4559-4566.
17. Smit, J. *Physica* **1955**, *21*, 877-887.
18. Smit, J. *Physica* **1958**, *24*, 39-51.

19. Uchida, K.; *et al.*, *Nature Materials* **2010**, 9, 894-897 (2010).
20. Uchida, K.; Ota, T.; Kajiwara, Y.; Umezawa, H.; Kawai, H.; Saitoh, E.; *J. Phys.: Conf. Ser.* **2011**, 303, 012096(1)-(4).
21. Siegel, G.; Prestgard, M. C.; Teng, S.; Tiwari, A. *Sci. Reports* **2013**, 4, 4429(1)-(6).
22. Adachi, H.; Uchida, K.; Saitoh, E.; Ohe, J.; Takahashi, S.; Maekawa, S. *Appl. Phys. Lett.* **2010**, 97, 252506(1)-(3).
23. Prestgard, M. C.; Siegel, G.; Roundy, R.; Raikh, M.; Tiwari, A. *J. Appl. Phys.* **2015**, 117, 083905(1)-(6).
24. Wang, Z.; Tang, C.; Sachs, R.; Barlas, Y.; Shi, J. *Phys. Rev. Lett.* **2015**, 114, 016603(1)-(5).
25. Niimi, Y.; Suzuki, H.; Kawanishi, Y.; Omori, Y.; Valet, T.; Fert, A.; Otani, Y. *Phys. Rev. B* **2014**, 89, 054401(1)-(10).
26. Sinitsyn, N. A. *J. Phys.: Condens. Matter* **2008**, 20, 023201(1)-(17).
27. Tse, W.-K.; Das Sarma, S. *Phys. Rev. Lett.* **2006**, 96, 056601(1)-(4).
28. Guo, G. Y.; Yao, Y.; Niu, Q. *Phys. Rev. Lett.* **2005**, 94, 226601(1)-(4).
29. Yao, Y.; Fang, Z. *Phys. Rev. Lett.* **2005**, 95, 156601(1)-(4).

**Table 6.1 Temperature dependence of the inverse spin Hall effect in ZnO thin films deposited under 0.1 mTorr.** Values of the spin Hall angle, spin Hall conductivity, and spin Hall resistivity for ZnO thin films deposited under 0.1 mTorr of O<sub>2</sub>.

Temperature (K)	Spin Hall Angle (%)	Spin Hall Conductivity (S/cm)	Spin Hall Resistivity ( $\Omega$ -cm)
300	1.65	3.18	$8.55 \times 10^{-5}$
275	1.48	2.84	$7.66 \times 10^{-5}$
250	1.47	2.83	$7.61 \times 10^{-5}$
225	1.34	2.55	$7.02 \times 10^{-5}$
200	1.24	2.34	$6.55 \times 10^{-5}$
175	1.25	2.33	$6.71 \times 10^{-5}$
150	1.16	2.13	$6.28 \times 10^{-5}$
125	1.07	1.92	$5.91 \times 10^{-5}$
100	1.02	1.79	$5.84 \times 10^{-5}$
75	1.08	1.85	$6.27 \times 10^{-5}$
50	1.14	1.89	$6.85 \times 10^{-5}$

**Table 6.2 Temperature dependence of the inverse spin Hall effect in ZnO thin films deposited under 1 mTorr.** Values of the spin Hall angle, spin Hall conductivity, and spin Hall resistivity for ZnO thin films deposited under 1 mTorr of O<sub>2</sub>.

Temperature (K)	Spin Hall Angle (%)	Spin Hall Conductivity (S/cm)	Spin Hall Resistivity ( $\Omega$ -cm)
300	3.33	0.917	$1.21 \times 10^{-3}$
275	3.39	0.931	$1.23 \times 10^{-3}$
250	3.89	1.07	$1.41 \times 10^{-3}$
225	3.93	1.08	$1.43 \times 10^{-3}$
200	2.62	0.715	$9.61 \times 10^{-4}$
175	3.21	0.863	$1.20 \times 10^{-3}$
150	2.32	0.610	$8.83 \times 10^{-4}$
125	2.44	0.617	$9.64 \times 10^{-4}$
100	1.65	0.391	$6.96 \times 10^{-4}$
75	1.31	0.282	$6.07 \times 10^{-4}$
50	1.38	0.152	$4.29 \times 10^{-4}$

**Table 6.3 Temperature dependence of the inverse spin Hall effect in ZnO thin films deposited under 10 mTorr.** Values of the spin Hall angle, spin Hall conductivity, and spin Hall resistivity for ZnO thin films deposited under 10 mTorr of O<sub>2</sub>.

Temperature (K)	Spin Hall Angle (%)	Spin Hall Conductivity (S/cm)	Spin Hall Resistivity ( $\Omega$ -cm)
300	9.34	3.70	$2.34 \times 10^{-3}$
275	9.13	3.61	$2.29 \times 10^{-3}$
250	8.86	3.47	$2.24 \times 10^{-3}$
225	8.09	3.14	$2.07 \times 10^{-3}$
200	7.08	2.73	$1.82 \times 10^{-3}$
175	6.40	2.46	$1.66 \times 10^{-3}$
150	6.12	2.34	$1.59 \times 10^{-3}$
125	6.11	2.22	$1.67 \times 10^{-3}$
100	6.47	2.36	$1.77 \times 10^{-3}$
75	5.53	2.01	$1.52 \times 10^{-3}$
50	4.46	1.59	$1.25 \times 10^{-3}$

**Table 6.4 Composition dependence of the intrinsic and extrinsic contributions to the spin-orbit coupling in ZnO.** Table summarizing the intrinsic and extrinsic (due to impurities only) spin-orbit coupling contributions to the spin Hall conductivity determined according to the fits in Figure 6.9 for the 0.1, 1, and 10 mTorr samples.

Sample Name	Intrinsic SHC	Extrinsic SHC (due to impurity skew-scattering)
0.1 mTorr	-1.5 S/cm	3.5 S/cm
1 mTorr	-0.59 S/cm	0.97 S /cm
10 mTorr	-5.4 S/cm	7.6 S/cm

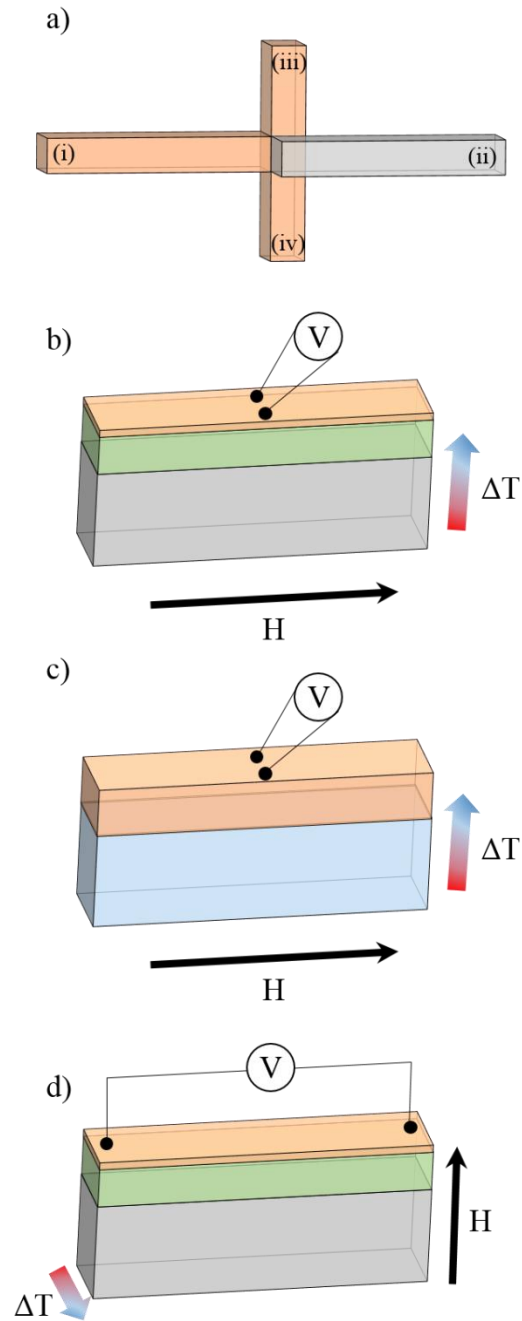


**Figure 6.1 Device arrangements to test for the ISHE, the SSE, the Nernst effect, and the anomalous Nernst effect in ZnO.** Schematics of the testing arrangements for a) the ISHE via electrical spin injection, b) the SSE – thermal spin injection, c) the Nernst effect, and d) the proximity-induced anomalous Nernst effect. In these diagrams, ZnO is shown as orange, YIG is shown as green, the GGG substrate is shown in gray, and the sapphire substrate is shown in blue. In Figure 6.1a, the current was injected from (ii) to (i), and the voltage was measured from (iv) to (iii).



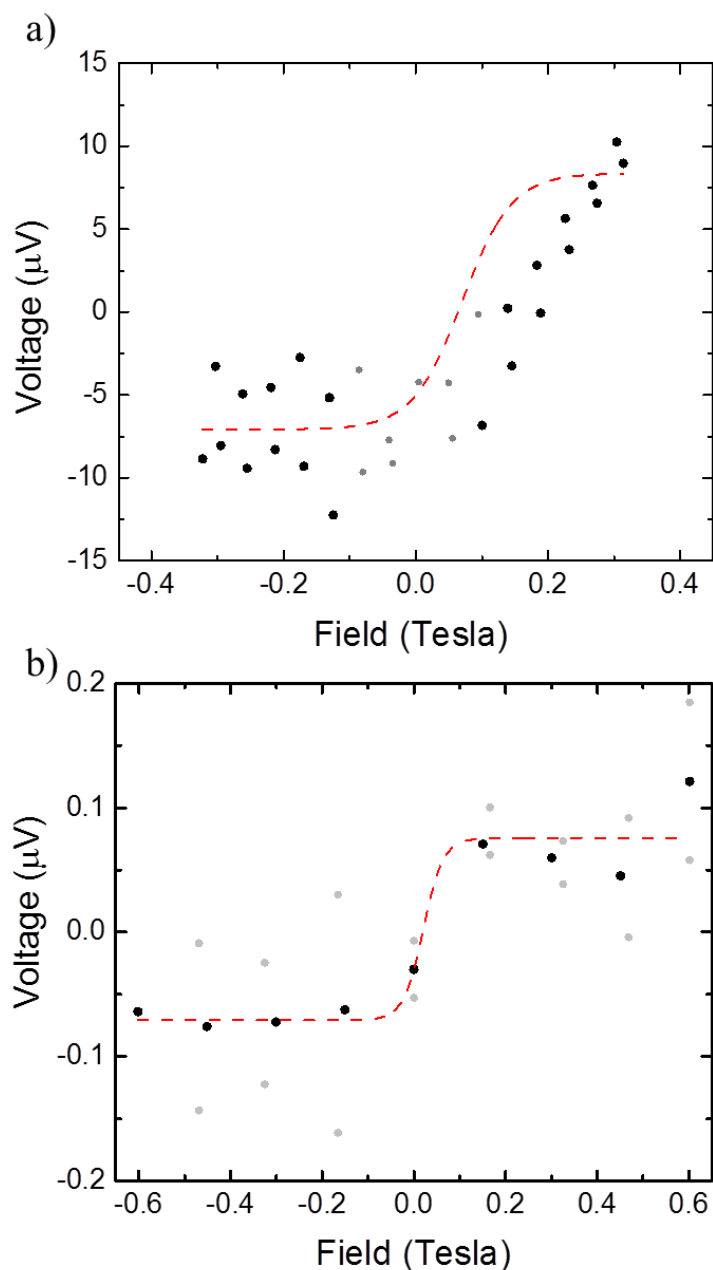


**Figure 6.2 Voltage signal generated due to electrical and thermal spin injection in ZnO.** a) The ISHE response for the 1 mTorr ZnO sample measured via electrical spin injection testing. b) The ISHE response for the 10 mTorr ZnO/YIG sample, generated via the spin Seebeck effect. For both sets of data, the anticipated behavior is a Boltzmann-type curve, which is shown as a red, dashed curve for each set of data.

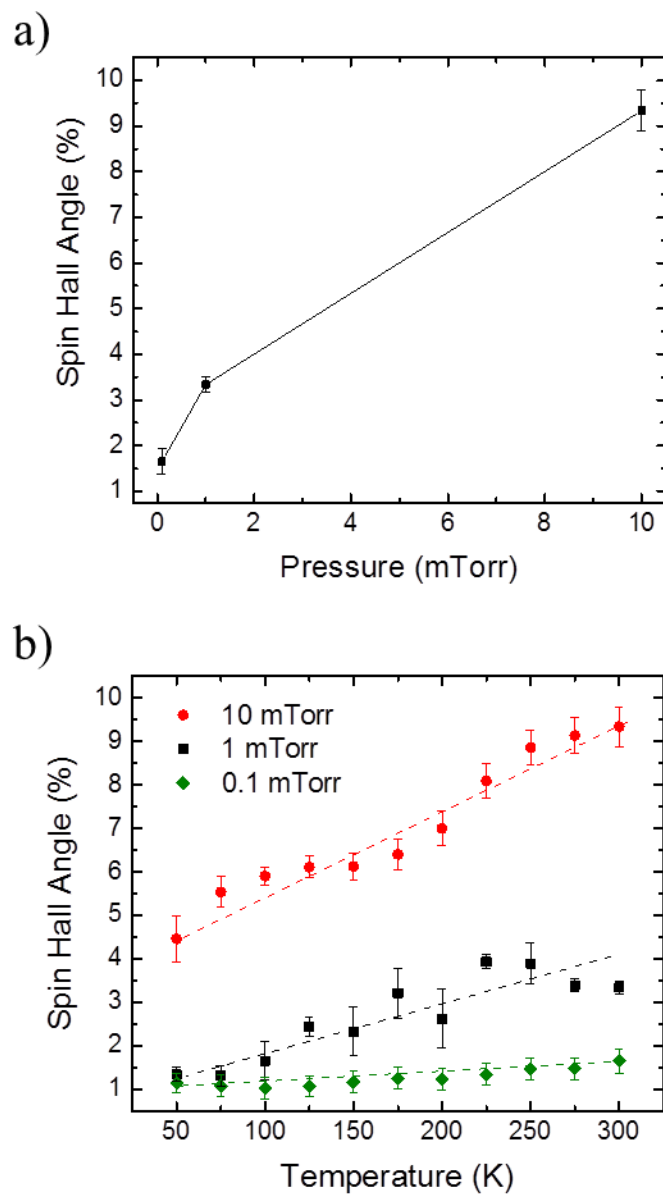


**Figure 6.3 The composition and temperature dependence of the spin Hall angle in ZnO.** The spin Hall angle (in %) dependence on a) oxygen pressure during deposition and b) temperature.

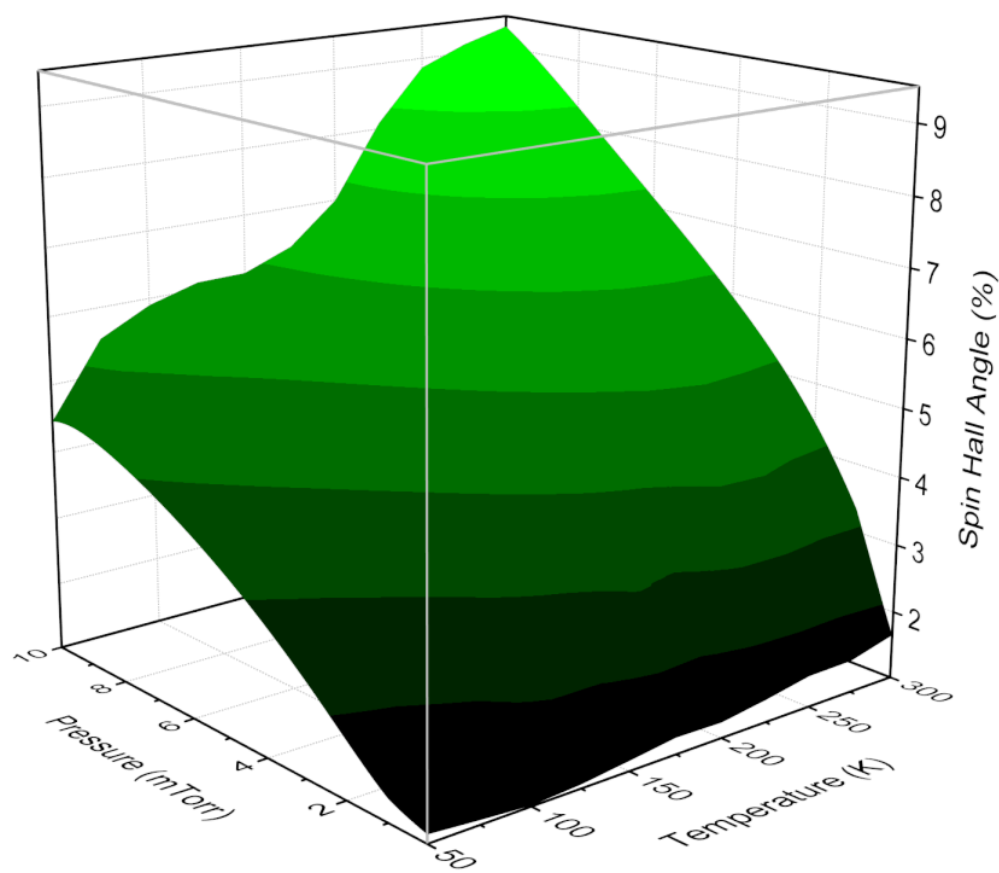


**Figure 6.4 3D contour plot showing spin Hall angle versus temperature and composition.** A 3D contour plot of the spin Hall angle dependence on oxygen pressure and temperature based on the data at 0.1, 1, and 10 mTorr for temperatures between 50 and 300 K. In this case, the brighter color indicates the larger spin Hall angle.

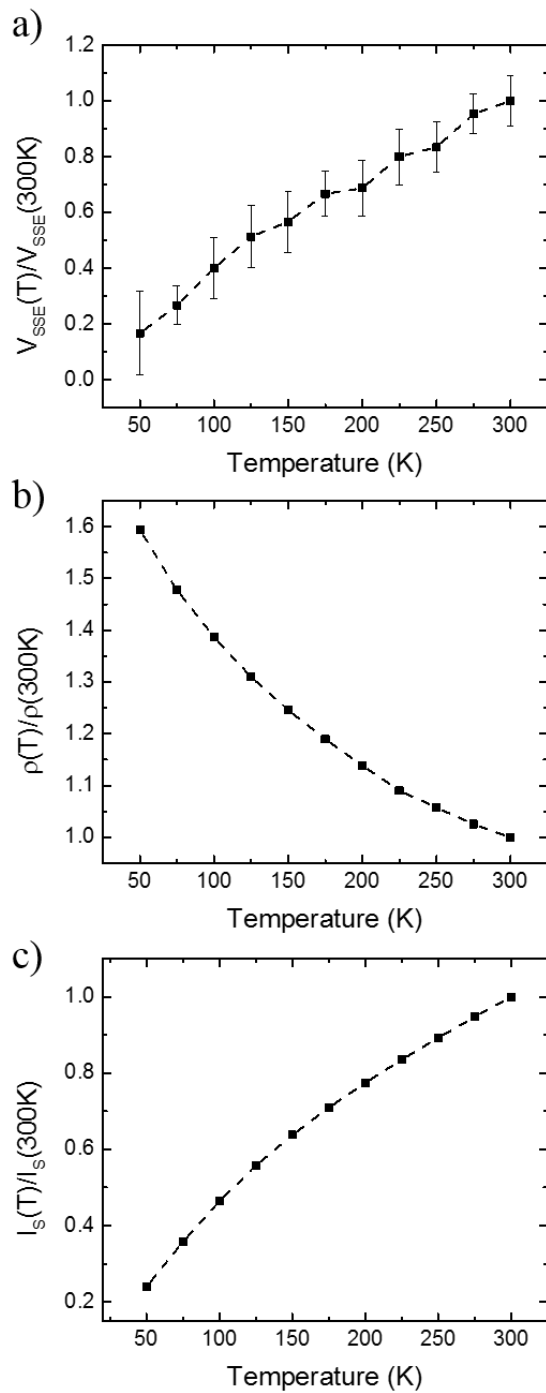


**Figure 6.5 The relative spin Seebeck voltage, electrical resistivity measured, and magnon-injected spin current.** Spin Seebeck effect results showing a) the measured, relative  $V_{SSE}$  versus temperature, b) the measured, relative electrical resistivity versus temperature, and c) the calculated, relative spin current,  $I_s$ , determined via magnon transport theory.

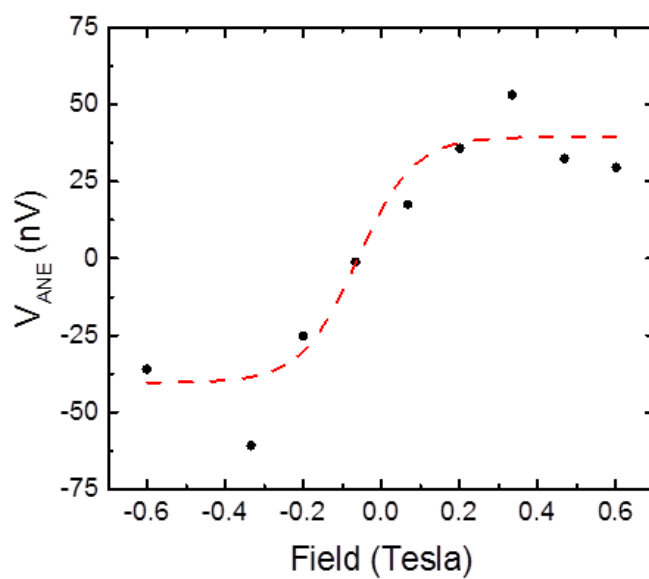


**Figure 6.6 Nernst effect and anomalous Nernst effect signals.** Voltage signal at 300 K due to the proximity-induced anomalous Nernst effect (denoted  $V_{ANE}$ ) – showing a  $\sim 40$ -50 nV signal.

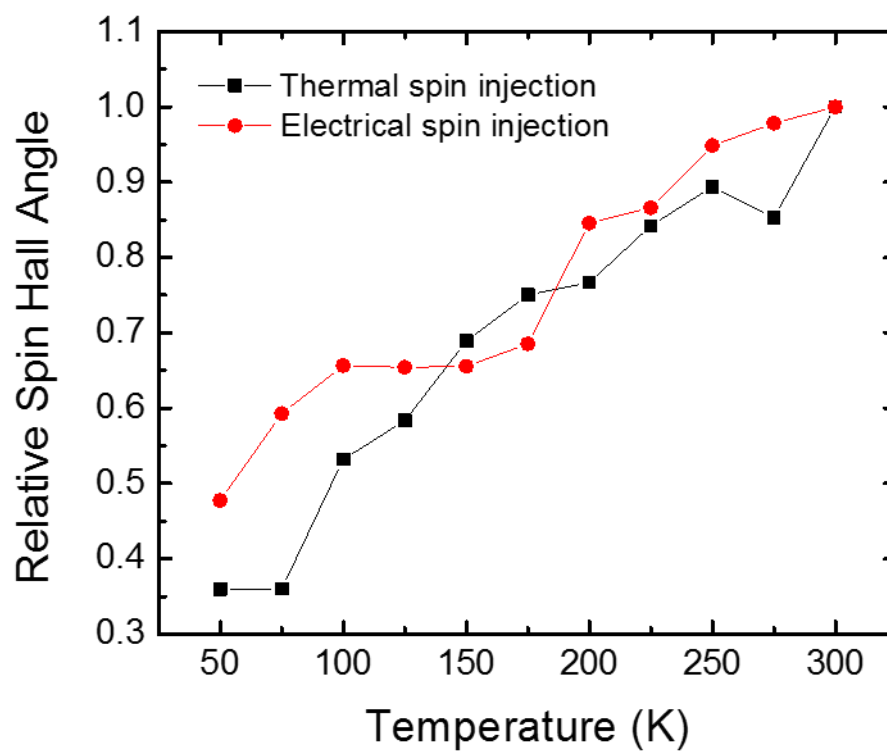


**Figure 6.7 The relative spin Hall angle measured via electrical and thermal spin injection.** A comparison of the relative spin Hall angle calculated from electrical spin injection experiments and thermal spin injection experiments for ZnO thin films deposited under 10 mTorr O<sub>2</sub>.

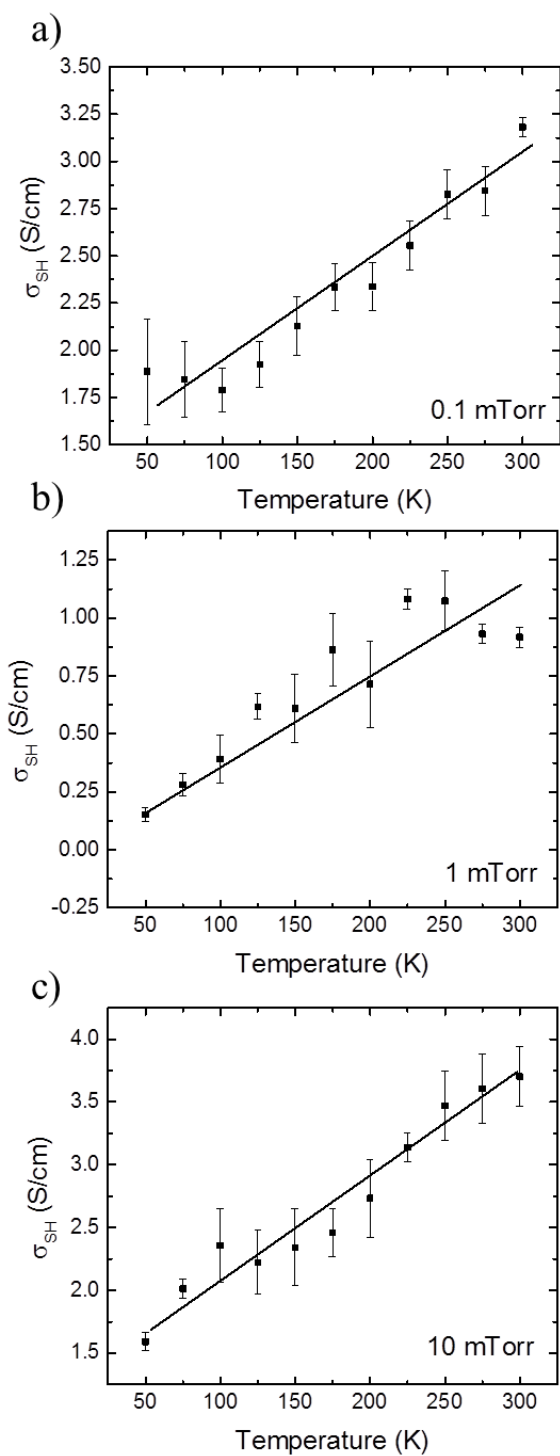


**Figure 6.8 Spin Hall conductivity versus temperature for all compositions.** Spin hall conductivity versus temperature the a) 0.1 mTorr, b) 1 mTorr, and c) the 10 mTorr samples.

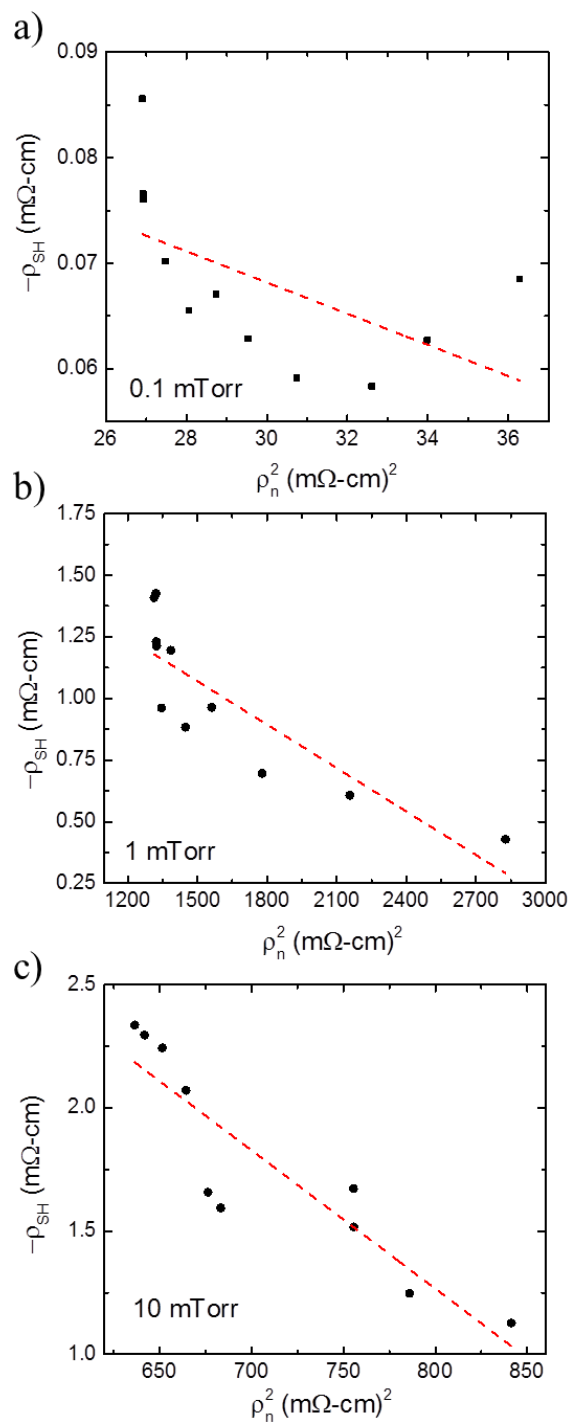


**Figure 6.9 Spin Hall resistivity versus electrical resistivity squared for all compositions.** Negative spin Hall resistivity versus electrical resistivity squared for the a) 0.1 mTorr, b) 1 mTorr, and c) the 10 mTorr samples. A linear fit to eq. (6.14) is shown for each of the curves.



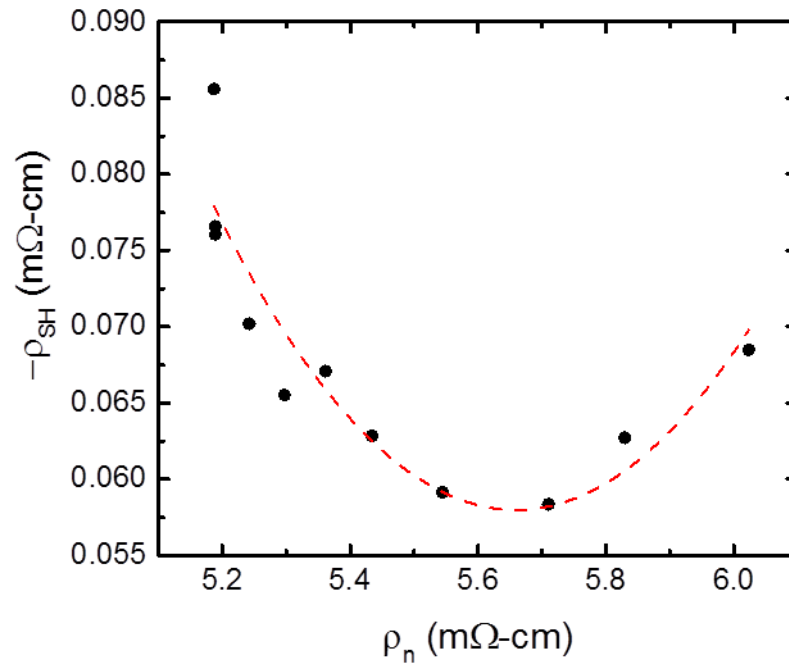


**Figure 6.10 Spin hall resistivity versus electrical resistivity: A fit of the 0.1 mTorr data.** Negative spin Hall resistivity versus electrical resistivity for the 0.1 mTorr sample. The fit equation is a quadratic depending on the respective intrinsic and extrinsic (due to impurity and phonon skew-scattering) SOC – according to eq. (6.15).

## CHAPTER 7

### FUTURE WORK AND CONCLUSION

This section summarizes the results presented herein and offers an outlook on future research in the field. In the future work section, a method for testing spin injection via a dilute magnetic dielectric,  $\text{CeO}_2$ : Co layer is proposed. An additional study on the spin detection capabilities of ZnO is discussed, specifically addressing how modifications to the structure may affect the spin Hall angle and spin Hall conductivity properties of ZnO.

#### 7.1 Future Work

Future work in the field of spintronic research should be focused on the fabrication of spin-based devices for next-generation technologies. However, the development and implementation of spintronics relies on enhancing and optimizing spin-based effects in a variety of materials and using these materials to fulfill spintronic device requirements. In the sections below, two new research topics will be discussed: the implementation of dilute magnetic dielectrics as spin-filter tunnel junctions for spin-polarized injection and the optimization and study of the structural dependence of the ISHE in ZnO.

### 7.1.1 Spin Injection via a Dilute Magnetic Dielectric Tunnel Barrier

Following the work presented in Chapter 3, which distinguished between intrinsic and extrinsic doping by examining the magnetic moment of the material, we propose a dilute magnetic dielectric tunnel barrier for spin filtering. As was introduced, theory postulates that in this kind of material, the energy requirements for tunneling will be spin-dependent, and thus injecting an unpolarized current into the tunnel barrier will result in a tunneled, spin-polarized current being passed into the channel.<sup>1</sup> Thus, spin-polarized injection should be possible without the use of a ferromagnetic injector contact. For testing this theory, a 3T Hanle device has been used according to Figure 7.1. In this arrangement, an aluminum contact is used to inject electrons into a Si channel through a  $\text{CeO}_2$ : Co tunnel barrier. In this tunnel barrier, the Co doping is intrinsic in nature. To probe the Hanle response, and thus the injected spin current polarization, an external, out-of-plane magnetic field is applied across the sample and the resulting voltage is measured from the Al/ $\text{CeO}_2$ : Co contact and a third contact along the length of the device, as shown in Figure 7.1. The resulting Hanle curve is a Lorentzian, with the width of the curve being proportional to spin lifetime in Si. Because the spin lifetime behavior has been well-studied in Si via the 3T Hanle effect,<sup>2</sup> the data obtained via traditional injection from a ferromagnetic electrode can be directly compared to the data obtained by injecting through a DMD tunnel barrier. Through this comparison, because the spin lifetime in Si is the same in both devices, the polarization resulting from DMD tunnel barrier usage can be obtained.

Similarly to electrical injection and detection, spin-polarized currents can also be measured optically. In order to examine the spin filter properties of  $\text{CeO}_2$ :Co, the optical

Hanle effect can be studied in an LED/CeO<sub>2</sub>:Co structure. In this device, the LED is a thin film, multilayered GaAs-based quantum well LED. When a thin film of CeO<sub>2</sub>:Co is deposited atop the LED and current is injected across the CeO<sub>2</sub>:Co, the resulting output light will be circularly polarized, proportional to the degree of spin-polarization resulting from tunneling through the DMD barrier. This method will give further support of the potential for DMDs as spin-filtering tunnel barriers in spintronic devices.

### 7.1.2 Structural Dependence of the Spin Hall Angle in ZnO

Similar to the previously reported temperature and compositional dependencies of the spin Hall angle (SHA), and consequently the spin-orbit coupling (SOC) (Chapters 5 and 6), the structural dependence of the SHA has also been investigated. Because SOC is highly dependent on the structural asymmetry in the material, it is expected that modulation of strain and structure can be used to either enhance or hinder the ISHE in ZnO films.<sup>3,4</sup> For this testing, ZnO thin films were deposited under 10 mTorr of O<sub>2</sub> on R-cut sapphire. These results were compared to the results of Chapter 6 for the 10 mTorr ZnO sample deposited on C-cut sapphire. The ISHE response in these R-axis aligned films was probed by testing according to the method outlined in Chapters 5 and 6.

The results for these R-axis-aligned films showed a lower SHA at room temperature for R-axis aligned ZnO as compared to C-axis aligned ZnO, ~7.8% compared to ~9.6% for R- and C-axis, respectively. Additionally, the temperature dependence of the SHA for the 10 mTorr R-axis-aligned ZnO showed the same trend as the C-axis-deposited 10 mTorr sample (Figure 7.2a), indicating that both have a similar mechanism of SOC. Indeed, by fitting the negative spin Hall resistivity versus electrical

resistivity squared to a linear expression according to eq. (6.14), shown in Figure 7.2b, the extrinsic spin Hall conductivity due to impurities was found to be  $\sim 2.5\times$  larger than the intrinsic contribution, which indicates that the R-axis-aligned ZnO was slightly more defective than the C-axis-aligned ZnO when deposited at 10 mTorr. Future studies on the SOC in ZnO as a function of structure can be used to quantify the degree of the intrinsic and extrinsic contributions and can help determine how to modulate these terms via strain and structure modulations.

## 7.2 Conclusion

Although there has yet to be a traditional spin-FET that can be implemented into standard electronic devices, this dissertation has outlined many advances made in spintronic research. In the field of spin injection, research into dilute magnetic dielectric materials has shown that the nature of the magnetic behavior is directly dependent on whether the dopant substitutes directly into the lattice or if the dopant atoms exist as clusters. Specifically, if the magnetic atoms exist purely as clusters, the magnetic moment of the DMD is given by the magnetic moment of the magnetic atoms present. If a mixture of substitutional doping and clustering exists, then the magnetic moment is the weighted sum of the magnetic momentum due to the clustered atoms as well as the magnetic moment due to the substitutional magnetic atoms. This allows us to distinguish between the clustered, substitutional, and mixed cases, thereby allowing us to know if a DMD is showing purely intrinsic ferromagnetism.

Based on 4T Hanle measurements in ZnO, it has been shown that the spin lifetime in ZnO is relatively long,  $\sim 150$  ps, which gives a spin diffusion length of  $\sim 200$  nm. Also,

the spin relaxation in ZnO was shown to be dependent on only Dyakonov-Perel spin relaxation mechanics, as dictated by Fermi-Dirac statistics. Additional investigations into the spin detection properties of ZnO, using the inverse spin Hall effect (ISHE), have shown that ZnO possesses a relatively large spin Hall angle, up to ~10% when deposited by PLD under 10 mTorr O<sub>2</sub>. This value was shown to vary with composition and temperature, thereby allowing for the tunability of the detection properties via deposition modifications. This relatively large spin Hall angle occurred as a result of extrinsic spin-orbit coupling in ZnO. These works have shown the potential for ZnO as either a spin transport channel or a spin detector in spintronic devices. Through this research, the potential for the efficient injection, transport, and detection of spin-polarized carriers has increased drastically. It is with developments like these that the future fabrication of a traditional spin-FET will become possible.

### 7.3 References

1. Slusser, P.; Kumar, D.; Tiwari, A. *JOM* **2011**, *63*, 25-28.
2. Gray, N. W.; Tiwari, A. *Appl. Phys. Lett.* **2011**, *98*, 102112(1)-(3).
3. Rashba, E.I. *Sov. Phys. Solid State* **1960**, *2*, 1109-1122.
4. Bychkov, Y. A.; Rashba, E. I. *J. Phys. C: Solid State Phys.* **1984**, *17*, 6034-6045.

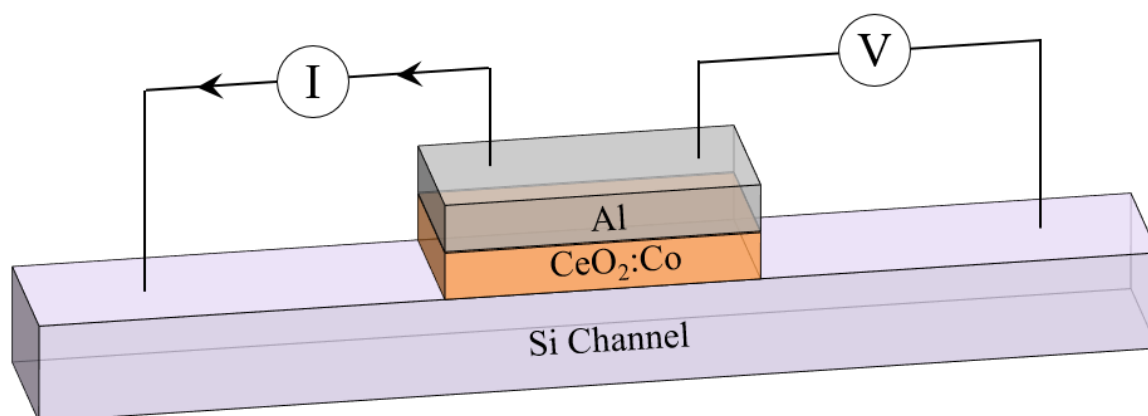


**Figure 7.1 3T Hanle Device with a CeO<sub>2</sub>:Co DMD tunnel barrier and Al injector.** Schematic illustrating Hanle testing using a CeO<sub>2</sub>:Co tunnel barrier to inject spin-polarized carriers. In this device, unpolarized electrons are injected from the Al into the Si channel. Upon tunneling through the DMD, spin filtering will occur and the current will now be spin-polarized. The spin lifetime and Hanle curves will then be measured in the Si channel by measuring the local voltage difference between the Al contact and a relatively far away point on the Si channel.



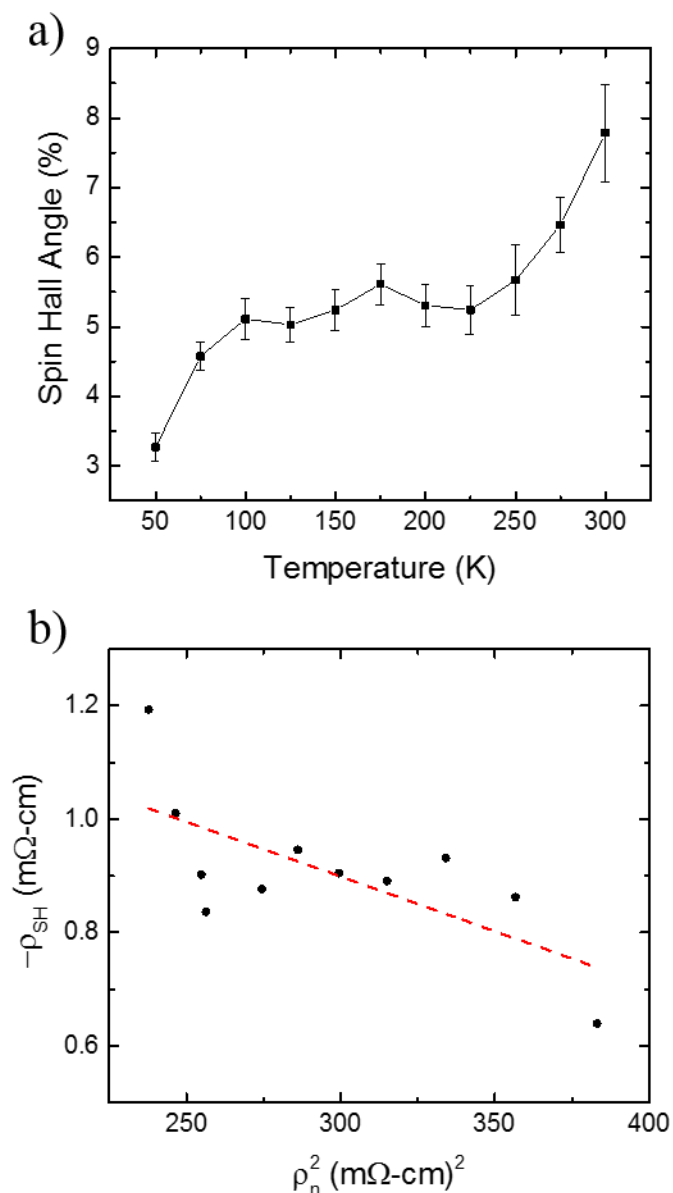


**Figure 7.2 R-axis ZnO ISHE results.** Graph showing the spin Hall angle in ZnO as a function of temperature for ZnO deposited under 10 mTorr O<sub>2</sub> on R-cut sapphire. These data show that the spin Hall angle is dependent on the structure of the ZnO and is lower for ZnO deposited on R-cut sapphire than films deposited on C-cut sapphire. Additionally, based on the spin Hall resistivity and electrical resistivity behavior, Figure 7.2b, it is theorized that a phonon contribution to the total extrinsic spin Hall conductivity is present, as the linear fit is not adequate to describe the behavior of the sample at all temperatures.

## CHAPTER 8

### LIST OF PUBLICATIONS

#### Publication Statistics:

Number of First-Authored Journal Articles: 6

Number of Total Journal Articles: 15

#### Published Journal Articles:

**M. C. Prestgard**, G. Siegel, R. C. Roundy, M. E. Raikh and A. Tiwari, "Temperature dependence of the spin relaxation in highly degenerate ZnO thin films," *J. Appl. Phys.* **117**, 083905 (2015).

**M. C. Prestgard** and A. Tiwari, "Observation of the inverse spin Hall effect in ZnO thin films: an all-electrical approach to spin injection and detection," *Appl. Phys. Lett.* **104**, 122402 (2014).

**M. C. Prestgard**, G. Siegel, and A. Tiwari, "Oxides for Spintronics: A review of engineered materials for spin injection," *Adv. Mater. Lett.* **5**, 242 (2014).

**M. C. Prestgard**, G. Siegel, Q. Ma, and A. Tiwari, "Magnetic characteristics of phase separated CeO<sub>2</sub>: Co thin films," *Appl. Phys. Lett.* **103**, 102409 (2013).

**M. C. Prestgard** and A. Tiwari, "Kinetically Stable Glassy Phase Formation in Neodymium Nickelate Thin Films as Evidenced by Hall Effect and Electrical Resistivity Measurements," *J. Mater. Res.* **28**, 1699 (2013).

**M. C. Prestgard** and A. Tiwari, "Evidence of Kinetically Stable Glassy Phase Formation in Ultrathin NdNiO<sub>3</sub> Films," *Jpn. J. Appl. Phys.*, **51**, 11PG08 (2012).

Z. Yue, **M. C. Prestgard**, A. Tiwari, and M. E. Raikh, "Resonant magneto-tunneling between normal and ferromagnetic electrodes in relation to the three-terminal spin transport," *Phys. Rev. B* **91**, 195316 (2015).

G. Siegel, **M. C. Prestgard**, H. Yang, and A. Tiwari, "Spin Current Response in Bi-YIG/Pt Thin Film Hetero-structures Induced by Gamma Radiation," *IEEE. Elect. Dev. Lett.* **36**, 853 (2015).

G. Siegel, Y. P. Venkata Subbaiah, **M. C. Prestgard**, and A. Tiwari, "Growth of Centimeter-scale atomically thin MoS<sub>2</sub> films by pulsed laser deposition," *APL Mater.* **3**, 056103 (2015).

N. W. Gray, **M. C. Prestgard**, and A. Tiwari, "Tb<sub>2</sub>O<sub>3</sub> thin films: An alternative candidate for high-k dielectric applications," *Appl. Phys. Lett.* **105**, 222903 (2014).

R. C. Roundy, **M. C. Prestgard**, A. Tiwari, and M. E. Raikh "The shape of the Hanle curve in spin-transport structures in the presence of AC drive," *Phys. Rev. B* **90**, 205203 (2014).

R. C. Roundy, **M. C. Prestgard**, A. Tiwari and M. E. Raikh "Manifestation of two-channel nonlocal spin transport in the shapes of the Hanle curves," *Phys. Rev. B* **90**, 115206 (2014).

G. Siegel, **M. C. Prestgard**, S. Teng, and A. Tiwari, "Robust longitudinal spin-Seebeck effect in Bi-YIG thin films," *Sci. Rep.* **4**, 4429 (2014).

K. Tian, **M. C. Prestgard**, and Ashutosh Tiwari, "A review of recent advances in nonenzymatic glucose sensors," *Mater. Sci. & Engineer. C* **41**, 100 (2014).

S. Teng, G. Siegel, **M. C. Prestgard**, W. Wang, and A. Tiwari, "Synthesis and characterization of copper-infiltrated carbonized wood monoliths for supercapacitor electrodes," *Electrochim. Acta* **161**, 343 (2015).

#### Journal Articles Currently Under Preparation:

**M. C. Prestgard** and A. Tiwari, "Proximity induced ferromagnetism in ZnO"

**M. C. Prestgard** and A. Tiwari, "Temperature and Oxygen Pressure Dependence of the Spin Hall Angle in ZnO Thin Films"

## APPENDIX A

### EXPERIMENTAL DESIGN AND TESTING OF THE 4T HANLE DEVICE

In order to perform the nonlocal Hanle experiments as described in Chapter 4, 4T Hanle devices were fabricated, the steps of which are shown in Figure A.1 of this appendix. First, ZnO thin films were deposited using a PLD technique. These films were deposited on sapphire substrates at a temperature of 700°C, under  $10^{-4}$  Torr of oxygen at a laser repetition rate of 10 Hz. To deposit films that were 200 nm thick, the ZnO target was ablated for 8,000 pulses. The desired, relatively narrow ZnO channel ( $\sim 2$  mm) was deposited using a shadow mask. The deposition rate (that is, the number of angstroms of ZnO deposited per laser pulse) was determined by depositing a trial ZnO thin film on sapphire and using a shadowmask to cover a portion of the substrate. Using a P-10 Tencor profilometer, the thickness of the ZnO thin film for 8,000 laser pulses was determined by performing a line scan from the masked portion (blank sapphire) to the ZnO thin film. These measurements, performed at several areas along the masked/ZnO interface, were used to determine the average thickness of  $\sim 200$  nm (with an error of about 10 nm).

Following the deposition of the ZnO thin films, an MgO tunnel barrier was deposited, also using PLD. These films were deposited at room temperature, under

vacuum ( $10^{-6}$  Torr) at a repetition rate of 1 Hz. For these films, 30 laser pulses gave films  $\sim 3 - 5$  nm in thickness. These MgO tunnel barriers were also deposited in the narrow channel arrangement, directly atop the ZnO, using a shadow mask as previously described. For this Hanle device, as well as the NiFe spin injector contacts in Chapters 5 and 6, an MgO tunnel barrier was used to enhance spin injection through use of tunneling, as compared to a direct metal-semiconductor junction (which is inefficient due to an impedance mismatch between the layers, as shown in Chapter 1).<sup>1</sup>

The NiFe contact pads were then deposited in a 3T arrangement using e-beam evaporation. For this, a positive photoresist (Shipley 1813) was first applied to the top of the MgO/ZnO/Sapphire samples. This photoresist was then patterned using a shadowmask, which was aligned on the substrate using an OAI 206 mask aligner. The shadowmask was of the 3T Hanle arrangement. Following exposure of the photoresist for 45 seconds, the resist was developed for 60 seconds to remove the exposed portions (the 3T contact pads) of the resist. After this,  $\sim 20$ -25 nm of NiFe was deposited over the entire sample using a Denton SJ20C e-beam evaporator. Using acetone, the remaining photoresist was removed. Because NiFe was deposited both directly on the sample (where the exposure process left openings in the photoresist) as well as on the photoresist on the surface, removal of the photoresist using acetone left only the as-deposited NiFe contact pads. Then using a dual-beam SEM/FIB, the centermost NiFe contact was cut in half.

Following fabrication of the 4T Hanle effect device, it was tested according to the method described in Chapter 4. In this testing, current was passed between contacts 1 and 2 using a Keithley current source, and voltage was measured between contacts 3 and 4

using a Keithley nanovoltmeter. The NiFe contacts were first polarized as shown in Figure A.2 by passing a magnetic field of ~5 kG for 30 minutes. For testing the Hanle response, an out-of-plane external magnetic field was applied through the thickness of the NiFe contacts, as shown in Figure A2. Although NiFe generally has a relatively low coercivity (values < 5 G has been reported<sup>2</sup>), values up to 500 G have been reported in relatively thin channels (< 1  $\mu\text{m}$ ).<sup>3,4</sup> Because of this, and given the large difference in sample dimension in the polarization direction (~2-3 mm) and the out-of-plane field application direction (~20 nm), the polarization should be relatively well retained during the device testing.

For fitting the as-measured Hanle curves, the diffusion coefficient was calculated according to Fermi Dirac statistics. These statistics were deemed necessary in order to account for the large carrier concentration ( $n \approx 3.5 \times 10^{19} \text{ cm}^{-3}$  at 300 K) and the large Fermi energy (~ 116 meV at 300 K), as calculated in Chapter 5. However, calculation of the Fermi energy in this system was done according to eq. 4.1, which applies for metals and can only provide a good approximation of the values for Fermi energy in the case that the semiconductor is highly degenerate. In order to confirm this assumption, the Fermi energy has been calculated based on the effective density of states in the conduction band for our ZnO according to the method outlined below. Calculation of the Fermi energy generally follows the form (eq. A.1)<sup>5</sup>:

$$E_F = E_C - k_B T \cdot \ln \left( \frac{N_C}{n} \right) \quad (\text{A.1})$$

In this equation,  $E_C$  is the conduction band energy,  $n$  is the carrier concentration, and  $N_C$

is the conduction band effective density of states, given by A.2:

$$N_C = 2 \left( \frac{2\pi m^* k_B T}{h^2} \right)^{3/2} \quad (\text{A.2})$$

However, eq. A.1 is for nondegenerate semiconductors. For the degenerate case ( $n \geq N_C$ ) Fermi-Dirac statistics must be used. Calculating  $N_C$  for ZnO and comparing that to our measured values of  $n$ , we see that  $\sim N_C \approx 4.1 \times 10^{18} \text{ cm}^{-3}$ , which is an order of magnitude smaller than our reported values of  $n$  ( $\sim 10^{19} \text{ cm}^{-3}$ ). Because  $n > N_C$ , eq. A.1 must be adapted for Fermi-Dirac statistics, and takes the form:<sup>5</sup>

$$E_F \approx E_C + \left[ k_B T \cdot \ln \left( \frac{n}{N_C} \right) + 2^{-3/2} \cdot k_B T \cdot \left( \frac{n}{N_C} \right) \right]$$

Using this relation, the Fermi-energy was calculated to be  $\sim 3.5$  eV, or approximately 130 meV above the conduction band edge. Comparing this to the values, previously reported in Chapter 5, of  $\sim 116$  meV above the conduction band edge, both equations show fairly good agreement. Also, since our Fermi energy lies within the conduction band, it is expected that the previously used equation for a metallic system should give a good approximation of the system behavior.

### References

1. Salis, G.; Wang, R.; Jiang, X.; Shelby, R. M.; Parkin, S. S. P.; Bank, S. R.; Harris, J. S. *Appl. Phys. Lett.* **2005**, 87, 262503(1)-(3)
2. Kockar, H.; Alper, M.; Kuru, H.; Meyden, T.; *J. Magnetism and Magnetic Mater.* **2006**, 304, e736-e738.
3. Tang, H. X.; Monzon, F. G.; Jedema, F. J.; Filip, A. T.; van Wees, B. J.; Roukes, M. L. Spin Injection and Transport. In *Semiconductor Spintronics and Quantum Computation*; Awschalom, D. D.; Loss, D.; Samarth, N. Eds.; Springer: Berlin Heidelberg 2002; Ch. 2, pp. 51.
4. Michel, R. P.; Chaiken, A.; Kim, Y.; Johnson, L. E. *IEEE. Trans. Magn.* **1996**, 32, 4651-4653.
5. Sze, S. M.; Ng, K. K. *Physics of Semiconductor Devices*: John Wiley & Sons: Hoboken 2007; pp. 18-19.



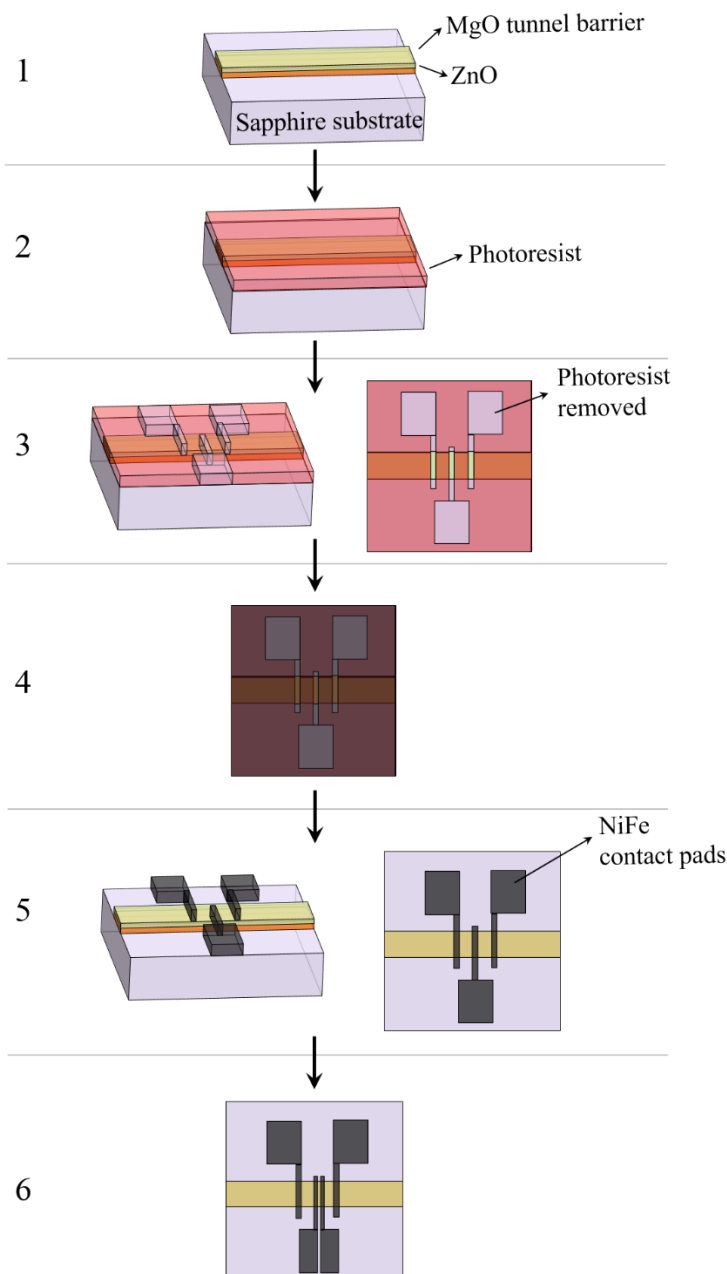


**Figure A.1 Procedure for fabricating the 4T Hanle devices.** Steps detailing the process by which the 4T Hanle devices were fabricated. In step 1, the ZnO (orange) and MgO (green) are deposited by PLD on the sapphire (purple) substrate. In step 2, a layer of photoresist is applied over the entire surface. Step 3 details the patterning of the photoresist, in which photoresist is removed in the 3T geometry. In step 4, NiFe is deposited over the entire surface, both on the photoresist as well as in the exposed channels. In step 5 the photoresist (and the NiFe on top of that) is removed using acetone, leaving on the NiFe contacts. The final step, step 6, shows the cutting of the centermost contact into two contacts via FIB.

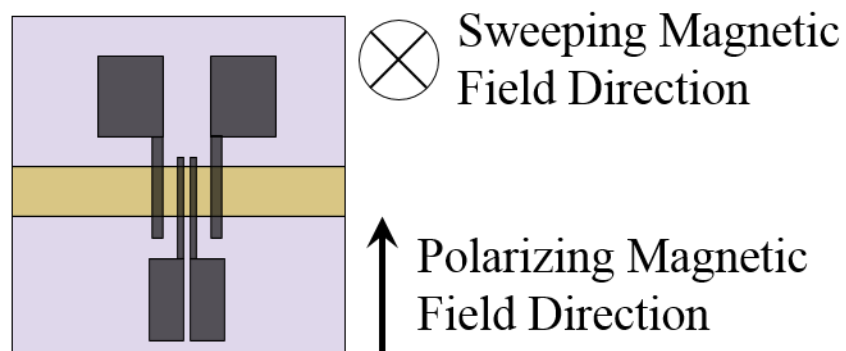


**Figure A.2 Hanle device testing arrangement.** Device schematic illustrating the direction of the magnetic field first applied to polarized carriers in the NiFe contacts, and the direction of the sweeping magnetic field which was used to probe the Hanle response.

## APPENDIX B

### DEVICE DESIGN FOR ALL-ELECTRICAL INVERSE

#### SPIN HALL EFFECT EXPERIMENTS

The following method was used to fabricate devices for measuring the room temperature ISHE in ZnO thin films, as reported in Chapter 5. The thin films of ZnO were deposited on sapphire substrates using PLD. An MgO tunnel barrier layer was then deposited atop the ZnO films. The ZnO/MgO were then patterned using a negative resist (that is, the resist was patterned in the desired “T” structure, as shown in Figure B.1). Using a dilute acid mixture (200 mL H<sub>2</sub>O: 1.5 mL H<sub>3</sub>PO<sub>4</sub>: 0.1 mL HCl), the unmasked ZnO/MgO was etched for 60 seconds until entirely removed. Acetone was then used to remove the negative resist and uncover the resulting ZnO/MgO structure. NiFe was then deposited in a thin strip using the method outline in the supplement to Chapter 4, where positive photoresist was used to make the desired geometry in which to deposit NiFe. The overall device arrangement with dimensions is shown in Figure B.2.

For testing, a magnetic field was applied in-plane, along the length of the NiFe strip, in order to magnetically polarize the spins in the NiFe film. The polarized carriers were then injected into the ZnO by applying a current between the ZnO and NiFe according to Figure 5.3. As the spin-polarized charge current is injected into the ZnO, a voltage develops in the transverse ZnO channel due to the spin-orbit coupling.

However, because this is a local arrangement, and thus the voltage signal is complicated by additional effects (such as an offset voltage bias and a magnetoresistance background), simply measuring the ISHE voltage is a challenge. In order to probe the ISHE response, we have swept the externally applied magnetic field in order to sweep the polarization of the injected carriers. This allows us to see a response in the ZnO as a function of applied magnetic field that is Boltzmann-like in nature, giving  $\pm$  the ISHE voltage at  $\pm$  applied magnetic field. The sweep rate was relatively fast, taking ~15 minutes per full scan (starting at max field, going to negative max field, and then returning to max field).

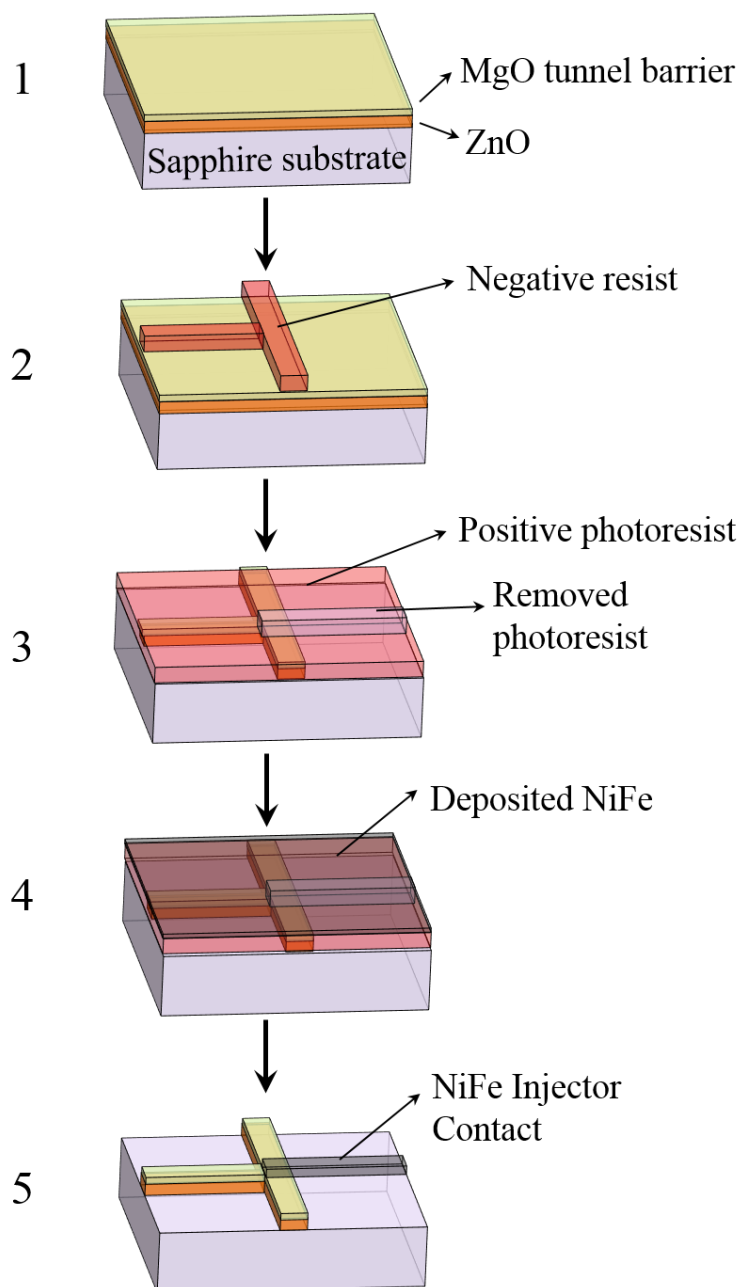


**Figure B.1 Procedure for fabricating the ISHE testing devices.** The steps outlining the fabrication procedure of the ISHE testing devices. In step 1, the ZnO and MgO layers are deposited on a sapphire substrate by PLD. In step 2, a negative resist is applied in the desired channel structure. The ZnO/MgO are then etched to the desired T-structure and the negative resist is removed. Then, in step 3, a positive photoresist is applied and patterned in the channel pattern for the NiFe deposition. NiFe is then deposited over the entire surface (both on the photoresist as well as in the channel) in step 4. Finally, the photoresist (and NiFe deposited on it) are removed with acetone and the final structure is ready for testing (step 5).

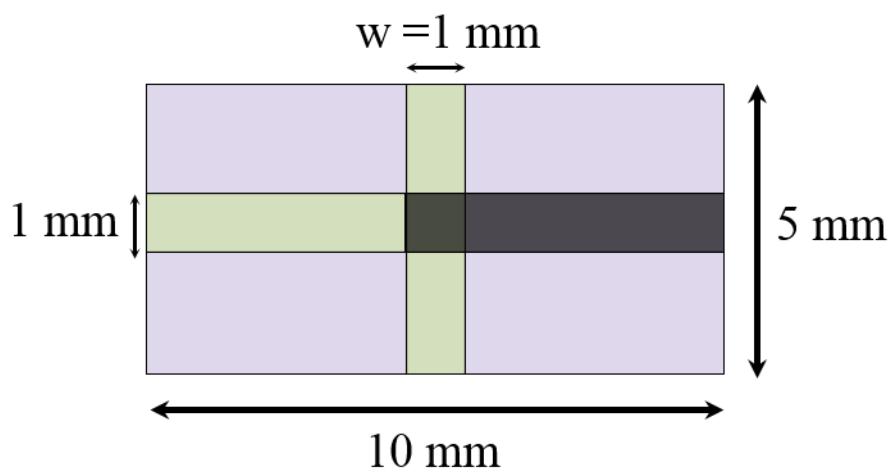


**Figure B.2 ISHE device schematic.** Schematic device design of the ISHE device with sample dimensions.

## APPENDIX C

### DEVICES FOR ELECTRICAL AND THERMAL

#### SPIN INJECTION IN ZNO

Chapter 6 discussed measurement of the ISHE in ZnO as a function of testing temperature and as a function of the oxygen pressure present during the deposition of the thin film. In addition, both electrical spin injection and thermal spin injection techniques were used to inject spin current in the ZnO. This injected spin current was then transformed to a charge current via the SOC. The electrical spin injection experiments were performed according to the method described above for Chapter 5 for all of the ZnO thin films deposited. Thin films of ZnO were deposited using the same deposition parameters; however, oxygen pressure during the deposition was varied. As such, ZnO films deposited under three different oxygen pressures were studied: films deposited under 0.1 mTorr of oxygen, under 1 mTorr, and under 10 mTorr of oxygen.

The oxygen pressure dependence of the spin Hall angle was then determined by measuring the ISHE response in the ZnO thin films at room temperature using the method and device design exactly as shown in Chapter 5. For testing the temperature dependence of the ISHE response in each of the samples, the scans were performed at temperatures between 50 and 300 K (data taken every 25 K; for example, 50 K, 75K, 100 K, etc.). To do the temperature-dependent testing, each sample was loaded and tested

one-at-a-time in a closed-cycle coldhead. Several raw data scans are shown in Figure A5 for the 0.1, 1, and 10 mTorr deposited samples.

As an alternative to electrical spin injection, thermal spin injection was also investigated. For thermally injecting spin-polarized carriers, the SSE was used. This effect relies on the propagation of magnons in a magnetic insulator – which are driven by the phonon response to a temperature gradient – to inject a spin-polarized current into ZnO via spin transfer torque between the ZnO/magnetic insulator layers. In these studies, YIG (yttrium iron garnet) was used as the magnetic insulator. ZnO was deposited on commercially available YIG thin films which were grown on GGG (gadolinium gallium garnet) substrates. The YIG/GGG substrates, purchased from MTI, were approximately 10 mm x 3 mm in size, with the YIG layer being 3  $\mu\text{m}$  thick and the GGG substrate being 0.5 mm thick. For testing the SSE response, a temperature difference of 3 K was applied through the thickness of the sample (from the GGG substrate to the ZnO thin film).

For testing the SSE response, a magnetic field was applied along the length of the sample, a temperature gradient was applied through the thickness of the sample, and the voltage was measured along the width of the ZnO layer. Similar to the electrical spin injection measurements, the magnetic field was swept in order to modulate the polarization of the injected spin current in the ZnO. For these measurements, the magnetic field was from 0.6 T to -0.6 T, at a rate of  $\sim 30$  minutes per sweep. The raw  $V_{\text{SSE}}$  data are shown in Figure C.1. To confirm that the observed response was due to the SSE, it was necessary to rule out the presence of any Nernst effect contribution.

The Nernst effect describes the generation of a voltage orthonormal to both an applied temperature gradient as well an applied magnetic field. As the temperature



gradient is applied, carriers begin to move through the sample along that gradient. If a magnetic field is being applied perpendicular to this movement, these carriers, moving in response to the temperature gradient, will feel a Lorentz force due to the Hall effect. As such, a voltage will develop in the third direction.

In ferromagnetic materials, there is an ultra-large enhancement in the Nernst effect response called the anomalous Nernst effect (ANE). This effect, similar to the anomalous Hall effect exhibited by ferromagnetic materials, gives a much larger than anticipated signal and is the Nernst effect occurring in ferromagnetic materials.<sup>1</sup> Although the ZnO tested is not ferromagnetic, it is important to consider the possibility of proximity-induced ferromagnetism in ZnO. As has been shown in graphene, it is possible to induce ferromagnetic behavior in a nonmagnetic material by its proximity to a magnetic layer, in this case YIG.<sup>2</sup> This effect can be probed in the ZnO/YIG system by using the arrangement outlined in Figure 6.1d. In this case, the applied temperature gradient is used to excite magnon motion along the width of the sample. However, due to the spin transfer torque process at the interface of the YIG/ZnO, we still get spin current injected from the YIG into the ZnO. Because of this, the injected current is moving in the same direction as the magnetic field and, because the spin-polarization vector and spin current direction are no longer orthogonal to one another, there should not be SSE response, but rather ANE in this arrangement.

Finally, in order to comment of the efficiency of the SSE, the temperature drop across the YIG can be estimated. If we assume that the thermal conductivity of the YIG and GGG layers is the same, the temperature drop across the 3  $\mu\text{m}$  thick YIG layer is

approximately equal to 18 mK. Based on our 150 nV signal at room temperature, this response gives an efficiency of  $\sim 18 \mu\text{V/K}$ .

### References

1. Nagaosa, N.; Sinova, J.; Onoda, S.; MacDonald, A. H.; Ong, N. P. *Rev. Mod. Phys.* **2010**, 82, 1539-1592.
2. Wang, Z.; Tang, C.; Sachs, R.; Barlas, Y.; Shi, J. *Phys. Rev. Lett.* **2015**, 114, 016603(1)-(5).

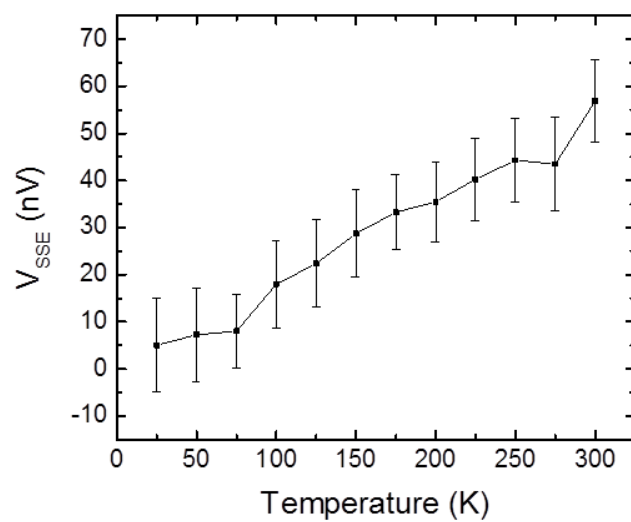


**Figure C.1 Raw  $V_{SSE}$  versus T data.** The non-normalized SSE data following subtraction of the ANE background response, plotted as a function of temperature.